Investigating Chemical and Structural Heterogeneities of High-Voltage Spinel Cathode Material for Li-ion Batteries

Stephanie Leigh Spence

Dissertation submitted to the faculty of the Virginia Polytechnic Institute and State University in partial fulfillment of the requirements for the degree of

Doctor of Philosophy
In
Chemistry

Feng Lin, Chair
Ayman M. Karim
Amanda Morris
John R. Morris

January 31st, 2023
Blacksburg, VA

Keywords: Li-ion batteries, intercalation chemistry, high-voltage cathodes, structural heterogeneity, nanodiffraction

Investigating Chemical and Structural Heterogeneities of High-Voltage Spinel Cathode Material for Li-ion Batteries

Stephanie Leigh Spence

Academic Abstract

Li-ion battery technologies have transformed the consumer electronics and electric vehicles landscape over the last few decades. Single-crystal cathode materials with controllable physical properties including size, morphology, and crystal facets can aid researchers in developing relationships between physical characteristics, chemical properties, and electrochemical performance. High-voltage $LiNi_{0.5}Mn_{1.5}O_4$ (LNMO) materials are desirable as cathodes due to their low cost, low toxicity, and high capacity and energy density making them promising to meet increasing consumer demands for battery materials. However, transition metal dissolution, interfacial instability, and capacity fading plague these materials when paired with graphite, limiting their commercial capability. Furthermore, variation in Ni/Mn ordering can lead to complex multiphase co-existence and changes in Mn oxidation state and electrochemical performance. These properties can be adjusted during synthesis using a facile and tunable molten salt synthesis method. This dissertation focuses on the investigation of chemical and structural heterogeneities of LNMO prepared under different synthetic conditions at different length scales. In Chapter 2, the influences of molten salt synthesis parameters on LNMO particle size, morphology, bulk uniformity, and performance are evaluated revealing the difficulty of reproducible cathode synthesis. We utilize the X-ray nanodiffraction technique throughout this work, which provides high-resolution structural information. We develop a method to measure and relate lattice strain to phase distribution at the tens of nanometers scale. In Chapter 3, mapping lattice distortions of LNMO particles with varying global Mn oxidation states reveals inherent

structural defects and distortion heterogeneities. In Chapter 4, we examine lattice distortion evolution upon chemical delithiation, Mn dissolution behaviors, and evaluate the chemical delithiation method as a means to replicate electrochemical cycling conditions. We further investigate lattice distortion spatially via *in situ* nanodiffraction during battery cycling in Chapter 5, illustrating the capabilities of the measurement to provide practical understanding of cathode transformations. From intra-particle to electrode materials level, heterogeneities that arise in cathode materials can dictate performance properties and degradation mechanisms and are necessary for researchers to understand for the improvement of Li-ion battery systems. The development of the nanodiffraction measurements aids in our understanding of inherent and dynamic materials chemical and structural heterogeneities.

Investigating Chemical and Structural Heterogeneities of High-Voltage Spinel Cathode Material for Li-ion Batteries

Stephanie Leigh Spence

General Audience Abstract

The invention of rechargeable Li-ion batteries in the 1990s has undeniably revolutionized modern civilization. Cell phones, laptops, grid energy storage, and electric vehicles have become fundamental fixtures of the 21st century. As technologies improve and requirements for advanced renewable energy storage have increased, researchers have sought to design longer lasting, faster charging, and more lightweight batteries. Modifying and finding new positive electrode materials is one way to improve the capabilities of modern batteries as their properties are governed by fundamental chemistry. High-voltage $LiNi_{0.5}Mn_{1.5}O_4$ (LNMO) is one such material that can allow for fast charging and high energy storage capacity, but its commercialization is hindered by complex physical and chemical properties, which can limit its lifetime in batteries. Large, particles with well-defined shapes are desirable to improve the stability of the materials; however, understanding their defects and structural heterogeneities is vital to continued optimization and requires advanced characterization techniques. In this dissertation, we characterize the physical phases and chemical properties of LNMO samples prepared under different conditions resulting in different particle shapes, sizes, and chemical distributions. An advanced X-ray nanodiffraction technique is used to measure phase distributions within individual particles while lab-based analytical techniques and electrochemical testing can determine bulk properties and battery performance of materials. Overall, the aim of this work is to develop techniques to measure structural and chemical heterogeneities of cathode materials at different length scales and to understand how they influence properties and performance in batteries. This work provides

valuable insights into the inherent and dynamic properties of high-voltage electrode materials useful to advance our understanding of how these materials fail and to aid researchers in creating design principles to develop stable, high-performing future generations of rechargeable batteries.

Acknowledgements

First and foremost, I would like to gratefully acknowledge my advisor, Prof. Feng Lin, without whose guidance and support, this work would not be possible. Thank you for your mentorship throughout the past five years. Your enthusiasm for science and passion for teaching are evident and inspiring. It has been a pleasure to be your student and learn valuable knowledge not only about electrochemistry and materials but how to be a successful and engaging scientist, communicator, and mentor.

I thank and appreciate my committee members, Prof. John Morris, Prof. Amanda Morris, and Prof. Ayman Karim. Your feedback and suggestions have pushed me to think deeper and strive to improve myself as a researcher. I would like to extend my thanks to the entire Virginia Tech Department of Chemistry for providing a wonderful environment and community for learning and researching throughout my time at Virginia Tech.

I am extremely lucky to have such a wonderful group of colleagues and friends in the Lin Lab. Special thanks to Dr. Crystal Waters, Dr. M. Mominur Rahman, Dr. David Kautz for welcoming me to your corner of the office when I first joined the lab. Thank you to Dr. Linqin Mu, Dr. Lei Tao, Dr. Dong Hou, Dr. Chunguang Kuai, Dr. Zhengrui Xu, Dr. Zhije Yang, Dr. Anyang Hu, Yuxin Zhang, Dawei Xia, Jungki Min, Anika Promi, Huabin Sun, Rachel Perez and all past and present Lin Lab members. Each of you have made contributions that have made me a better energy scientist.

Thank you to my collaborators Dr. Sami Sainio and Dr. Dennis Nordlund at SSRL, Dr. Luxi Li and Dr. Cheng-Jun Sun at Argonne National Laboratory, and Dr. Yong S. Chu, Dr.

Xianghui Xiao, and Dr. Xiaojing Huang at Brookhaven National Laboratory for help conducting experiments, processing data, and engaging in fruitful scientific discussions.

Katherine Ammon, Steven Blackburn, Alannah Brow, and Christopher Thornhill, aka Zoomin' Boomin Buddies, aka Keen for Sheen, aka Yearn for Dern, aka Jodie Devotees, aka Edie Flaco, aka Hailers of Taylor, aka Leerin at Mirren, I am forever grateful for your friendship (and memes). Thank you Steven Frederiksen for being an exceptional friend, partner, and supporter.

Lastly, thank you to my brothers Chris, Phil, and Neil and my parents Donna and Stephen Spence for your unwavering love, encouragement, and support.

Table of Contents

Attributions

Chapter 1 of this dissertation includes materials published in *Reference Module in Earth Systems and Environmental Sciences*, **DOI:** 10.1016/b978-0-12-819723-3.00093-7, and is reprinted with permission from Elsevier: Spence, S. L.; Lin, F. Single-Crystal Oxide Cathode Materials. In *Reference Module in Earth Systems and Environmental Sciences*; Elsevier, 2021. Chapter 1 also includes work published in *Inorganic Chemistry*, **DOI:** 10.1021/acs.inorgchem.0c01042, and is reprinted with permission from the American Chemical Society: Spence, S. L.; Xu, Z.; Sainio, S.; Nordlund, D.; Lin, F. Tuning the Morphology and Electronic Properties of Single-Crystal $LiNi_{0.5}Mn_{1.5}O_{4-\delta}$: Exploring the Influence of LiCl–KCl Molten Salt Flux Composition and Synthesis Temperature. *Inorg. Chem.* **2020**, *59*, 10591–10603.

Chapter 2 is an unpublished manuscript under preparation for submission. Dr. Feng Lin conceived and oversaw the study. Stephanie L. Spence and Dr. Feng Lin designed experiments. Rachel Perez assisted with materials synthesis, coin cell fabrication, and data analysis. Dr. Anyang Hu performed SEM measurements. Stephanie L. Spence conducted all additional synthesis, experimentation, and analysis.

The third chapter of this work has been published in *ACS Energy Letters*, **DOI:** 10.1021/acsenergylett.1c02759, and is reprinted with permission from the American Chemical Society: Spence, S. L.; Hu, A.; Jiang, M.; Xu, Z.; Yang, Z.; Rahman, M.M.; Li, L.; Chu, Y.S.; Xiao, X.; Huang, X.; Lin, F. Mapping Lattice Distortions in $LiNi_{0.5}Mn_{1.5}O_4$ Cathode Materials. *ACS Energy Lett.* **2022**, *7*, 690-695. It has been formatted for this thesis. Dr. Feng Lin conceived and led the study. Stephanie L. Spence and Dr. Feng Lin designed experiments. Stephanie L. Spence performed materials synthesis, electrochemical measurements, and Raman measurements. Dr. Zhengrui Xu and Dr. Zhijie Yang collected synchrotron XAS measurements. Dr. Muhammad

Mominur Rahman performed SEM and synchrotron XRD measurements. Dr. Luxi Li, Stephanie L. Spence, and Dr. Anyang Hu performed BCDI measurements. Stephanie L. Spence, Meng Jiang, Dr. Yong S. Chu, and Dr. Xiaojing Huang performed HXN measurements and assisted with data analysis. Dr. Xianghui Xiao participated in scientific discussions and assisted with data analysis. Stephanie L. Spence and Dr. Feng Lin wrote the manuscript with feedback from all coauthors. All authors have approved the final version of the manuscript.

Chapter 4 is an unpublished manuscript under preparation for submission. Dr. Feng Lin conceived and oversaw the project. Stephanie L. Spence and Dr. Feng Lin designed experiments. Dr. Anyang Hu performed SEM measurements. Dr. Sami Sainio and Dr. Dennis Nordlund collected soft XAS data. Stephanie L. Spence and Dr. Xiaojing Huang performed HXN experiments and data analysis. Stephanie L. Spence conducted all additional synthesis, experimentation, and analysis.

Chapter 5 is an unpublished manuscript under preparation for submission. Dr. Feng Lin conceived and led the project. Stephanie L. Spence and Dr. Feng Lin designed experiments. Dr. Sami Sainio and Dr. Dennis Nordlund collected soft XAS data. Stephanie L. Spence, Anika Promi, and Dr. Xiaojing Huang performed HXN experiments and data analysis. Stephanie L. Spence conducted all additional synthesis, experimentation, and analysis.

Abbreviations

BCDI, Bragg coherent diffraction imaging

CEI, Cathode-electrolyte interphase

EXAFS, Extended X-ray absorption fine structure

FY, Fluorescence yield

HXN, Hard X-ray nanoprobe

LCO, $LiCoO_2$

LFP, $LiFePO_4$

LIB, Lithium-ion battery

LMO, $LiMn_2O_4$

LNMO, $LiNi_{0.5}Mn_{1.5}O_4$

NCA, $LiNi_xCo_yAl_zO_2$

NMC, $LiNi_xMn_yCo_zO_2$

SEI, Solid-electrolyte interphase

SEM, Scanning electron microscopy

SOC, State-of-charge

TEY, Total electron yield

TM, Transition metal

TXM, Transmission X-ray microscopy

XANES, X-ray absorption near-edge spectroscopy

XAS, X-ray absorption spectroscopy

XRD, X-ray diffraction

Chapter 1. Introduction

1.1. Li-ion Battery Cathode Technologies and Innovations

Over the past 30 years, Li-ion batteries (LIB) have become ubiquitous components of society. With applications in communication, entertainment, transportation, and energy storage devices, the rapid growth of battery usage worldwide has been accompanied by advances in our scientific understanding of battery systems and technologies. LIBs were first commercialized by Sony in 1991. Since then, researchers have sought to improve the safety, capacity, lifetime, and cost-effectiveness of active materials.[1] Transition metal oxides have stood out as promising positive electrode materials,[2,3] and in fact, the majority of devices still utilize $LiCoO_2$ (LCO), the first commercialized cathode material.[4,5] LIBs rely on intercalation chemistry used to drive the insertion and removal of Li ions from the positive to negative electrodes, accompanying the electron transport that occurs through an external circuit to power devices, as illustrated in **Figure 1-1**.[3,6] The 2019 Nobel Prize in Chemistry awarded for the development of Li-ion batteries signifies their value and importance in society as we steer towards a more sustainable energy future.

Cathode research in recent years has led to the development of new high-energy density layered transition metal oxides derived from LCO. These state-of-the-art materials include $LiNi_xCo_yMn_zO_2$ (NMC) and $LiNi_xCo_yAl_zO_2$ (NCA) classes of materials.[7,8] However, these materials are limited by capacity fading, instability during high-voltage operation which can lead to irreversible oxygen and Li loss and electrolyte side reactions, and structural or chemical reconstruction.[9] Olivine $LiFePO_4$ (LFP) is favored in applications requiring high operating safety but has low specific energy.[10] Spinel $LiMn_2O_4$ (LMO) was first investigated by Thackeray and co-workers in the 1980s and was favorable for its three-dimensional framework allowing for fast Li^+

intercalation.[11,12] Mn containing spinel materials face issues of Mn dissolution leading to loss of active material and poor long-term cycling stability.[13] Partial substitution with Ni to form $LiNi_{0.5}Mn_{1.5}O_4$ (LNMO) increases the overall Mn oxidation state to 4+ and lowers the Ni^{2+}/Ni^{3+} redox couple to provide a cathode that operates at a high voltage versus Li/Li^+.[14–16] The high-voltage material is attractive for high energy applications, but commercial carbonate-based electrolytes are often unstable at the operating voltage. **Figure 1-2** shows the crystal structures, specific capacity, and specific energy of common cathode materials for LIBs.

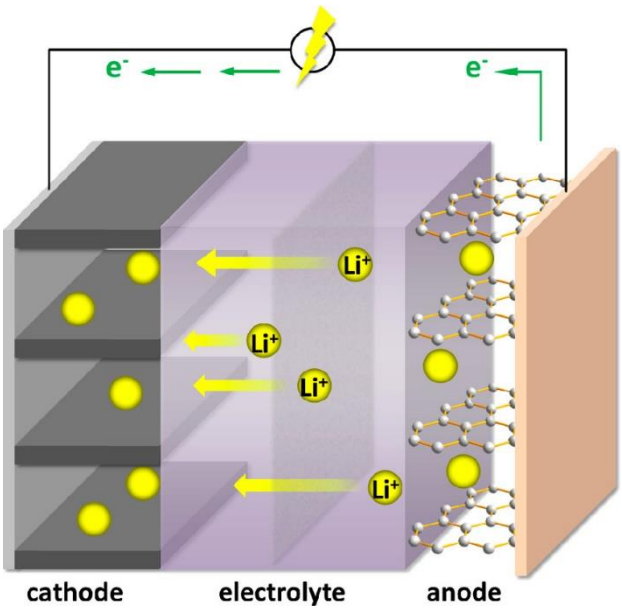

Figure 1-1. Schematic of a Li-ion battery based on dual intercalation chemistry. Reproduced with permission from reference [17]. Copyright 2012, Sigma-Aldrich Co.

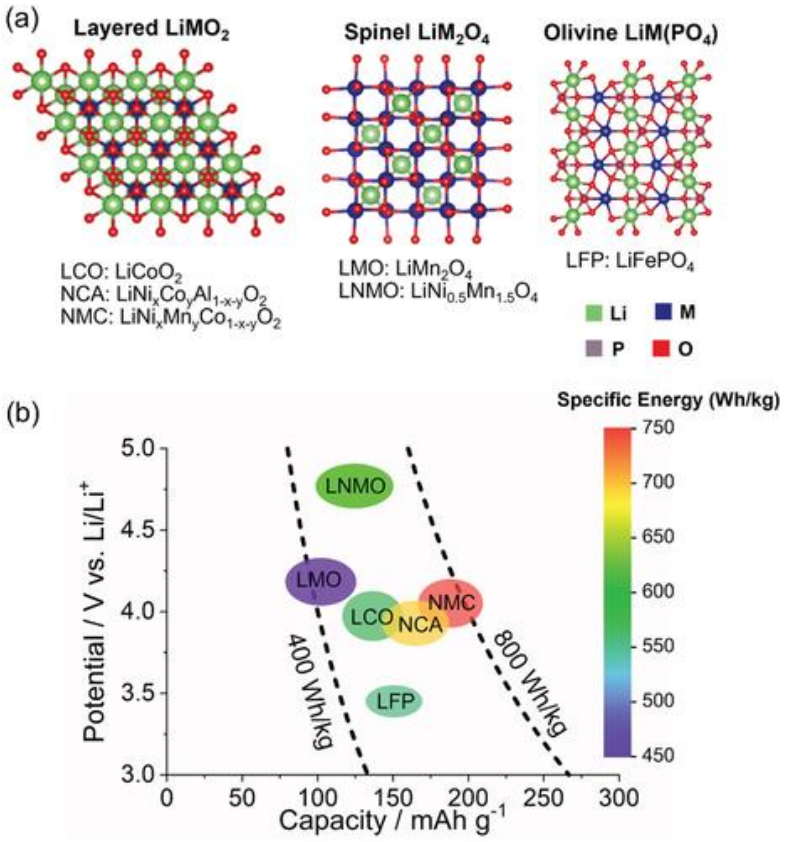

Figure 1-2. (a) Crystal structures of common cathode materials including layered, spinel, and olivine (viewed along the *a*-axis). **(b)** Operating potential, specific capacity, and specific energy of common cathode materials. Reproduced with permission from reference [18]. Copyright 2022, Wiley.

Both Co and Ni are classified as toxic elements.[19] Co is also expensive and at the center of controversial human rights issues as its mining involves alleged child labor in the Democratic Republic of Congo.[20] A drive towards the development of Co-free batteries has arisen in recent years to reduce costs, improve safety, and address moral concerns. The Ni-containing analog, layered $LiNiO_2$, is lower cost and has a higher specific capacity than LCO, but Li and Ni cation mixing can readily occur, blocking Li^+ pathways and creating structural instabilities.[18] Trinary transition metal layered cathodes NMC and NCA have found commercial success by balancing

capacity and structural stability; however, Co-free, high Ni content is still of interest for next-generation, low-cost, high-energy-density batteries with the help of doping and coating strategies.[21,22] **Figure 1-3a-b** compares the costs of elements and element ratios in common cathode materials. Furthermore, single-crystal cathodes are advantageous for mitigating electro-mechanical degradation in cathode particles, including Ni-rich layered materials.[23] Degradation mechanisms including structural changes, crack formation, transition metal migration, and dissolution all affect the stability and longevity of cathodes.[24] Careful control of microstructure including morphology is also a strategy of frontline research efforts to enhance the performance of materials.[25]

Ultimately, with limited availability and high costs, Co-containing cathodes are not sustainable to meet future market demands for LIBs. With a balanced capability in terms of cost, energy density, thermal stability, tap density, cycle life, and rate performance (**Figure 1-3c**), spinel LNMO is a promising cathode material with high voltage applications. The research herein focuses on investigating the influence of synthetic methods on particle uniformity and performance in single-crystal, high-voltage LNMO cathode materials. Furthermore, we develop and utilize advanced X-ray characterization techniques to understand inherent structural and chemical heterogeneities and dynamic phase transformation behaviors during chemical Li^+ removal and under electrochemical cycling conditions. This chapter will review the features and properties of single-crystal transition metal oxide cathodes, characteristics and frontier research of high-voltage LNMO materials, strategies for tailoring single-crystal LNMO materials properties during synthesis, and structural characterization techniques.

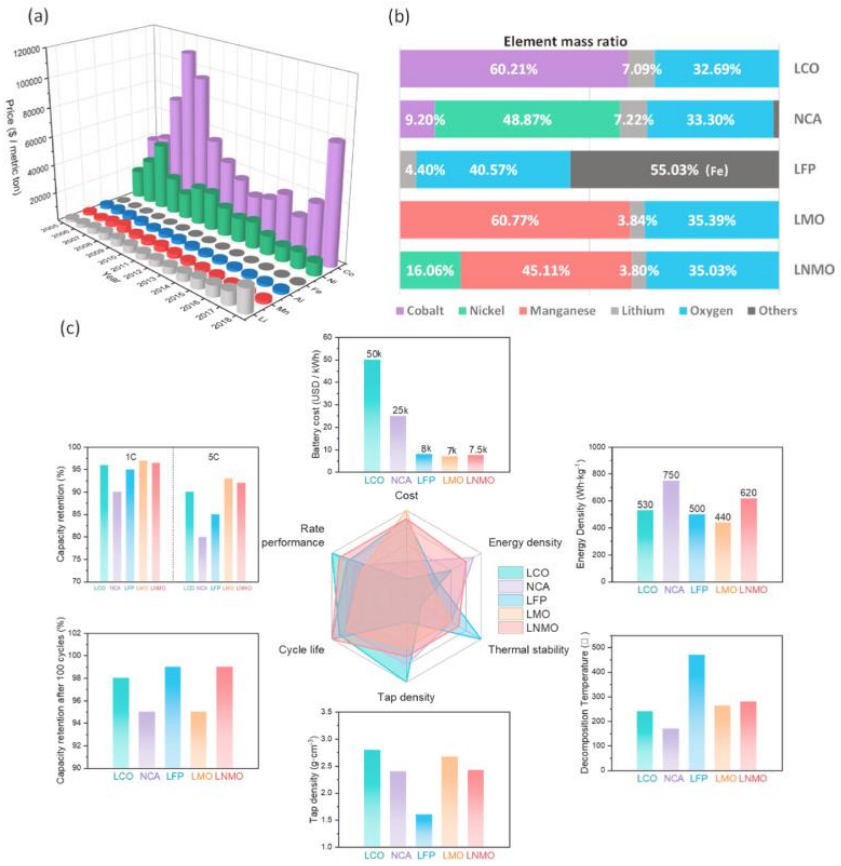

Figure 1-3. (a) The annual price of elements for Li-ion batteries. **(b)** Element mass ratios in common cathode materials. **(c)** Radar map of metrics for common cathode materials. Reproduced with permission from reference [26]. Copyright 2020, Elsevier.

1.2. Single-Crystal Cathode Materials

There has been a recent drive to develop single-crystal materials with well-controlled physical properties to establish clear relationships between physical characteristics and electrochemical performance and stability of materials.[24] Transition metal oxide cathodes are often synthesized as polycrystalline materials consisting of large micrometer-sized aggregates, or secondary particles, further comprised of individual nanometer-sized primary particles.[27] The performance of a material is dictated by the physical properties of both the primary and secondary

particles, including primary particle size distribution, porosity, and grain boundaries. These materials are intrinsically vulnerable to mechanical degradation and fractures along grain boundaries.[28–30] Understanding degradation mechanisms become complicated with polycrystalline materials containing multiple grain boundaries.[24] It is difficult to synthetically control the properties of secondary and primary particles individually, and even more difficult to isolate the impact of specific physical properties on the performance of the overall material.[9,31] Designing single-crystal materials is a direct method to address the issues plaguing polycrystalline cathodes.

Layered polycrystalline materials suffer anisotropic volume change during Li^+ extraction and insertion and are vulnerable to fracturing, leading to phase transformation, transition metal dissolution, lattice oxygen release, and electrolyte decomposition.[32,33] This results in poor cycling stability or battery failure due to disruption of electronic and ionic conduction pathways.[28] Single-crystal materials without internal grain boundaries are more morphologically stable and have smaller surface areas, and less cracking, gas evolution, and side reactions, contributing to reduced capacity fading and higher safety features.[33,34] Furthermore, single-crystals can be synthesized with controllable and tunable sizes and morphologies easier than polycrystalline materials, which can help correlate specific material properties to performance. **Figure 1-4** summarizes the performance difference and morphological features visualized by scanning electron microscopy (SEM) of single-crystal versus polycrystalline cathode materials. When comparing micron-sized single-crystal and polycrystalline NMCs, the single-crystals exhibited higher capacity retentions during half-cell cycling at both 40 and 55 °C and were also resistant to oxygen loss below 100 °C.[35] Superior long-term cycling[36] and rate performance, as well as less cation mixing,[37] have also been observed due to mitigation of anisotropic stress. Despite mechanical improvements, single-crystals still face anisotropic volume change in layered materials or lattice distortion in spinel

materials, as well as intergranular fractures to alleviate internal stress or due to structural instability upon deep delithaitaion.[33] Therefore, understanding defects and structural heterogeneities in single-crystal materials is vital for continued optimization. Single-crystal materials are also often much larger as a result of increased crystal growth rates to prevent crystal agglomeration. There is a trade-off in that in the larger crystals surface areas are reduced, decreasing electrolyte side reactions, but Li^+ diffusion paths become longer leading to poorer rate performances.[38] Most single-crystal Ni-rich materials have therefore not yet reached the reversible capacity performance of polycrystalline materials; however, strategies such as surface coating, doping, and rational facet design have been employed to promote Li^+ transport.[34]

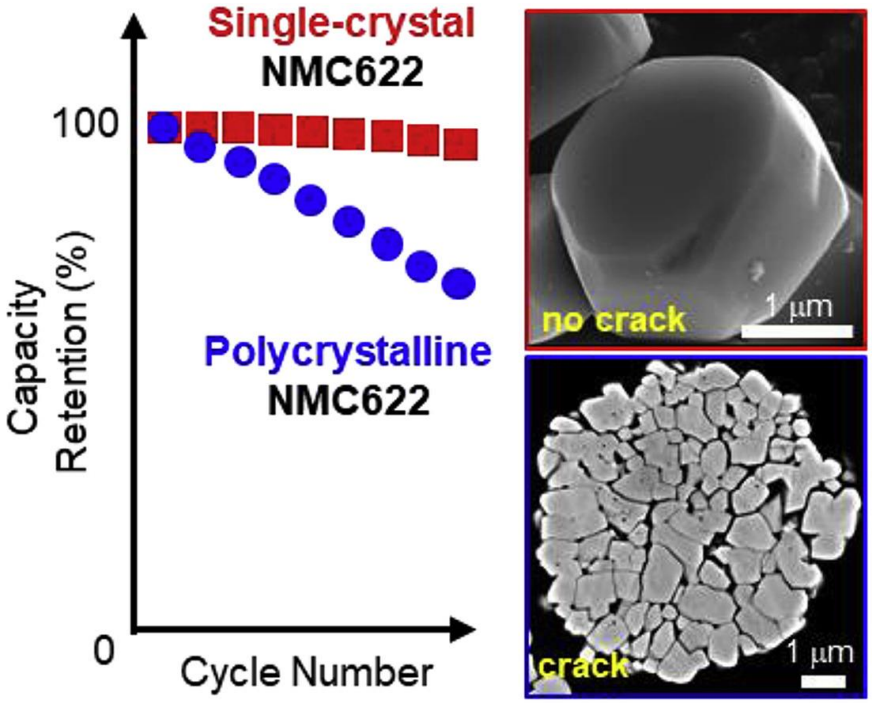

Figure 1-4. Performance difference and SEM images of polycrystalline and single-crystal NMC cathode materials. Reproduced with permission from reference [33]. Copyright 2020, Elsevier.

Tailoring particle facets is a strategy to alter the electrochemical performance of single-crystal materials through stabilizing surfaces for high-voltage operation, or to improve Li^+ diffusion rates for improved high-rate performance. **Figure 1-5** shows NMC particles synthesized in different morphologies including octahedrons, truncated octahedrons, polyhedrons, and platelets with various percentages of (104), (001), and (012) surface facets.[24] The (001) dominated platelets showed superior high-voltage cycling stability as the low-energy facets are parallel to the transition metal layer and are more resistant to chemical reduction. The high-energy (012) surfaces of the truncated octahedron were more reactive, providing greater initial discharge capacity and efficient Li^+ transport, but poorer long-term cycling stability. LNMO of different morphologies also exhibited facet-dependent performance, with stable (111) facets containing octahedrons exhibiting superior specific capacity and rate capability compared to other facets which suffered surface reconstruction upon contact with electrolytes.[39] Size of the particles is also a dictating factor of performance with larger, more robust particles having longer cycling stability than nanometer counterparts.[33,40] Morphological control and surface engineering are advantages of single-crystal cathode materials over polycrystalline materials. At present, the optimization of single-crystal cathodes is limited by current synthesis methods as the high-temperature synthesis often used can introduce structural disorders and impurities, and wet chemical methods are often complex and use volatile or toxic solvents.

The structural enhancement and superior mechanical stability of single crystals allow for improved electrochemical performance. After cycling, single-crystal Ni-rich materials have shown reduced phase transformation layers and suppressed intra-granular cracking under standard cycling conditions.[36,41] High-voltage cycling is desirable for increasing specific capacities and energy densities, but the material must be stable to be practically viable. For single-crystal NMC material

cycled to 4.7 V vs Li/Li^+, capacity fading was observed after 200 cycles, and significant cracking and phase transformation to a Ni-rich rock-salt phase was observed, illustrating that degradation is still an issue upon strenuous cycling.[42] Surface treatment and rational design of particle microstructure have been strategies to improve structure and performance, but further optimization is still required. Presently, single-crystal materials with high mechanical and interfacial stability have promising potential to meet demands for stable and safe LIBs.

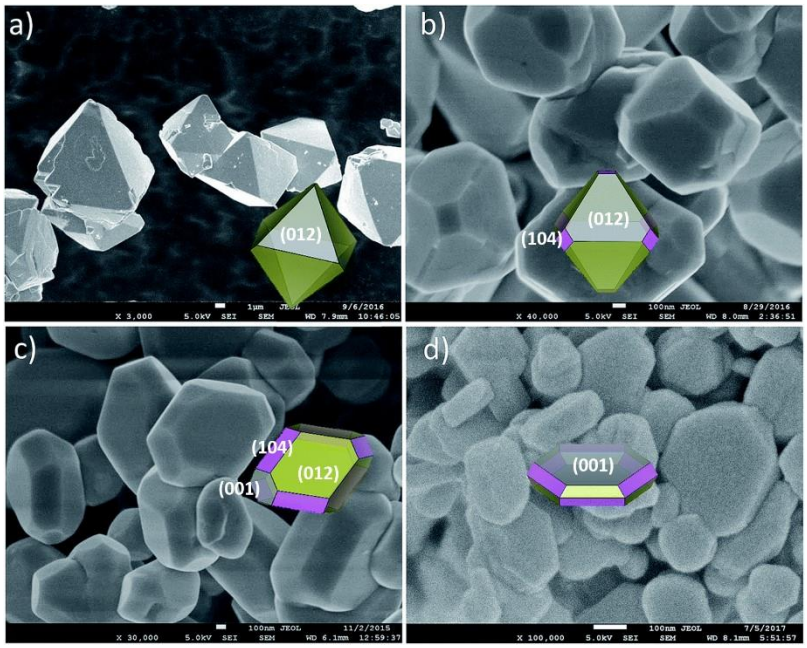

Figure 1-5. SEM images of NMC single-crystal particles with different morphologies: **(a)** octahedron, **(b)** truncated-octahedron, **(c)** polyhedron, and **(d)** platelet. Reproduced with permission from reference [24]. Copyright 2019, The Royal Society of Chemistry.

1.3. High-Voltage Spinel $LiNi_{0.5}Mn_{1.5}O_4$

High-voltage spinel LNMO is a cathode material that can potentially meet demands for higher energy density and power density in consumer batteries.[43] With low costs, low toxicity, an

abundance of raw materials for Mn, and a three-dimensional framework for fast Li^+ intercalation, LNMO is a green alternative to Co-containing layered materials.[11] LNMO operates at a voltage of 4.7 V vs Li/Li^+, has a theoretical capacity of 147 mAh/g, a practical capacity of 125 mAh/g, and an energy density of 650 Wh/kg.[15,43,44] LNMO is a complex system, but is also highly tunable and can be easily synthesized as single crystals and with variations in structural and electronic properties.

1.3.1. Cation Ordering, Mn Oxidation State, and Performance Relationships

LMO is a cubic spinel with $A[B_2]O_4$ structure where oxygen anions form a face-centered cubic arrangement, Li cations in the A-site fill 1/8 of the tetrahedral 8a positions, and Mn cations in the B-site fill 1/2 of the octahedral 16d positions.[45] MnO_6 forms 3-dimensional $[B_2]O_4$ arrays which share edge sites allowing Li^+ to diffuse via empty 16c octahedral sites. In the partially Ni substituted derivative, LNMO, two crystallographic structures can be formed. Oxygen sits in the 8c and 24e sites and Li sits in the 4c tetrahedral sites.[43] When Ni occupies 4a positions and Mn occupies 12b octahedral positions, the material is said to be cation ordered and forms a superlattice with $P4_332$ symmetry.[43,46] A random arrangement of Ni and Mn on 16d octahedral sites is denoted as the disordered spinel and has an $Fd\bar{3}m$ phase group. **Figure 1-6** illustrates the transition metal arrangement in the two crystal structures. The disordered material is favored at synthesis temperatures above 700 °C due to the slow kinetics of cation intermixing.[47–49] The stoichiometric ordered phase is more thermodynamically favorable as the higher temperatures used to form the disordered phase can create oxygen vacancies.[50] The presence of oxygen vacancies may also lead to the reduction of a small amount of Mn from the stoichiometric 4+ oxidation state to 3+ to provide an overall charge compensation.[51,52] Furthermore, secondary rock-salt structured Li_{1-}

$_xNi_xO$-type impurities can also be formed.[47] Impurity phases can increase the Mn/Ni ratio in the spinel phase increasing the proportion of Mn^{3+}.[53] Synthesis under an oxygen environment or post-annealing at the phase transition temperature can be used to increase the transition metal ordering and minimize the impurity phases.[54,55]

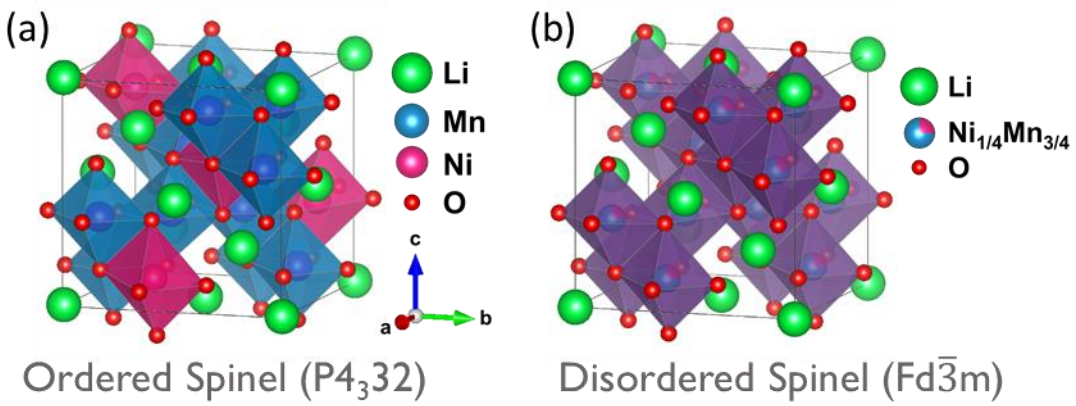

Figure 1-6. Crystal structures of **(a)** ordered spinel LNMO with $P4_332$ phase group and **(b)** disordered spinel LNMO with $Fd\bar{3}m$ phase group. Structures created with Vesta software.

In a perfectly ordered material, Mn^{4+} is electrochemically inactive while Ni^{2+}/Ni^{4+} duel redox at ~ 4.7 V vs Li/Li^+ is responsible for the electrochemical performance.[56] When Mn^{3+} is introduced, it can participate in redox events leading to an additional voltage plateau at ~ 4.0 V vs Li/Li^+ and provide enhanced electrochemical performance.[57] Mn^{3+} has been shown to increase electronic conductivity by two orders of magnitude, improving performance at high rates of charging and discharging.[52] The improved transport kinetics have also been attributed to cation disordering.[56] **Figure 1-7** shows the typical charge and discharge voltage profiles for cation ordered and disordered spinel materials while **Figure 1-8** shows the relative energies and density

of states for the available redox couples. The disordered phase is overall favorable due to better electrochemical performance and structural reversibility at faster rates.[47]

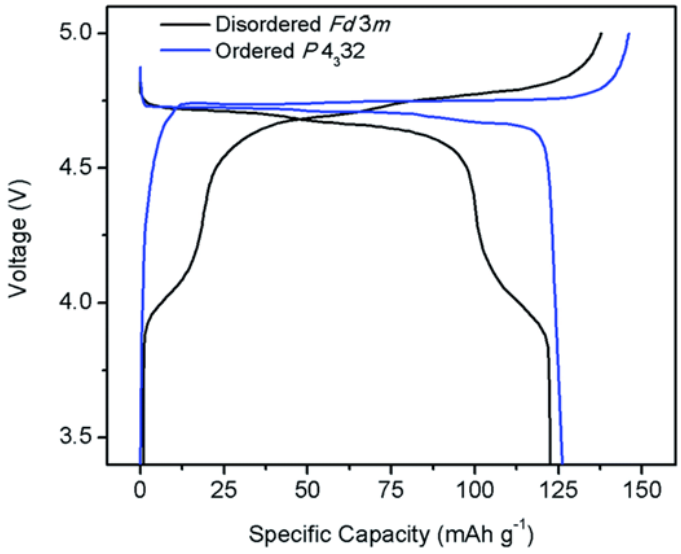

Figure 1-7. Typical charge/discharge profile of ordered $P4_332$ and disordered $Fd\bar{3}m$ LNMO. Reproduced with permission from reference [58]. Copyright 2014, The Royal Society of Chemistry.

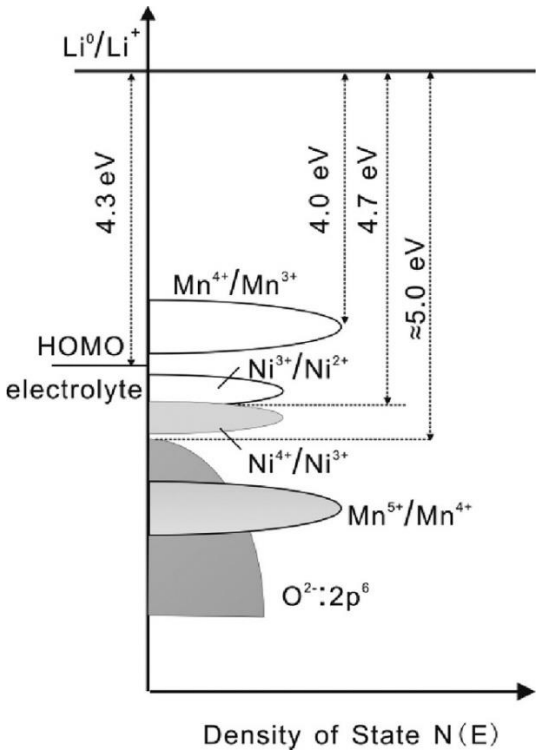

Figure 1-8. Schematic of energy versus density of states for LNMO. Reproduced with permission from reference [55]. Copyright 2012, American Chemical Society.

The cation ordering, Mn^{3+} content, oxygen vacancy formation, and impurity identity are all closely related and have significant impacts on the performance of LNMO.[59,60] Careful control of synthesis parameters is required to fully understand the influence of each material property. Practically, a fully cation-ordered or disordered material is difficult to obtain as individual particles likely contain local domains with varying degrees of cation order throughout. This inherent structural heterogeneity further complicates efforts at deconvolution of contributions from cation ordering degree and Mn^{3+} content.[61–63] The presence of antiphase boundaries can also hinder Li^+ transport and lower the reversible capacity at higher cycling rates.[62]

1.3.2. Phase Transformations upon Li^+ Removal

Phase transformations in LNMO upon Li^+ removal maintain the cubic spinel framework. The ordered spinel converts via two two-phase reactions progressing from $LiNi_{0.5}Mn_{1.5}O_4$ to $Li_{0.5}Ni_{0.5}Mn_{1.5}O_4$ to $Ni_{0.5}Mn_{1.5}O_4$ with approximately 3% and 3.3% volume change, respectively.[64,65] Ni^{2+}/Ni^{3+} and Ni^{3+}/Ni^{4+} redox couples occur as individual events with negligible voltage differences, and so a single voltage plateau is observed in the charge/discharge curve. The disordered spinel is found to transition via a solid solution reaction of $Li_{1-x}Ni_{0.5}Mn_{1.5}O_4$, where $0 \leq x \leq 0.5$, followed by a single two-phase transformation to the fully delithiated spinel.[66,67] The voltage plateau of the disordered material, therefore, occurs with two distinct regions with less defined plateaus. The solid solution behavior is kinetically advantageous compared to the two-phase transformation and is partially responsible for improved ionic conductivity and resulting rate capability observed in the disordered material.[68] Powder X-ray diffraction (XRD) patterns taken *in situ* during charging of cation ordered and disordered spinel LNMO samples show the dynamic structural changes and illustrate the differences in the phase transformation behaviors in the two materials (**Figure 1-9**). From the diffraction patterns, the lattice constants can be obtained at different states of charge (SOC) to illustrate the difference in two-phase versus solid-solution mechanisms where the former has discrete lattice changes for each phase and the latter has a continuous contraction. At the particle level, two- or three-phase intra-particle coexistence has been found to occur, suggesting heterogeneous rates of delithiation within a particle.[64] Lattice mismatch between the three cubic phases and a large volume change during charging and discharging can lead to particle strain, mechanical degradation, and failure of the materials or device.

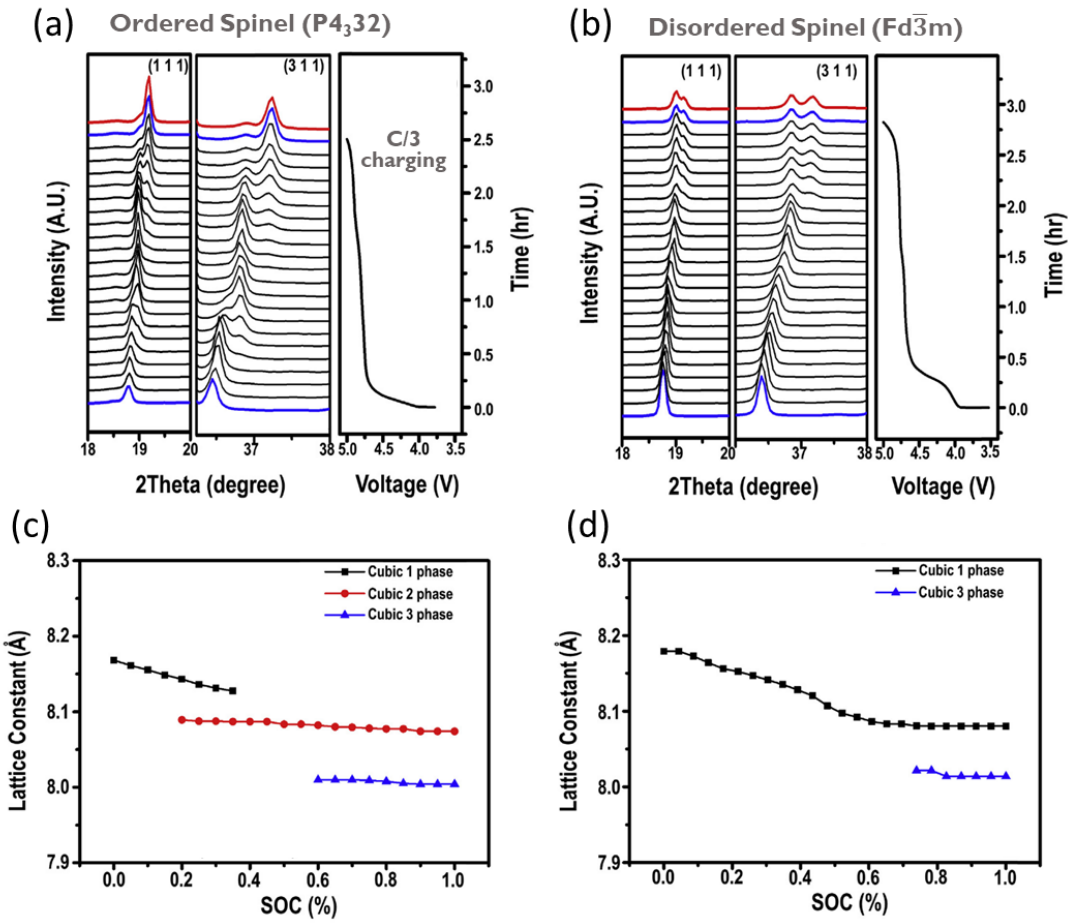

Figure 1-9. *In situ* powder XRD patterns and lattice parameter variation of **(a)** and **(c)** ordered and **(b)** and **(d)** disordered LNMO sample during charging. Modified with permission from reference [66]. Copyright 2016, Elsevier.

1.3.3. Degradation Mechanisms and Modification Strategies

LNMO faces many practical challenges including Mn dissolution, Jahn-Teller distortion, and electrolyte instability, all contributing to poor full-cell cycling performance. Mn dissolution is perhaps the greatest barrier to the commercialization of LNMO materials. Mn^{3+} in spinel Mn oxides is known to disproportionate into Mn^{2+} and Mn^{4+} in the presence of acid following the reaction $2Mn^{3+} \rightarrow Mn^{2+} + Mn^{4+}$.[12,69,70] Fluorine-containing salts used in electrolyte formation can

produce acidic HF in LIBs, leading to Mn dissolution in LNMO cathodes.[71,72] This can lead to loss of redox active material which can migrate through the electrolyte and deposit on the anode (**Figure 1-10**).[73] Under practical battery conditions, side reactions at the interface between the electrode active material and the liquid electrolyte can form solid products which deposit on electrodes forming passivation layers: the solid-electrolyte interphase (SEI) at the anode and cathode-electrolyte interphase (CEI) at the cathode.[74] Deposition of dissolved transition metals at either interphase can poison the passivation later and lead to severe capacity fading, especially on graphite anodes. Jahn-Teller distortion occurs when increased Mn^{3+} content causes a distortion of the MnO_6 octahedral, which increases lattice strain inducing crack formation, reduces crystal symmetry, and forms Li excess tetragonal phases.[11,16] Additionally, the high voltage of operation for LNMO can lead to side reactions with carbonate electrolytes, which are oxidized around 4.3 V vs Li/Li^+ without a stable SEI.[55,75] O_2, CO_2, and H_2 gas production can also occur at high voltages and elevated temperatures, leading to severe capacity fading.[76] Surface instability at high SOC can lead to oxygen migration and loss and the formation of tetragonal Mn_3O_4 leading to further Mn dissolution.[77,78] Ultimately, interfacial reactions and capacity fading are the primary challenges for LNMO/graphite full cells. Without modification, LNMO/graphite cells have been found to reach 120 mAh/g initial capacity with <80% retention after 200 cycles.[79,80]

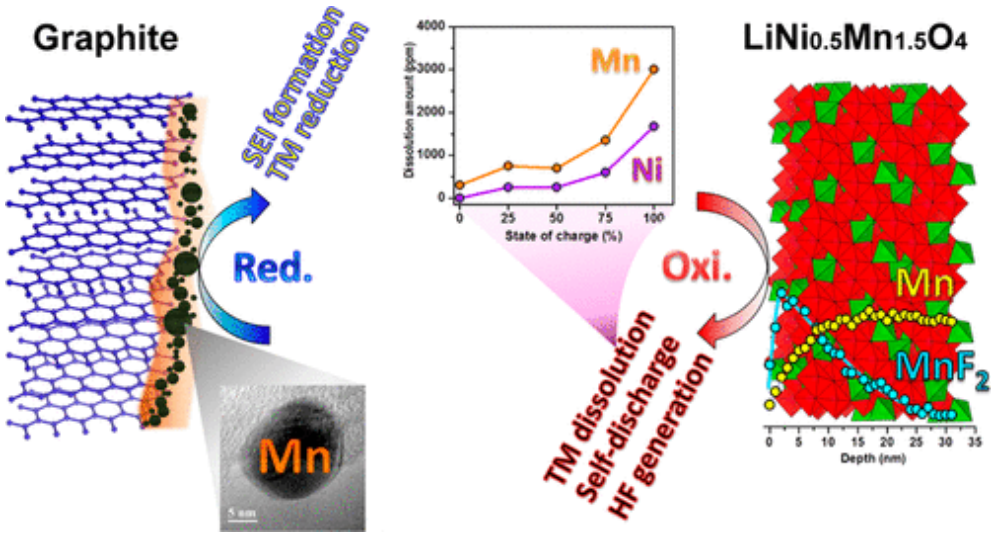

Figure 1-10. Schematic of degradation mechanisms of high-voltage LNMO/graphite full cells during electrochemical cycling. Reproduced with permission from reference [72]. Copyright 2013, American Chemical Society.

Several strategies have been undertaken to improve the interfacial stability of high-voltage LNMO including element doping, coating, electrolyte modification, and microstructural control to minimize the severity of side reactions and optimize Li^+ diffusion lengths.[81] Doping with transition metals such as Fe, Ga, Zn, Al, Cr, Co, and Cu can improve ionic and electronic conductivity, stabilize crystal structure, adjust Ni/Mn ordering, and influence surface facet growth and particle morphology.[82,83] Likewise, surface coating with metals, metallic oxides, or inorganic ionic or electronic conductors can inhibit surface structural degradation, transition metal dissolution, and enhance Li^+ diffusion, allowing for better cycling stability and rate performance. Compatible high-voltage stable electrolytes are required for the commercialization of LNMO. Fluorinated solvents such as fluoroethylene carbonate (FEC) or salt additives including lithium bis(oxalate)borate (LiBOB) and dimethyl methylphosphonate (DMMP) can improve cycling stability.[58] Solid electrolytes with high lithium-ion conductivity and stable interfaces are also desirable. In rationally

designing single-crystal size and shape, larger particles with lower surface areas are less prone to interfacial reactions with electrolytes which may lead to Mn dissolution, while smaller particles may have shorter Li^+ diffusion lengths and increase capacity and rate capability.[40,84] Crystallographic facets are also influential. The thermodynamically stable (111) facets enclosing octahedrons can facilitate the formation of a stable SEI, improving cycling performance,[84,85] while the less densely packed (110) facets can improve rate capability, but may be more prone to side reactions.[86,87] These trade-offs in size and morphology indicate that combining strategies and careful control of materials properties are necessary to develop practical high-voltage spinel cathode materials.

1.4. Tuning and Characterizing Material Properties of $LiNi_{0.5}Mn_{1.5}O_4$

Researchers have long sought to correlate high-voltage LNMO materials properties including particle size and morphology, crystal structure, and Mn^{3+} content to electrochemical performance for rationally designing materials with improved performance.[40,84,88–90] Studies attempting to decouple the individual parameters of LNMO have debated the significance of morphology versus structural ordering or Mn^{3+} content.[56,87,91,92] Particle morphology and crystal structure can be engineered during growth by altering chemical and physical conditions during synthesis.[82,93,94] LNMO has been synthesized via co-precipitation,[95,96] solid state[97–99], carbon exo-templating,[100] and molten salt methods.[101,102] The molten salt method uses a low melting point salt flux which allows for fast diffusion of raw materials and high crystallinity of products. Synthetic conditions including temperature, heating duration, precursors, molten salts, and ratios of reactants and salts can all be easily modified making this method favorable to tune LNMO properties.[47,101,103]

1.4.1. Morphological Control

A series of LNMO materials was prepared via a molten salt method using a mixture of LiCl and KCl salts.[104] Systematically varying the composition of the flux across the phase diagram of the two salts allowed for tuning the melting point of the composite salt mixture. Furthermore, changing the max synthesis temperature influenced the conditions for particle formation. For example, a 59:41 ratio of LiCl:KCl has a minimum melting temperature of 352 °C and is known as the eutectic ratio, while a 20:80 ratio has a high composite melting temperature of 688 °C.[105] **Figure 1-11a** shows the LiCl-KCl phase diagram with the various salt ratio and temperature points investigated during the study and the major material properties that dictate electrochemical performance. SEM was used to investigate particle morphology, and changes were most significant as the salt compositional ratio was varied. At a fixed flux, the temperature had little effect on particle shape. For example, in the eutectic composition, low flux melting temperature allowed for efficient diffusion of raw materials and the thermodynamically favorable (111) facets to dominate, producing octahedral particles. Truncation resulting in (100) surfaces did occur at higher temperatures as slower forming facets continued to grow. Pure LiCl salt was able to stabilize higher energy facets and produced plate-like particles with predominant $(11\bar{2})$ surfaces.[103] **Figure 1-11b** summarizes the molten salt composition dependence of the morphology.

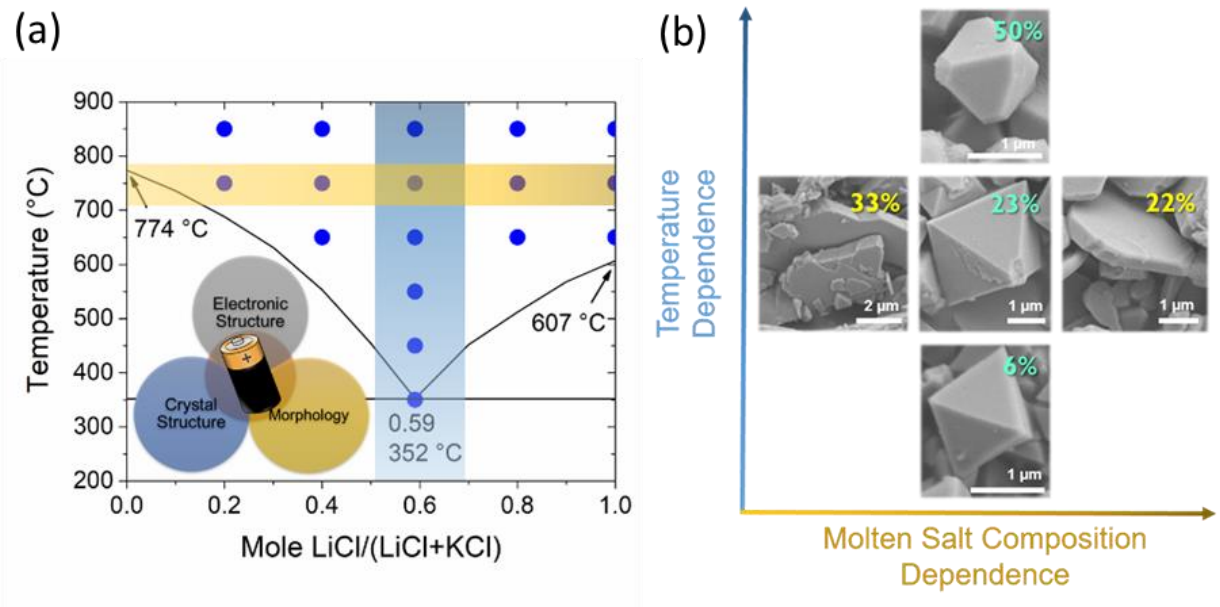

Figure 1-11. (a) LiCl−KCl molten salt phase diagram illustrating tunable synthesis parameters. Insert: material properties influencing electrochemical performance. **(b)** Selected SEM images to illustrate temperature-dependent and molten salt composition-dependent particle morphologies and Mn^{3+} contents. Particle sizes are not representative. Modified with permission from reference [104]. Copyright 2020, American Chemical Society.

1.4.2. Crystallographic and Electronic Structure Control

The cation ordering and Mn oxidation state of LNMO are highly dependent on synthesis temperature. Tuning the synthesis temperature above and below the reported transition metal ordering transition temperature of 700 °C was used to tune crystallographic and electronic structures. The electrochemically active Mn^{3+} content can be estimated by measuring the percentage of total capacity obtained in the voltage plateau from 3.8 to 4.25 V vs Li/Li^+ during electrochemical cycling. While salt composition significantly influenced morphology, the temperature had a much larger effect on Mn^{3+} content and cation ordering. **Figure 1-11b** summarizes the percentage of Mn^{3+} in samples prepared under different molten salt conditions.

Synchrotron soft X-ray absorption spectroscopy (XAS) is capable of probing transition metal oxidation states with element specificity and surface sensitivity.[106] The Mn L-edge was also used to estimate Mn^{3+} percentage and revealed that higher synthesis temperatures produced samples with more reduced Mn (**Figure 1-12a**). The electrochemical cycling data shows that while the higher temperatures increased the Mn^{3+}/Mn^{4+} voltage plateau, the total capacity decreased significantly due to severe structural disordering and the formation of electrochemically inactive impurity phases (**Figure 1-12b**). From **Figure 1-12c**, the rate performance is also shown to be dependent on Mn^{3+} content, but it is a non-linear relationship as the sample synthesized at 750 °C showed the best high-rate capacity retention due to optimal Mn^{3+} and transition metal disordering. This study demonstrates that the molten salt synthesis method can be used to rationally design LNMO materials with specific surface facets and controllable amounts of Mn^{3+}. This is useful for optimizing materials performance or for further studies on the influence of properties on electrochemical behavior, which will be explored in the following chapters.

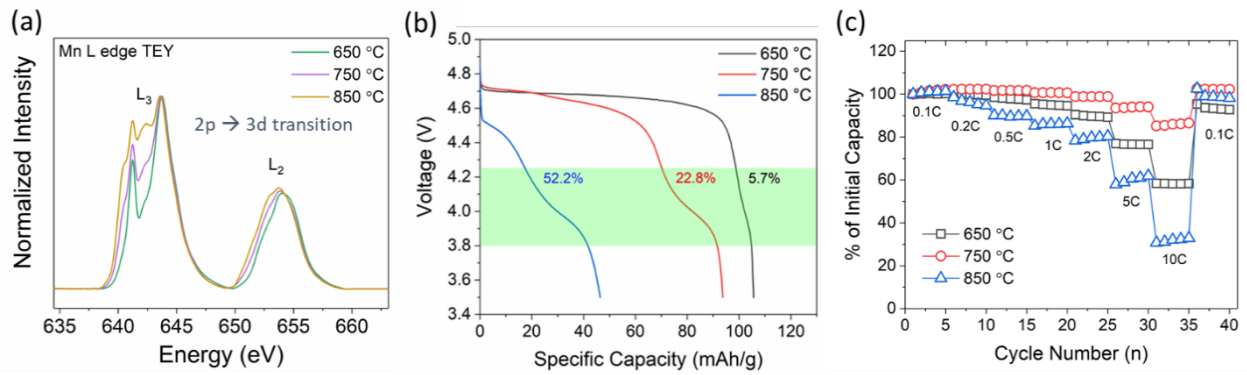

Figure 1-12. (a) Mn L-edge soft XAS spectra in TEY collection mode of LNMO synthesized at different temperatures illustrating decreasing Mn oxidation state as temperatures increase. **(b)** Discharge profiles of LNMO synthesized at different temperatures illustrating increased capacity contribution in the 3.8 – 4.25 V vs Li/Li^+ region due to the Mn redox as temperatures increase.

Cells were cycled at room temperature from 3.5- 4.9 V vs Li/Li^+ at 0.1C. **(c)** Rate capability testing with normalized initial capacities for LNMO synthesized at different temperatures. Cells were charged at 0.1 C and discharged at the indicated C-rates where 1 C = 147 mAh/g. Modified with permission from reference [104]. Copyright 2020, American Chemical Society.

1.4.3. Characterizing Chemical and Structural Heterogeneities

Advanced characterization of tunable LNMO materials is required for in-depth understanding of kinetic, chemomechanical, and structural properties. The XRD patterns of ordered and disordered crystal structures are almost indistinguishable with lab-based diffractometers using Cu Kα energy. The lower symmetry of the ordered $P4_332$ phase leads to the presence of low intensity superlattice Bragg diffraction peaks. Most peaks are still difficulty to discern even with synchrotron sources, which provide continuously tunable, high energy X-rays (**Figure 1-13)**; however, slight changes in the lattice parameter arise due to Mn^{3+} present in the disordered phase. Several studies have focused on quantifying the more obvious structural changes during the Li removal. *In situ* XRD has been used to study the transformation of the three-cubic phases during Li removal in LNMO revealing two and three phase coexistence and solid solution behaviors.[65] Phase transformations were further studied and correlated to the degree of Li removal at the mesoscale in single crystals though hard X-ray full-field transition microscopy imaging combined with X-ray absorption near-edge structure (FF-TXM-XANES).[64] **Figure 1-14** illustrates Ni oxidation state mapping measured by FF-TXM-XANES in an ordered LNMO single-crystal at 50% SOC.[64] Differences in the oxidation state throughout the particle indicate that Li^+ removal is initiated at one edge or corner site and then propagates throughout the bulk of the particle. Operando XRD combined with computed tomography (XRD-CT) has been used to spatially

quantify crystallographic heterogeneities in spinel $Li_xMn_2O_4$ through tracking of the lattice parameter variation.[61] Both inter-particle stoichiometric differences and intra-particle stoichiometric gradients and phase heterogeneities were observed illustrating different particle responses to lithiation.

Synchrotron X-ray nanodiffraction mapping combining microscopy and structural analysis has been employed to study LCO materials to understand the influence of inherent structural and chemical defects on performance.[107] This technique allows for high-resolution mapping of defects and distortions at the individual particle level and is a particularly useful platform to study the structurally complex high-voltage LNMO. Throughout this work, we will utilize nanodiffraction, developing experiments to study inherent phase distributions and dynamic phase transformations through strain monitoring.

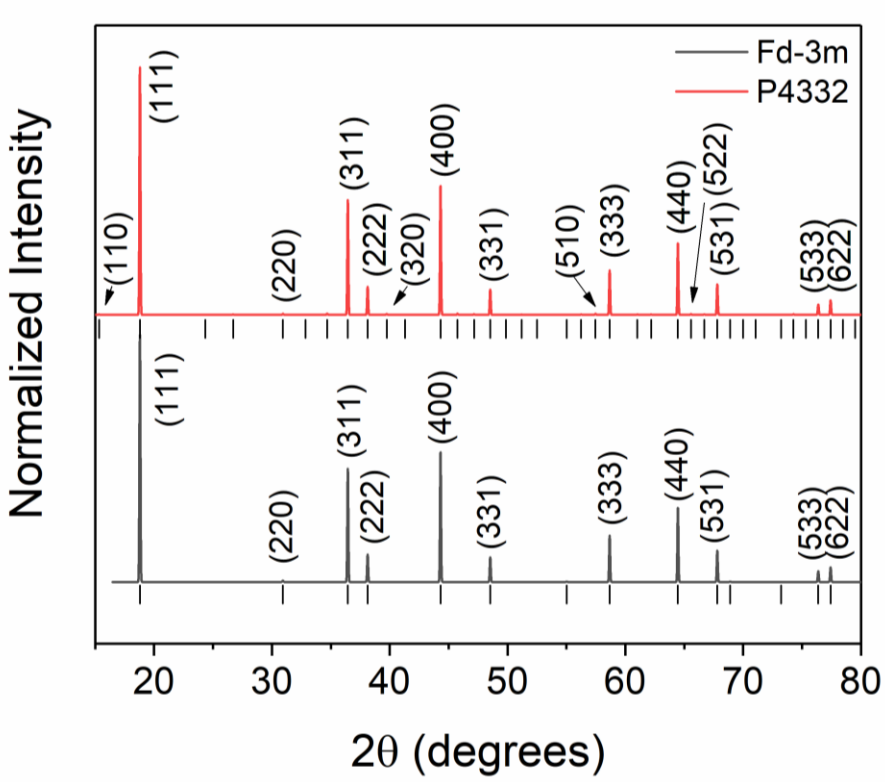

Figure 1-13. Synchrotron powder X-ray diffraction patterns of ordered ($P4_332$) and disordered ($Fd\bar{3}m$) spinel LNMO converted to Cu Kα energy.

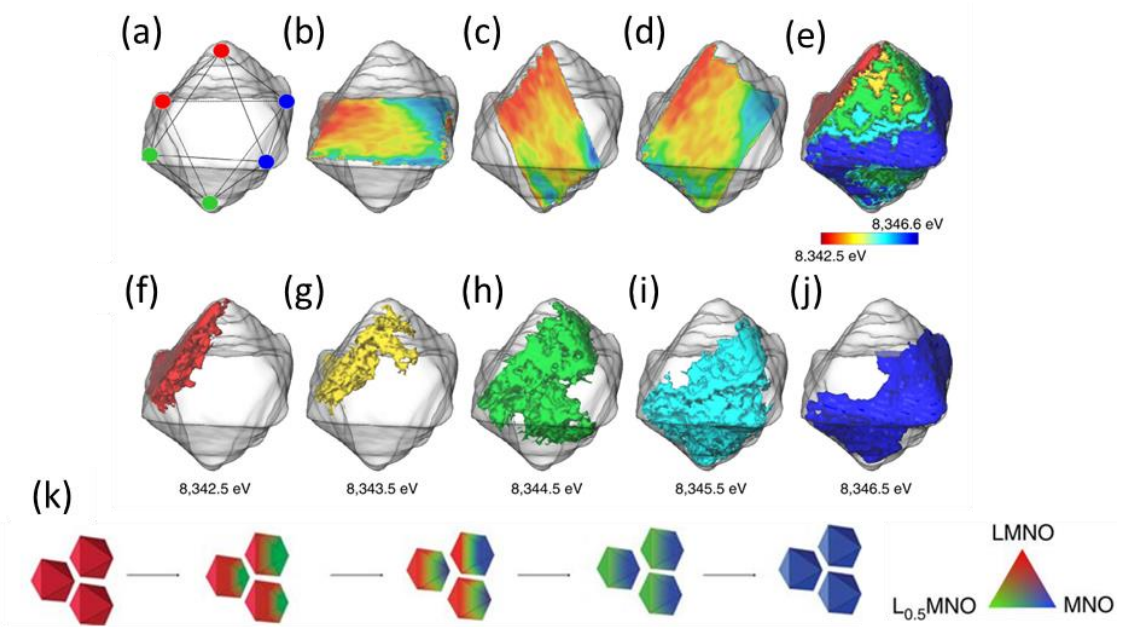

Figure 1-14. Three-dimensional map of Ni oxidation state in 50% delithiated LNMO measured by hard X-ray full-field transition microscopy combined with X-ray absorption near-edge structure (FF-TXM-XANES). **(a-d)** horizontal and diagonal slices. **(e-j)** Color-coded charge heterogeneity. **(k)** Schematic of three-phase transformation mechanism. Modified from reference [64].

1.5. Conclusions

While LNMO represents a promising Co-free, high-voltage cathode material, its commercialization is hindered by Mn dissolution leading to poor full-cell cycling stability and the lack of compatible electrolytes. Furthermore, the structural properties are complex leading to chemical and structural heterogeneities that can hinder Li^+ transportation. **Chapter 2** of this work systematically explores molten salt synthesis conditions and their influence on particle size, uniformity, and cycling performance. In **Chapter 3**, inherent particle structural heterogeneity is compared in samples prepared under different synthetic conditions using X-ray nanodiffraction. In **Chapter 4** and **Chapter 5**, the nanodiffraction technique is further developed to measure lattice

strain and distortion evolution under chemical delithiation and *in situ* electrochemical cycling conditions, respectively. These studies explore and discuss methods to study heterogeneities at different length scales and under different conditions in cathode materials. Finally, **Chapter 6** discusses perspectives for the future of high-voltage spinel cathode materials design and characterization including synthesis optimization, modification strategies, further applications, advanced characterization requirements.

1.6. References

(1) Armand, M.; Tarascon, J. M. Building Better Batteries. *Nature* **2008**, *451* (7179), 652–657.

(2) Fergus, J. W. Recent Developments in Cathode Materials for Lithium Ion Batteries. *J. Power Sources* **2010**, *195*, 939–954.

(3) Whittingham, M. S. Lithium Batteries and Cathode Materials. *Chem. Rev.* **2004**, *104* (10), 4271–4301.

(4) Mizushima, K.; Jones, P. C.; Wiseman, P. J.; Goodenough, J. B. LixCoO2 (0<x<-1): A New Cathode Material for Batteries of High Energy Density. *Mater. Res. Bull.* **1980**, *15* (6), 783–789.

(5) Ozawa, K. Lithium-Ion Rechargeable Batteries with LiCoO2 and Carbon Electrodes: The LiCoO2/C System. *Solid State Ionics* **1994**, *69* (3–4), 212–221.

(6) Tarascon, J. M.; Armand, M. Issues and Challenges Facing Rechargeable Lithium Batteries. *Nature* **2001**, *414* (6861), 359–367.

(7) Liu, Z.; Yu, A.; Lee, J. Y. Synthesis and Characterization of LiNi1-x-YCoxMnyO2 as the Cathode Materials of Secondary Lithium Batteries. *J. Power Sources* **1999**, *81–82*, 416–419.

(8) Madhavi, S.; Subba Rao, G. V.; Chowdari, B. V. R.; Li, S. F. Y. Effect of Aluminum Doping on Cathodic Behaviour of LiNi0.7Co0.3O2. *J. Power Sources* **2001**, *93* (1–2), 156–162.

(9) Lin, F.; Markus, I. M.; Nordlund, D.; Weng, T. C.; Asta, M. D.; Xin, H. L.; Doeff, M. M. Surface Reconstruction and Chemical Evolution of Stoichiometric Layered Cathode Materials for Lithium-Ion Batteries. *Nat. Commun.* **2014**, *5*, 3529.

(10) Padhi, A. K.; Nanjundaswamy, K. S.; Goodenough, J. B. Phospho-olivines as Positive-Electrode Materials for Rechargeable Lithium Batteries. *J. Electrochem. Soc.* **1997**, *144* (4), 1188–1194.

(11) Thackeray, M. M.; David, W. I. F.; Bruce, P. G.; Goodenough, J. B. Lithium Insertion into Manganese Spinels. *Mater. Res. Bull.* **1983**, *18* (4), 461–472.

(12) Thackeray, M. M. Manganese Oxides for Rechargeable Lithium Batteries. *Prog. Solid State Chem.* **1997**, *25* (1–2), 1–75.

(13) Liu, D.; Zhu, W.; Trottier, J.; Gagnon, C.; Barray, F.; Guerfi, A.; Mauger, A.; Groult, H.; Julien, C. M.; Goodenough, J. B.; Zaghib, K. Spinel Materials for High-Voltage Cathodes in Li-Ion Batteries. *RSC Adv.* **2014**, *4* (1), 154–167.

(14) Amine, K.; Tukamoto, H.; Yasuda, H.; Fujita, Y. Preparation and Electrochemical Investigation of LiMn2 − XMexO4 (Me: Ni, Fe, and x = 0.5, 1) Cathode Materials for Secondary Lithium Batteries. *J. Power Sources* **1997**, *68* (2), 604–608.

(15) Zhong, Q. Synthesis and Electrochemistry of LiNixMn2−xO4. *J. Electrochem. Soc.* **1997**, *144* (1), 205.

(16) Rana, J.; Glatthaar, S.; Gesswein, H.; Sharma, N.; Binder, J. R.; Chernikov, R.; Schumacher, G.; Banhart, J. Local Structural Changes in LiMn1.5Ni0.5O4 Spinel Cathode Material for Lithium-Ion Batteries. *J. Power Sources* **2014**, *255*, 439–449.

(17) Kam, K. C.; Doeff, M. M. Electrode Materials for Lithium Ion Batteries. *Mater. Matters* **2012**, *7* (4), 56–58.

(18) Muralidharan, N.; Self, E. C.; Dixit, M.; Du, Z.; Essehli, R.; Amin, R.; Nanda, J.; Belharouak, I.; Muralidharan, N.; Dixit, M.; Du, Z.; Essehli, R.; Amin, R.; Belharouak, I.; Self, E. C.; Nanda, J. Next-Generation Cobalt-Free Cathodes – A Prospective Solution to the Battery Industry's Cobalt Problem. *Adv. Energy Mater.* **2022**, *12* (9), 2103050.

(19) Chagnes, A.; Pospiech, B. A Brief Review on Hydrometallurgical Technologies for Recycling Spent Lithium-Ion Batteries. *Journal of Chemical Technology and Biotechnology*. John Wiley & Sons, Ltd July 1, 2013, pp 1191–1199.

(20) Dühnen, S.; Betz, J.; Kolek, M.; Schmuch, R.; Winter, M.; Placke, T. Toward Green Battery Cells: Perspective on Materials and Technologies. *Small Methods* **2020**, *4* (7), 2000039.

(21) Nitta, N.; Wu, F.; Lee, J. T.; Yushin, G. Li-Ion Battery Materials: Present and Future. *Materials Today*. Elsevier B.V. June 1, 2015, pp 252–264.

(22) Yang, Z.; Huang, H.; Lin, F.; Yang, Z.; Lin, F.; Huang, H. Sustainable Electric Vehicle Batteries for a Sustainable World: Perspectives on Battery Cathodes, Environment, Supply Chain, Manufacturing, Life Cycle, and Policy. *Adv. Energy Mater.* **2022**, *12* (26), 2200383.

(23) Langdon, J.; Manthiram, A. A Perspective on Single-Crystal Layered Oxide Cathodes for Lithium-Ion Batteries. *Energy Storage Mater.* **2021**, *37*, 143–160.

(24) Zhu, J.; Chen, G. Single-Crystal Based Studies for Correlating the Properties and High-Voltage Performance of Li[NixMnyCo1-x-y]O2 Cathodes. *J. Mater. Chem. A* **2019**, *7* (10), 5463–5474.

(25) Xu, H.; Zhu, J.; Finegan, D. P.; Zhao, H.; Lu, X.; Li, W.; Hoffman, N.; Bertei, A.; Shearing, P.; Bazant, M. Z. Guiding the Design of Heterogeneous Electrode Microstructures for Li-Ion Batteries: Microscopic Imaging, Predictive Modeling, and Machine Learning. *Adv. Energy Mater.* **2021**, *11* (19), 2003908.

(26) Li, W.; Cho, Y.-G. G.; Yao, W.; Li, Y.; Cronk, A.; Shimizu, R.; Schroeder, M. A.; Fu, Y.; Zou, F.; Battaglia, V.; Manthiram, A.; Zhang, M.; Meng, Y. S. Enabling High Areal Capacity for Co-Free High Voltage Spinel Materials in next-Generation Li-Ion Batteries. *J. Power Sources* **2020**, *473*, 228579.

(27) Xu, Z.; Rahman, M. M.; Mu, L.; Liu, Y.; Lin, F. Chemomechanical Behaviors of Layered Cathode Materials in Alkali Metal Ion Batteries. *J. Mater. Chem. A* **2018**, *6* (44), 21859–21884.

(28) Liu, H.; Wolf, M.; Karki, K.; Yu, Y. S.; Stach, E. A.; Cabana, J.; Chapman, K. W.; Chupas, P. J. Intergranular Cracking as a Major Cause of Long-Term Capacity Fading of Layered Cathodes. *Nano Lett.* **2017**, *17* (6), 3452–3457.

(29) Ryu, H. H.; Park, K. J.; Yoon, C. S.; Sun, Y. K. Capacity Fading of Ni-Rich Li[NixCoyMn1-x-y]O2 ($0.6 \leq x \leq 0.95$) Cathodes for High-Energy-Density Lithium-Ion Batteries: Bulk or Surface Degradation? *Chem. Mater.* **2018**, *30* (3), 1155–1163.

(30) Min, K.; Cho, E. Intrinsic Origin of Intra-Granular Cracking in Ni-Rich Layered Oxide Cathode Materials. *Phys. Chem. Chem. Phys.* **2018**, *20* (14), 9045–9052.

(31) Arora, P. Capacity Fade Mechanisms and Side Reactions in Lithium-Ion Batteries. *J. Electrochem. Soc.* **1998**, *145* (10), 3647.

(32) Xu, Z.; Jiang, Z.; Kuai, C.; Xu, R.; Qin, C.; Zhang, Y.; Rahman, M. M.; Wei, C.; Nordlund, D.; Sun, C. J.; Xiao, X.; Du, X. W.; Zhao, K.; Yan, P.; Liu, Y.; Lin, F. Charge Distribution Guided by Grain Crystallographic Orientations in Polycrystalline Battery Materials. *Nat. Commun.* **2020**, *11* (1), 83.

(33) Qian, G.; Zhang, Y.; Li, L.; Zhang, R.; Xu, J.; Cheng, Z.; Xie, S.; Wang, H.; Rao, Q.; He, Y.; Shen, Y.; Chen, L.; Tang, M.; Ma, Z. F. Single-Crystal Nickel-Rich Layered-Oxide Battery Cathode Materials: Synthesis, Electrochemistry, and Intra-Granular Fracture. *Energy Storage Mater.* **2020**, *27*, 140–149.

(34) Kim, J.; Lee, H.; Cha, H.; Yoon, M.; Park, M.; Cho, J. Prospect and Reality of Ni-Rich Cathode for Commercialization. *Adv. Energy Mater.* **2018**, *8* (6).

(35) Li, J.; Cameron, A. R.; Li, H.; Glazier, S.; Xiong, D.; Chatzidakis, M.; Allen, J.; Botton, G. A.; Dahn, J. R. Comparison of Single Crystal and Polycrystalline LiNi 0.5 Mn 0.3 Co 0.2 O 2 Positive Electrode Materials for High Voltage Li-Ion Cells. *J. Electrochem. Soc.* **2017**, *164* (7), A1534–A1544.

(36) Fan, X.; Hu, G.; Zhang, B.; Ou, X.; Zhang, J.; Zhao, W.; Jia, H.; Zou, L.; Li, P.; Yang, Y. Crack-Free Single-Crystalline Ni-Rich Layered NCM Cathode Enable Superior Cycling Performance of Lithium-Ion Batteries. *Nano Energy* **2020**, *70*, 104450.

(37) Cheng, L.; Zhang, B.; Su, S. L.; Ming, L.; Zhao, Y.; Wang, C. H.; Ou, X. Comparison of Monocrystalline and Secondary LiNi0.5Co0.2Mn0.3O2 Cathode Material for High-Performance Lithium-Ion Batteries. *J. Alloys Compd.* **2020**, *845*.

(38) Weber, R.; Fell, C. R.; Dahn, J. R.; Hy, S. Operando X-Ray Diffraction Study of Polycrystalline and Single-Crystal Li x Ni 0.5 Mn 0.3 Co 0.2 O 2. *J. Electrochem. Soc.* **2017**, *164* (13), A2992–A2999.

(39) Chemelewski, K. R.; Lee, E. S.; Li, W.; Manthiram, A. Factors Influencing the Electrochemical Properties of High-Voltage Spinel Cathodes: Relative Impact of Morphology and Cation Ordering. *Chem. Mater.* **2013**, *25* (14), 2890–2897.

(40) Cabana, J.; Zheng, H.; Shukla, A. K.; Kim, C.; Battaglia, V. S.; Kunduraci, M. Comparison of the Performance of LiNi1/2Mn3/2O4 with Different Microstructures. *J. Electrochem. Soc.* **2011**, *158* (9), A997.

(41) Liu, G.; Li, M.; Wu, N.; Cui, L.; Huang, X.; Liu, X.; Zhao, Y.; Chen, H.; Yuan, W.; Bai, Y. Single-Crystalline Particles: An Effective Way to Ameliorate the Intragranular Cracking, Thermal Stability, and Capacity Fading of the LiNi 0.6 Co 0.2 Mn 0.2 O 2 Electrodes. *J. Electrochem. Soc.* **2018**, *165* (13), A3040–A3047.

(42) Zhang, F.; Lou, S.; Li, S.; Yu, Z.; Liu, Q.; Dai, A.; Cao, C.; Toney, M. F.; Ge, M.; Xiao, X.; Lee, W. K.; Yao, Y.; Deng, J.; Liu, T.; Tang, Y.; Yin, G.; Lu, J.; Su, D.; Wang, J. Surface Regulation Enables High Stability of Single-Crystal Lithium-Ion Cathodes at High Voltage. *Nat. Commun.* **2020**, *11* (1).

(43) Santhanam, R.; Rambabu, B. Research Progress in High Voltage Spinel LiNi0.5Mn1.5O4 Material. *J. Power Sources* **2010**, *195* (17), 5442–5451.

(44) Patoux, S.; Daniel, L.; Bourbon, C.; Lignier, H.; Pagano, C.; Le Cras, F.; Jouanneau, S.; Martinet, S. High Voltage Spinel Oxides for Li-Ion Batteries: From the Material Research to the Application. *J. Power Sources* **2009**, *189* (1), 344–352.

(45) Huang, Y.; Dong, Y.; Li, S.; Lee, J.; Wang, C.; Zhu, Z.; Xue, W.; Li, Y.; Li, J. Lithium Manganese Spinel Cathodes for Lithium-Ion Batteries. *Adv. Energy Mater.* **2020**, 2000997.

(46) Kim, J. H.; Yoon, C. S.; Myung, S. T.; Prakash, J.; Sun, Y. K. Phase Transitions in Li1-ΔNi0.5Mn 1.5O4 during Cycling at 5 V. *Electrochem. Solid-State Lett.* **2004**, *7* (7), A216.

(47) Kim, J. H.; Myung, S. T.; Yoon, C. S.; Kang, S. G.; Sun, Y. K. Comparative Study of LiNi0.5Mn1.5O 4-δ and LiNi0.5Mn1.5O4 Cathodes Having Two Crystallographic Structures: Fd3m and P4332. *Chem. Mater.* **2004**, *16* (5), 906–914.

(48) Kim, S.; Hegde, V. I.; Yao, Z.; Lu, Z.; Amsler, M.; He, J.; Hao, S.; Croy, J. R.; Lee, E.; Thackeray, M. M.; Wolverton, C. First-Principles Study of Lithium Cobalt Spinel Oxides: Correlating Structure and Electrochemistry. *ACS Appl. Mater. Interfaces* **2018**, *10* (16), 13479–13490.

(49) Greco, G.; Brutti, S.; Vitucci, F. M.; Lombardo, L.; Köntje, M.; Savoini, A.; Paolone, A.; Panero, S. Investigation of the Chemical Disorder of LiNi 0.5 Mn 1.5 O 4 Lattice by Means of Extended X-Ray Absorption Fine Structure Spectroscopy. *J. Phys. Chem. C* **2014**, *118* (46), 26471–26478.

(50) Chen, Y.; Sun, Y.; Huang, X. Origin of the Ni/Mn Ordering in High-Voltage Spinel LiNi0.5Mn1.5O4: The Role of Oxygen Vacancies and Cation Doping. *Comput. Mater. Sci.* **2016**, *115*, 109–116.

(51) Jafta, C. J.; Mathe, M. K.; Manyala, N.; Roos, W. D.; Ozoemena, K. I. Microwave-Assisted Synthesis of High-Voltage Nanostructured LiMn 1.5Ni0.5O4 Spinel: Tuning the Mn3+ Content and Electrochemical Performance. *ACS Appl. Mater. Interfaces* **2013**, *5* (15), 7592–7598.

(52) Kunduraci, M.; Al-Sharab, J. F.; Amatucci, G. G. High-Power Nanostructured LiMn2-XNixO4 High-Voltage Lithium-Ion Battery Electrode Materials: Electrochemical Impact of Electronic Conductivity and Morphology. *Chem. Mater.* **2006**, *18* (15), 3585–3592.

(53) Aktekin, B.; Valvo, M.; Smith, R. I.; Sørby, M. H.; Lodi Marzano, F.; Zipprich, W.; Brandell, D.; Edström, K.; Brant, W. R. Cation Ordering and Oxygen Release in LiNi0.5-XMn1.5+ XO4-y (LNMO): In Situ Neutron Diffraction and Performance in Li Ion Full Cells. *ACS Appl. Energy Mater.* **2019**, *2* (5), 3323–3335.

(54) Sun, H.; Hu, A.; Spence, S.; Kuai, C.; Hou, D.; Mu, L.; Liu, J.; Li, L.; Sun, C.; Sainio, S.; Nordlund, D.; Luo, W.; Huang, Y.; Lin, F. Tailoring Disordered/Ordered Phases to Revisit the Degradation Mechanism of High-Voltage LiNi0.5Mn1.5O4 Spinel Cathode Materials. *Adv. Funct. Mater.* **2022**, 2112279.

(55) Song, J.; Shin, D. W.; Lu, Y.; Amos, C. D.; Manthiram, A.; Goodenough, J. B. Role of Oxygen Vacancies on the Performance of Li[Ni 0.5-XMn 1.5+ x]O 4 (x = 0, 0.05, and 0.08) Spinel Cathodes for Lithium-Ion Batteries. *Chem. Mater.* **2012**, *24* (15), 3101–3109.

(56) Duncan, H.; Hai, B.; Leskes, M.; Grey, C. P.; Chen, G. Relationships between Mn3+ Content, Structural Ordering, Phase Transformation, and Kinetic Properties in LiNixMn2-

XO4 Cathode Materials. *Chem. Mater.* **2014**, *26* (18), 5374–5382.

(57) Kan, W. H.; Kuppan, S.; Cheng, L.; Doeff, M.; Nanda, J.; Huq, A.; Chen, G. Crystal Chemistry and Electrochemistry of LixMn1.5Ni0.5O4 Solid Solution Cathode Materials. *Chem. Mater.* **2017**, *29* (16), 6818–6828.

(58) Manthiram, A.; Chemelewski, K.; Lee, E. S. A Perspective on the High-Voltage LiMn1.5Ni0.5O 4 Spinel Cathode for Lithium-Ion Batteries. *Energy Environ. Sci.* **2014**, *7* (4), 1339–1350.

(59) Moorhead-Rosenberg, Z.; Shin, D. W.; Chemelewski, K. R.; Goodenough, J. B.; Manthiram, A. Quantitative Determination of Mn 3 Content in LiMn 1.5Ni 0.5O 4 Spinel Cathodes by Magnetic Measurements. *Appl. Phys. Lett.* **2012**, *100* (21).

(60) Amdouni, N.; Zaghib, K.; Gendron, F.; Mauger, A.; Julien, C. M. Structure and Insertion Properties of Disordered and Ordered LiNi 0.5Mn1.5O4 Spinels Prepared by Wet Chemistry. *Ionics (Kiel).* **2006**, *12* (2), 117–126.

(61) Finegan, D. P.; Vamvakeros, A.; Tan, C.; Heenan, T. M. M.; Daemi, S. R.; Seitzman, N.; Di Michiel, M.; Jacques, S.; Beale, A. M.; Brett, D. J. L.; Shearing, P. R.; Smith, K. Spatial Quantification of Dynamic Inter and Intra Particle Crystallographic Heterogeneities within Lithium Ion Electrodes. *Nat. Commun.* **2020**, *11* (1), 631.

(62) Kim, J. H.; Huq, A.; Chi, M.; Pieczonka, N. P. W.; Lee, E.; Bridges, C. A.; Tessema, M. M.; Manthiram, A.; Persson, K. A.; Powell, B. R. Integrated Nano-Domains of Disordered and Ordered Spinel Phases in LiNi0.5Mn1.5O4 for Li-Ion Batteries. *Chem. Mater.* **2014**, *26* (15), 4377–4386.

(63) Spence, S. L.; Hu, A.; Jiang, M.; Xu, Z.; Yang, Z.; Rahman, M. M.; Li, L.; Chu, Y. S.; Xiao, X.; Huang, X.; Lin, F. Mapping Lattice Distortions in LiNi 0.5 Mn 1.5 O 4 Cathode Materials. *ACS Energy Lett.* **2022**, 690–695.

(64) Kuppan, S.; Xu, Y.; Liu, Y.; Chen, G. Phase Transformation Mechanism in Lithium Manganese Nickel Oxide Revealed by Single-Crystal Hard X-Ray Microscopy. *Nat. Commun.* **2017**, *8*, 14309.

(65) Saravanan, K.; Jarry, A.; Kostecki, R.; Chen, G. A Study of Roomerature LixMn1.5Ni0.5O4 Solid Solutions. *Sci. Rep.* **2015**, *5* (1), 8027.

(66) Yoon, J.; Kim, D.; Um, J. H.; Jeong, M.; Oh, W.; Yoon, W. S. Effect of Local Structural Changes on Rate Capability of LiNi0.5Mn1.5O4-δ Cathode Material for Lithium Ion Batteries. *J. Alloys Compd.* **2016**, *686*, 593–600.

(67) Moorhead-Rosenberg, Z.; Huq, A.; Goodenough, J. B.; Manthiram, A. Electronic and Electrochemical Properties of Li1-XMn1.5Ni0.5O4 Spinel Cathodes As a Function of Lithium Content and Cation Ordering. *Chem. Mater.* **2015**, *27* (20), 6934–6945.

(68) Zheng, J.; Xiao, J.; Yu, X.; Kovarik, L.; Gu, M.; Omenya, F.; Chen, X.; Yang, X. Q.; Liu, J.; Graff, G. L.; Whittingham, M. S.; Zhang, J. G. Enhanced Li + Ion Transport in LiNi 0.5Mn 1.5O 4 through Control of Site Disorder. *Phys. Chem. Chem. Phys.* **2012**, *14* (39), 13515–13521.

(69) Hunter, J. C. Preparation of a New Crystal Form of Manganese Dioxide: λ-MnO2. *J. Solid State Chem.* **1981**, *39* (2), 142–147.

(70) Gummow, R. J.; de Kock, A.; Thackeray, M. M. Improved Capacity Retention in Rechargeable 4 V Lithium/Lithium-Manganese Oxide (Spinel) Cells. *Solid State Ionics* **1994**, *69* (1), 59–67.

(71) Benedek, R.; Thackeray, M. M. Reaction Energy for LiMn 2O 4 Spinel Dissolution in Acid. *Electrochem. Solid-State Lett.* **2006**, *9* (6).

(72) Pieczonka, N. P. W.; Liu, Z.; Lu, P.; Olson, K. L.; Moote, J.; Powell, B. R.; Kim, J.-H. Understanding Transition-Metal Dissolution Behavior in LiNi 0.5 Mn 1.5 O 4 High-Voltage Spinel for Lithium Ion Batteries. *J. Phys. Chem. C* **2013**, 117–15947.

(73) Shilina, Y.; Ziv, B.; Meir, A.; Banerjee, A.; Ruthstein, S.; Luski, S.; Aurbach, D.; Halalay, I. C. Combined Electron Paramagnetic Resonance and Atomic Absorption Spectroscopy/Inductively Coupled Plasma Analysis As Diagnostics for Soluble Manganese Species from Mn-Based Positive Electrode Materials in Li-Ion Cells. *Anal. Chem.* **2016**, *88* (8), 4440–4447.

(74) Peled, E. The Electrochemical Behavior of Alkali and Alkaline Earth Metals in Nonaqueous Battery Systems—The Solid Electrolyte Interphase Model. *J. Electrochem. Soc.* **1979**, *126* (12), 2047–2051.

(75) Julien, C. M.; Mauger, A. Review of 5-V Electrodes for Li-Ion Batteries: Status and Trends. *Ionics (Kiel).* **2013**, *19* (7), 951–988.

(76) Xu, X. L.; Deng, S. X.; Wang, H.; Liu, J. B.; Yan, H. Research Progress in Improving the Cycling Stability of High-Voltage LiNi0.5Mn1.5O4 Cathode in Lithium-Ion Battery. *Nano-Micro Lett.* **2017**, *9* (2), 1–19.

(77) Tang, D.; Sun, Y.; Yang, Z.; Ben, L.; Gu, L.; Huang, X. Surface Structure Evolution of LiMn2O4 Cathode Material upon Charge/Discharge. *Chem. Mater.* **2014**, *26* (11), 3535–3543.

(78) Wang, L.-F.; Ou, C.-C.; Striebel, K. A.; Chen, J.-S. Study of Mn Dissolution from LiMn2O4 Spinel Electrodes Using Rotating Ring-Disk Collection Experiments. *J. Electrochem. Soc.* **2003**, *150* (7), A905.

(79) Cui, Z.; Zou, F.; Celio, H.; Manthiram, A.; Cui, Z.; Zou, F.; Celio, H.; Manthiram, A. Paving Pathways Toward Long-Life Graphite/LiNi0.5Mn1.5O4 Full Cells: Electrochemical and Interphasial Points of View. *Adv. Funct. Mater.* **2022**, 2203779.

(80) Houache, M. S. E.; Yim, C. On the Current and Future Outlook of Battery Chemistries for Electric Vehicles — Mini Review. **2023**.

(81) Yu, X.; Yu, W. A.; Manthiram, A. Advances and Prospects of High-Voltage Spinel Cathodes for Lithium-Based Batteries. *Small Methods* **2021**, *5* (5), 1–30.

(82) Chemelewski, K. R.; Li, W.; Gutierrez, A.; Manthiram, A. High-Voltage Spinel Cathodes for Lithium-Ion Batteries: Controlling the Growth of Preferred Crystallographic Planes through Cation Doping. *J. Mater. Chem. A* **2013**, *1* (48), 15334–15341.

(83) Wang, Y.; Wang, E.; Zhang, X.; Yu, H. High-Voltage "Single-Crystal" Cathode Materials for Lithium-Ion Batteries. *Energy and Fuels* **2021**, *35* (3), 1918–1932.

(84) Lin, H. B.; Zhang, Y. M.; Rong, H. B.; Mai, S. W.; Hu, J. N.; Liao, Y. H.; Xing, L. D.; Xu,

M. Q.; Li, X. P.; Li, W. S. Crystallographic Facet- and Size-Controllable Synthesis of Spinel LiNi 0.5Mn1.5O4 with Excellent Cyclic Stability as Cathode of High Voltage Lithium Ion Battery. *J. Mater. Chem. A* **2014**, *2* (30), 11987–11995.

(85) Kuppan, S.; Duncan, H.; Chen, G. Controlling Side Reactions and Self-Discharge in High-Voltage Spinel Cathodes: The Critical Role of Surface Crystallographic Facets. *Phys. Chem. Chem. Phys.* **2015**, *17* (39), 26471–26481.

(86) Chen, Z.; Zhao, R.; Du, P.; Hu, H.; Wang, T.; Zhu, L.; Chen, H. Polyhedral LiNi0.5Mn1.5O4 with Excellent Electrochemical Properties for Lithium-Ion Batteries. *J. Mater. Chem. A* **2014**, *2* (32), 12835–12848.

(87) Liu, H.; Zhang, X.; He, X.; Senyshyn, A.; Wilken, A.; Zhou, D.; Fromm, O.; Niehoff, P.; Yan, B.; Li, J.; Muehlbauer, M.; Wang, J.; Schumacher, G.; Paillard, E.; Winter, M.; Li, J. Truncated Octahedral High-Voltage Spinel LiNi0.5Mn1.5O4 Cathode Materials for Lithium Ion Batteries: Positive Influences of Ni/Mn Disordering and Oxygen Vacancies. *J. Electrochem. Soc.* **2018**, *165* (9), A1886–A1896.

(88) Cabana, J.; Casas-Cabanas, M.; Omenya, F. O.; Chernova, N. A.; Zeng, D.; Whittingham, M. S.; Grey, C. P. Composition-Structure Relationships in the Li-Ion Battery Electrode Material LiNi0.5Mn1.5O4. *Chem. Mater.* **2012**, *24* (15), 2952–2964.

(89) Cai, Y.; Huang, S. Z.; She, F. S.; Liu, J.; Zhang, R. L.; Huang, Z. H.; Wang, F. Y.; Wang, H. E. Facile Synthesis of Well-Shaped Spinel LiNi0.5Mn1.5O4 Nanoparticles as Cathode Materials for Lithium Ion Batteries. *RSC Adv.* **2016**, *6* (4), 2785–2792.

(90) Xiao, J.; Chen, X.; Sushko, P. V.; Sushko, M. L.; Kovarik, L.; Feng, J.; Deng, Z.; Zheng, J.; Graff, G. L.; Nie, Z.; Choi, D.; Liu, J.; Zhang, J.-G.; Whittingham, M. S. High-Performance $LiNi_{0.5}Mn_{1.5}O_4$ Spinel Controlled by Mn^{3+} Concentration and Site Disorder. *Adv. Mater.* **2012**, *24* (16), 2109–2116.

(91) Shu, Y.; Xie, Y.; Yan, W.; Meng, S.; Sun, D.; Jin, Y.; He, K. Synergistic Effect of Surface Plane and Particle Sizes on the Electrochemical Performance of LiNi0.5Mn1.5O4 Cathode Material via a Facile Calcination Process. *J. Power Sources* **2019**, *433*, 226708.

(92) Casas-Cabanas, M.; Kim, C.; Rodríguez-Carvajal, J.; Cabana, J. Atomic Defects during Ordering Transitions in LiNi0.5Mn1.5O4 and Their Relationship with Electrochemical Properties. *J. Mater. Chem. A* **2016**, *4* (21), 8255–8262.

(93) Wang, Y.; Liu, H.; Bao, M.; Li, B.; Su, H.; Wen, Y.; Wang, F. Structural-Controlled Synthesis of Manganese Oxide Nanostructures and Their Electrochemical Properties. *J. Alloys Compd.* **2011**, *509* (33), 8306–8312.

(94) Chemelewski, K. R.; Shin, D. W.; Li, W.; Manthiram, A. Octahedral and Truncated High-Voltage Spinel Cathodes: The Role of Morphology and Surface Planes in Electrochemical Properties. *J. Mater. Chem. A* **2013**, *1* (10), 3347–3354.

(95) Fan, Y.; Wang, J.; Ye, X.; Zhang, J. Physical Properties and Electrochemical Performance of LiNi 0.5 Mn 1.5 O 4 Cathode Material Prepared by a Coprecipitation Method. *Mater. Chem. Phys.* **2007**, *103*, 19–23.

(96) Zhang, M.; Liu, Y.; Xia, Y.; Qiu, B.; Wang, J.; Liu, Z. Simplified Co-Precipitation Synthesis of Spinel LiNi0.5Mn1.5O4with Improved Physical and Electrochemical

Performance. *J. Alloys Compd.* **2014**, *598*, 73–78.

(97) Fang, H.; Wang, Z.; Li, X.; Guo, H.; Peng, W. Low Temperature Synthesis of LiNi0.5Mn1.5O4 Spinel. *Mater. Lett.* **2006**, *60* (9–10), 1273–1275.

(98) Xiang, Y.; Yin, Z.; Zhang, Y.; Li, X. Effects of Synthesis Conditions on the Structural and Electrochemical Properties of the Li-Rich Material Li[Li0.2Ni0.17Co0.16Mn0.47]O2 via the Solid-State Method. *Electrochim. Acta* **2013**, *91*, 214–218.

(99) Jiao, C.; Wang, L.; Zuo, Y.; Ni, P.; Liang, G. Solid-State Synthesis of Spherical Hierarchical LiNi0.5Mn1.5O4 through an Improved Calcination Method and Its Cyclic Performance for 5 V Lithium Ion Batteries. *Solid State Ionics* **2015**, *277*, 50–56.

(100) Raja, M. W.; Mahanty, S.; Basu, R. N. Multi-Faceted Highly Crystalline LiMn2O4 and LiNi0.5Mn1.5O4 Cathodes Synthesized by a Novel Carbon Exo-Templating Method. *Solid State Ionics* **2009**, *180* (23–25), 1261–1266.

(101) Kim, J. H.; Myung, S. T.; Sun, Y. K. Molten Salt Synthesis of LiNi0.5Mn1.5O4 Spinel for 5 V Class Cathode Material of Li-Ion Secondary Battery. *Electrochim. Acta* **2004**, *49* (2), 219–227.

(102) Wen, L.; Lu, Q.; Xu, G. Molten Salt Synthesis of Spherical LiNi0.5Mn1.5O4 Cathode Materials. *Electrochim. Acta* **2006**, *51* (21), 4388–4392.

(103) Hai, B.; Shukla, A. K.; Duncan, H.; Chen, G. The Effect of Particle Surface Facets on the Kinetic Properties of LiMn1.5Ni0.5O4 Cathode Materials. *J. Mater. Chem. A* **2013**, *1* (3), 759–769.

(104) Spence, S. L.; Xu, Z.; Sainio, S.; Nordlund, D.; Lin, F. Tuning the Morphology and Electronic Properties of Single-Crystal LiNi 0.5 Mn 1.5 O 4−δ : Exploring the Influence of LiCl–KCl Molten Salt Flux Composition and Synthesis Temperature. *Inorg. Chem.* **2020**, *59*, 10591–10603.

(105) Basin, A. S.; Kaplun, A. B.; Meshalkin, A. B.; Uvarov, N. F. The LiCl-KCl Binary System. *Russ. J. Inorg. Chem.* **2008**, *53* (9), 1509–1511.

(106) Lin, F.; Liu, Y.; Yu, X.; Cheng, L.; Singer, A.; Shpyrko, O. G.; Xin, H. L.; Tamura, N.; Tian, C.; Weng, T.-C.; Yang, X.-Q.; Meng, Y. S.; Nordlund, D.; Yang, W.; Doeff, M. M. Synchrotron X-Ray Analytical Techniques for Studying Materials Electrochemistry in Rechargeable Batteries. *Chem. Rev.* **2017**, *117* (21), 13123–13186.

(107) Hong, Y. S.; Huang, X.; Wei, C.; Wang, J.; Zhang, J. N.; Yan, H.; Chu, Y. S.; Pianetta, P.; Xiao, R.; Yu, X.; Liu, Y.; Li, H. Hierarchical Defect Engineering for LiCoO2 through Low-Solubility Trace Element Doping. *Chem* **2020**, *6* (10), 2759–2769.

Chapter 2. Influences of Tunable Molten Salt Synthesis Parameters on High-Voltage Cathode Particle Size, Uniformity, and Performance

Stephanie L. Spence[1], Rachel Perez[1], Anyang Hu[1], Feng Lin[1]*

[1]Department of Chemistry, Virginia Tech, Blacksburg, VA 24061, USA

2.1. Abstract

Synthetically controlling morphological heterogeneity at both the particle level and materials level is important in dictating single-crystal cathode materials performance. Herein, single-crystal $LiNi_{0.5}Mn_{1.5}O_4$ (LNMO) high-voltage cathode materials for Li-ion batteries were synthesized via a molten salt synthesis method using eutectic LiCl and KCl. Synthesis variables including synthesis time, transition metal precursor to salt ratio, crucible volume, batch size, and covering condition were systematically tuned and their influence on both individual particle morphology and overall size distribution were investigated revealing that the seemingly facile molten salt synthesis method may be more complicated than previously suggested. Crystal structure and electrochemical performance were investigated under each synthesis condition to correlate materials structure and property relationships. This study reveals that minor variations in the synthesis conditions, specifically, the amount of exposed surface area of precursors to oxygen in the synthesis atmosphere, can have a non-trivial influence on materials properties. Minimal oxygen flow produced impurity-free octahedral LNMO particles with sizes of up to 10 μm and a specific discharge capacity of 121.7 mAh/g.

2.2. Introduction

Li-ion batteries (LiBs) have proliferated as energy storage devices for electric vehicles, consumer electronics, and grid storage, and improving their performance and safety is of the utmost importance.[1] Structural and chemical heterogeneities are an important feature in dictating the lifetime and degradation of LiB cathode materials, and the effect has been studied across different length scales.[2] In the composite cathode comprised of active materials, conductive carbon, and polymer binder additives, local network heterogeneity can result in asynchronous

behavior early in cycling.[3] Upon prolonged cycling behavior becomes more synchronous and particle-to-particle variation has a more significant effect on chemomechanical damage. Morphological features including polycrystalline or single-crystalline microstructure, particle size, and particle shape are critical in influencing cathode material stability and performance.[4–6] Single-crystal particles can be very chemo-mechanically robust, but uniformity is desired to improve performance.[7–9] In single-crystal materials, homogeneous structure and grain size control can increase battery capacity, rate performance, and cycle life.

$LiNi_{0.5}Mn_{1.5}O_4$ (LNMO) is a promising high-voltage cathode material for LiBs. Two crystallographic structures of the spinel phase material exist including a Ni/Mn cation-ordered and cation-disordered structure, where the cation disordered material contains some electrochemically active Mn^{3+} which can increase overall electronic conductivity.[10] In addition, LNMO undergoes multiple cubic phase transitions upon (de)lithiation. The heterogeneous existence of three structural groups accompanied by internal domain boundaries and defects are considered to cause differences in charging and discharging behaviors in LNMO.[11–13] Intra- and inter- particle heterogeneities can increase severity upon cycling, and can initially be caused by heterogeneous conditions during synthesis.[14] A facile molten salt synthesis method has been used to synthesize well-defined single-crystal LNMO but resulted in particles with a large deviation in size and morphology uniformity.[15] Synthesis conditions which can include salt flux identity and composition, transition metal to salt ratio, synthesis time, and synthesis volume can influence nucleation and growth rates of particles to different degrees leading to differences in morphologies, particle sizes, and size distributions.[16,17] Although the molten salt is a highly tunable method, it remains a challenge to correlate multiple synthesis parameters to physical properties.

Herein, we systematically tune molten salt synthesis parameters including synthesis time, transition metal precursor to salt ratio, crucible size, batch size, and covering to the atmosphere during heating to develop LNMO materials with micron-sized octahedral morphology. We then evaluate physical properties including particle size, size uniformity, and structural purity and correlate them to electrochemical performance. We have found that particle size can be increased up to several microns by using a transition metal to molten salt ratio of 1 : 45 or 1 : 60 and synthesis time of 12 hours as this allows particles to have adequate room and time for growth in the molten medium after nucleation. Covering, crucible size, and batch size have a non-trivial influence the final product morphology as the surface area of material exposed to the atmosphere can affect the growth conditions of the particles and minimal oxygen flow can reduce impurity phase content and increase specific capacity. Determining the optimal parameters for the formation of large, stable LNMO particles with uniform size distribution and high specific capacity can aid in the stable cycling performance of this material in Li-ion batteries.

2.3. Results and Discussion

During the molten salt synthesis process, transition metal precursors and salts are dissolved in a minimal amount of deionized water and the slurry is heated in an alumina crucible. Micron-sized octahedral LNMO particles can be formed using a eutectic LiCl/KCl ratio at 650 °C.[15,16,18] To further explore the influence of molten salt synthesis parameters on the formation of octahedrons and their resulting properties, herein, we tune molten salt synthesis parameters including transition metal precursor to salt ratio (R, where a 1:30 ratio is represented as R = 30), synthesis time, and surface area through altering crucible size, covering condition, and batch size. **Table 1** lists the full synthesis parameters and identification for each sample.

Table 1. Summary of LNMO samples and molten salt synthesis parameter variables. Sample IDs indicate synthesis time in hours (e.g. 8h), R ratio (e.g. R30), crucible size [small (S), medium (M), or large (L)], batch size in grams (e.g. 0.5g), and covered (C) or uncovered (U) condition. Sample IDs are shortened (in bold) where appropriate.

Sample ID	R Ratio	Time, h	Crucible size	Covering	Batch size, g
8h_R30_S_0.5g_U*	30	8	Small	No	0.5
12h_R30_S_0.5g_U	30	12	Small	No	0.5
16h_R30_M_0.5g_U	30	16	Medium	No	0.5
8h_R60_M_0.5g_U*	60	8	Medium	No	0.5
12h_R60_M_0.5g_U^	60	12	Medium	No	0.5
16h_R60_M_0.5g_U	60	16	Medium	No	0.5
8h_**R45_S**_0.5g_U	45	8	Small	No	0.5
8h_**R60_S**_0.5g_U	60	8	Small	No	0.5
8h_**R30_M**_0.5g_U	30	8	Medium	No	0.5
8h_**R45_M**_0.5g_U	45	8	Medium	No	0.5
12h_R60_**S_0.5g_U**	60	12	Small	No	0.5
12h_R60_**S_0.5g_C**	60	12	Small	Yes	0.5
12h_R60_**M_0.5g_C**	60	12	Medium	Yes	0.5
12h_R60_**L_0.5g_U**	60	12	Large	No	0.5
12h_R60_**L_0.5g_C**	60	12	Large	Yes	0.5
12h_R60_**L_1.0g_U**	60	12	Large	No	1.0
12h_R60_**L_1.0g_C**	60	12	Large	Yes	1.0

2.3.1. Influence of Synthesis Time

The molten salt synthesis temperature affects both the morphology and the electrochemically active Mn^{3+} content of resulting LNMO powders, where 650 °C synthesis for 8 hours produces well-defined octahedral particles.[15] To maintain morphology but potentially increase the growth rate of octahedral LNMO particles, we investigated the effect of holding time

at 650 °C. **Figure 2-1** shows the SEM images of materials held for 8, 12, and 16 hours in transition metal to salt ratios of 1 : 30 or 1 : 60. In the R = 30 flux, 8-hour and 12-hour holds led to the formation of approximately 0.5 to 1.5 μm sized single crystal octahedral particles, while synthesis for 16 hours led to particle agglomeration, truncation, and wider size distribution. In R = 60 flux, 8 and 12 hour holds produced particles ranging from approximately 200 nm to 3 μm and 300 nm to > 5 μm, respectively. Agglomeration became more severe for particles synthesized for 16 hours in R = 60 flux. From the powder X-ray diffraction (XRD) patterns (**Figure 2-2**), sharp diffraction peaks indicate the crystallinity of the disordered cubic spinel phase. Impurity phase content increased as both synthesis time and flux were increased, indicated by peaks at around 20.8 and 21.7 °2θ corresponding to monoclinic Li_2MnO_3, and around 36.8 and 43.3 °2θ corresponding to rock-salt $Li_xNi_{1-x}O$. Excess Li reacting with oxygen from the air environment could favor the formation of Li_2MnO_3 and as a result, NiO species as a portion of Mn is already consumed.[16] Impurity formation is increased at longer synthesis holding times and in the larger salt flux containing a larger excess of Li. From varying synthesis times, 8 to 12 hours are found to be ideal to form single-crystal octahedral particles, while an R = 60 flux can produce larger, more robust particles.

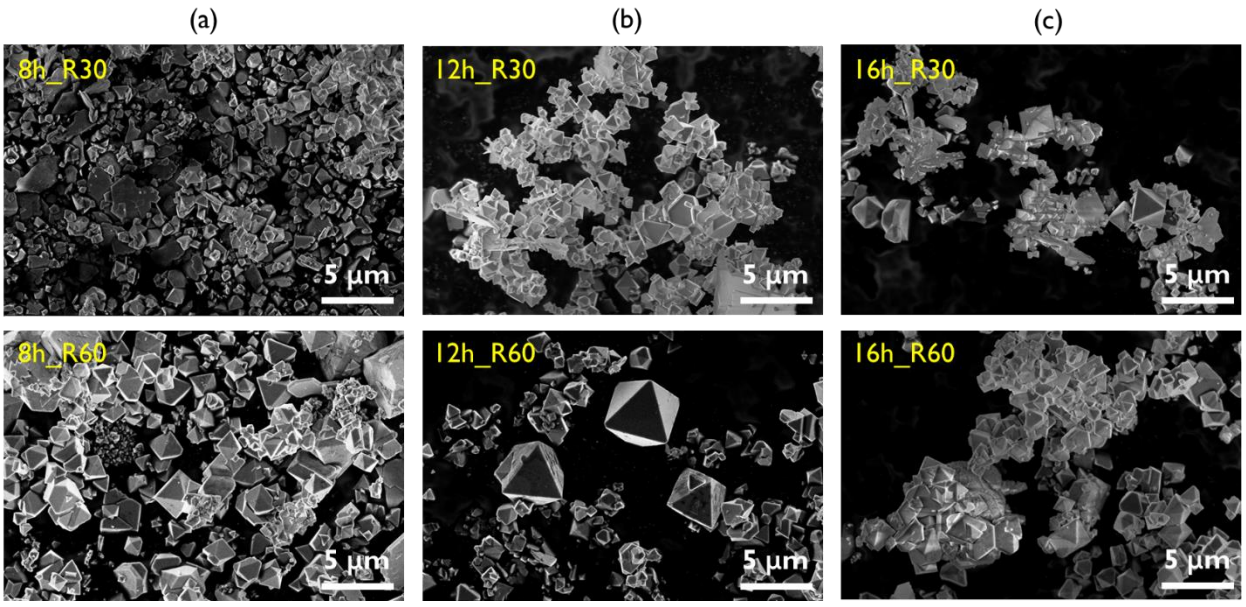

Figure 2-1. SEM images of LNMO powders synthesized at 650 °C for **(a)** 8, **(b)** 12, and **(c)** 16 hours with an R ratio of 30 or 60.

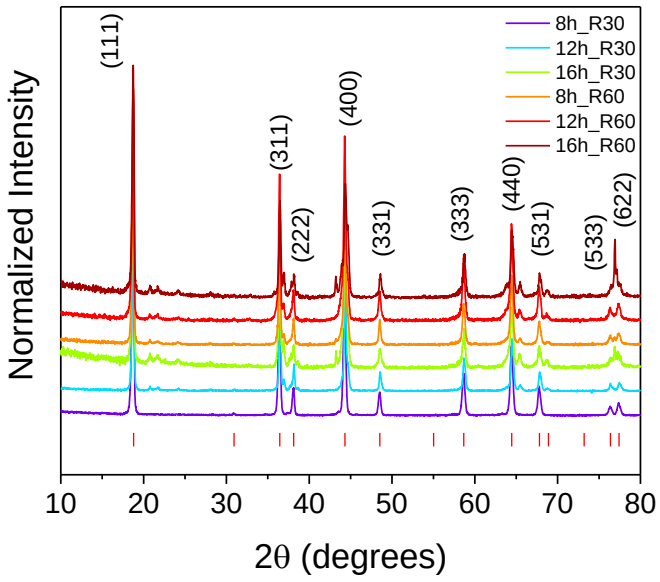

Figure 2-2. XRD patterns of LNMO powders synthesized at 650 °C for 8, 12, or 16 hours with an R ratio of 30 or 60. Tick lines represent disordered cubic spinel structure peak locations.

2.3.2. Influence of Molten Salt Ratio

We further investigate the effect of the molten salt ratio by tuning R. Synthesis in different sized crucibles also produced an effect on morphology and performance. Abundant molten salt content allows efficient diffusion of the raw materials and should prevent nanometer-sized particles from agglomerating during heating. From the SEM images in **Figure 2-3**, increasing the R ratio from 30 to 45 to 60 in the small crucible changed the maximum particle size from 3.5 to 6.5 to 6.3 μm, while also seemingly widening the size distribution. Synthesis in the medium crucible also produced nanometer-sized crystals and 5.8, 5.7, and 6.7 μm maximum-sized particles, respectively. From the XRD patterns shown in **Figure 2-4a**, impurity phases were present in samples R60_S, R45_M, and R60_M, due to the higher flux ratios, similar to what was observed in **Figure 2-2**. Sample R45_M is slightly shifted to higher angles indicating a contraction of the unit cell.

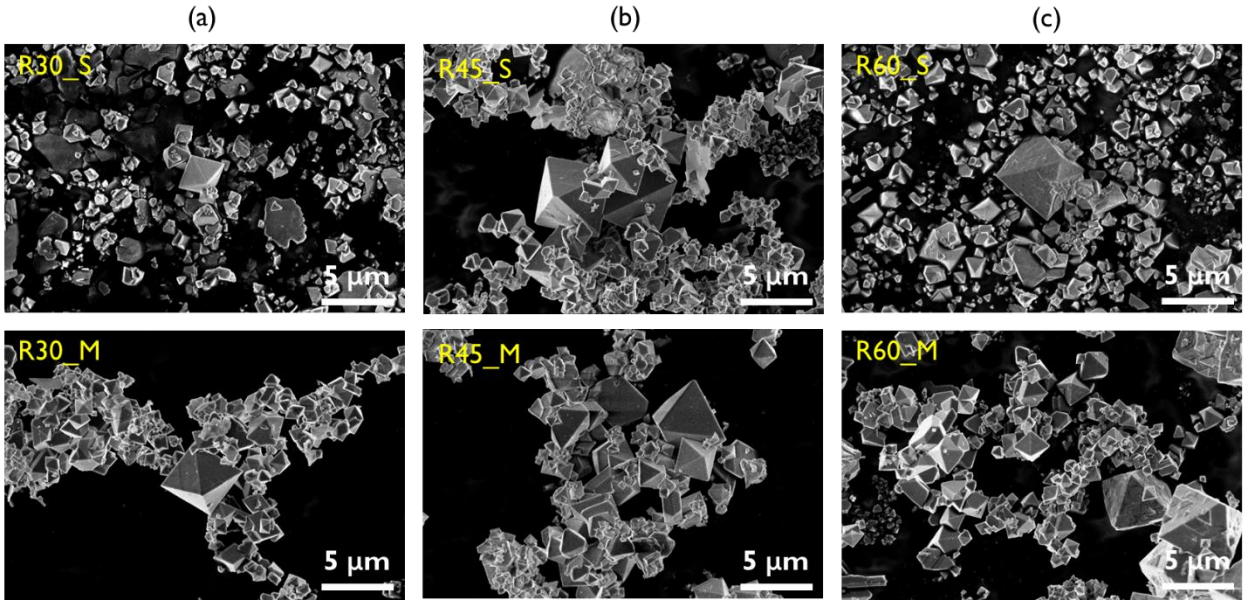

Figure 2-3. SEM images of LNMO powders synthesized at 650 °C for 8 hours with an R ratio of **(a)** 30, **(b)** 45, and **(c)** 60 in small or medium crucibles.

To test the electrochemical performance of samples, coin cells were prepared from each powder sample. The voltage profile and performance of LNMO material is influenced by the cation ordering and oxidation state of Mn.[19,20] The disordered phase is associated with the presence of reduced Mn^{3+} which is electrochemically active and leads to a secondary voltage plateau at ~4.0 V vs Li/Li^+ in addition to Ni redox at ~4.7 V vs Li/Li^+.[10] We can use the percentage of total capacity obtained between 3.8 and 4.25 V originating from the $Mn^{3+/4+}$ redox plateau to approximate the amount of electrochemically active Mn^{3+} present in each sample. **Figure 2-4b** shows the second discharge profiles for the samples prepared with various R ratios in small and medium crucibles. In the small crucible, increasing the R ratio gives discharge capacities of 88.7, 100.2, and 77.8 mAh/g, respectively. Materials synthesized in the medium crucibles give 91.1, 87.6, and 88.5 mAh/g upon increasing R. The highest performing samples also contain the highest percentages of capacity from the 4.0 V region (up to 9.2% for R45_S), indicating the beneficial effect of a moderate amount of Mn^{3+} on the electrochemical performance. From the cycling performance over 50 cycles at a rate of C/10 (**Figure 2-4c**), the Columbic efficiency is very poor for the lowest performing samples while capacity fading seems less severe for samples prepared in the medium crucible. Neither the capacities nor percent of 4.0 V plateau regions exhibit an apparent trend with R ratio or crucible size, indicating the complex factors associated with the molten salt synthesis and property relationships of LNMO.

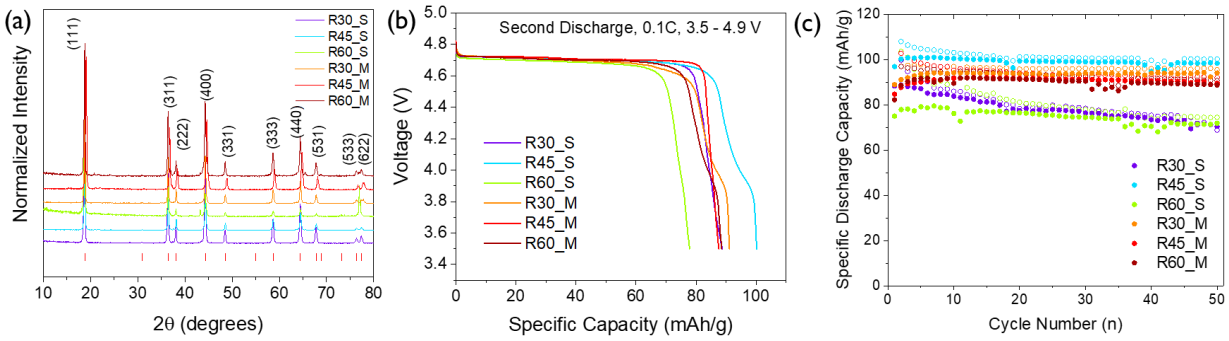

Figure 2-4. (a) XRD patterns, **(b)** discharge profiles, and **(c)** cycling performance of LNMO powders synthesized at 650 °C for 8 hours with an R ratio of 30, 45, or 60 in small or medium crucibles. Tick lines in XRD represent disordered spinel phase peak locations.

2.3.3. Influence of Exposed Surface Area

It is apparent that when keeping all other synthesis parameters the same, the size of the crucible has a non-trivial effect on LNMO performance; however, a trend is hard to reveal. We attribute the effect to the change in the percentage of the surface area of the sample slurry exposed to the atmosphere upon heating. Indeed, increasing the flux ratio increases the total amount of total salt present in the crucible and also affects the exposed surface area compared to the volume of the sample. To investigate this further, we prepared LNMO samples in small, medium, and large crucibles with 20, 30, or 50 mL volumes, respectively, while maintaining the salt ratio and a 0.5 g batch size. Based on the volume of starting material and dimensions of each crucible we calculate the ratio of surface area exposed to total volume (SA/V) to be 0.92, 1.14, and 2.15 for small, medium, and large crucibles, respectively. We performed an additional synthesis doubling the batch size to 1.0 g in the large crucible reducing the SA/V to 1.08, similar to that of the 0.5 g batch prepared in the medium crucible. In addition, we performed each synthesis with the crucible

uncovered and covered to the atmosphere, where covering reduces the SA/V to close to zero. A small opening was left to allow gases to escape during synthesis and to still provide oxygen flow. During covered synthesis, oxygen is limited allowing for Mn^{2+} precursors to oxidize fully to Mn^{4+} of the spinel phases while preventing the additional reaction of oxygen with excess Li and the formation of impurities.[16]

Figure 2-5 shows the SEM images of the resulting samples. Sample S_0.5g_U produced octahedrons up to 7.3 µm in size. With covering, particles up to 3.1 µm were observed. Particles under 100 nm were present in both samples indicating a wide size distribution. In the medium crucible, particles from hundreds of nm to 5.7 µm were present in the uncovered synthesis while covering produced a particle > 10 µm. Up to 5.8 µm and 7.1 µm particles were formed in the large crucible while uncovered and covered, respectively (**Figure 2-5c**); however, an agglomeration of nanometer-sized particles was present in the uncovered sample. Increasing the batch size, but lowering the SA/V led to the formation of particles similar to that of those in the previous synthesis, but > 5 µm particles were not observed. With covering, the particle size variation is wider compared to the uncovered state. In the medium and large crucibles, covering leads to larger particle growth, but a wider distribution. Overall, the morphological differences are minor but illustrate the difficulty of forming uniform, well-defined, single-crystal LNMO via the molten salt synthesis method. However, particle heterogeneity may directly influence the electrochemical performance.

XRD patterns of the powders prepared in small, medium, and large crucibles show that the impurity content increases from smaller to larger crucible sizes and SA/V ratios for the uncovered samples (**Figure 2-6a**). The samples that were covered during synthesis show minimal impurity phases. The voltage profiles for the second discharge (**Figure 2-6b)** show a trend of increasing

specific capacity with decreasing SA/V. The covered samples in the medium and large crucibles show higher capacities than their uncovered counterparts do; however, the sample synthesized in the smallest crucible shows a significant drop in capacity when covered. This may be due to inadequate diffusion of the limited oxygen over a smaller SA/V ratio so that pure phase LNMO could not be formed throughout the depth of the sample slurry. In fact, S_0.5_C is the only covered sample with visible impurity peaks in the XRD. The 4.0 V plateau capacity contribution increase in uncovered cases indicating Mn is more adequately oxidized during covered synthesis. From the cycling performance in **Figure 2-6c**, all samples show a brief period of activation, which is typical for LNMO material, and capacity retention of > 90%.[21] Sample M_0.5g_C gives the largest specific capacity of 121.7 mAh/g while also containing the largest octahedral particles, despite a wide size distribution, indicating an important relationship between performance and particle morphology. Synthesis conditions including exposed surface area influence both the particle level and materials level properties of LNMO, which have a complex and synergistic impact on electrochemical performance.

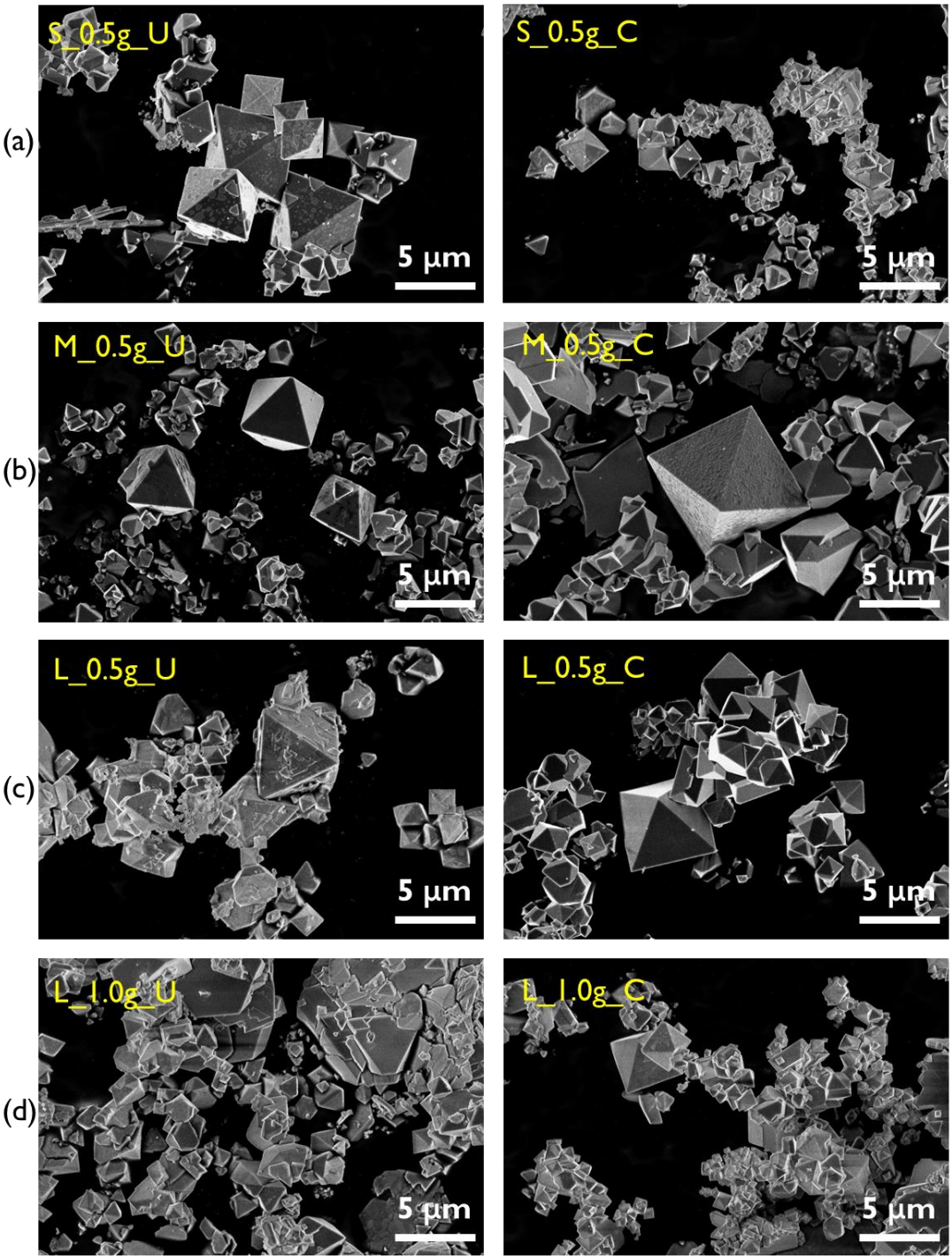

Figure 2-5. SEM images of LNMO powders synthesized at 650 °C for 8 hours with an R ratio of 60 in a **(a)** small, **(b)** medium, or **(c)** large crucible with a 0.5 g batch size or a **(d)** large crucible with a 1.0 g batch size. Crucibles were either uncovered or covered during synthesis.

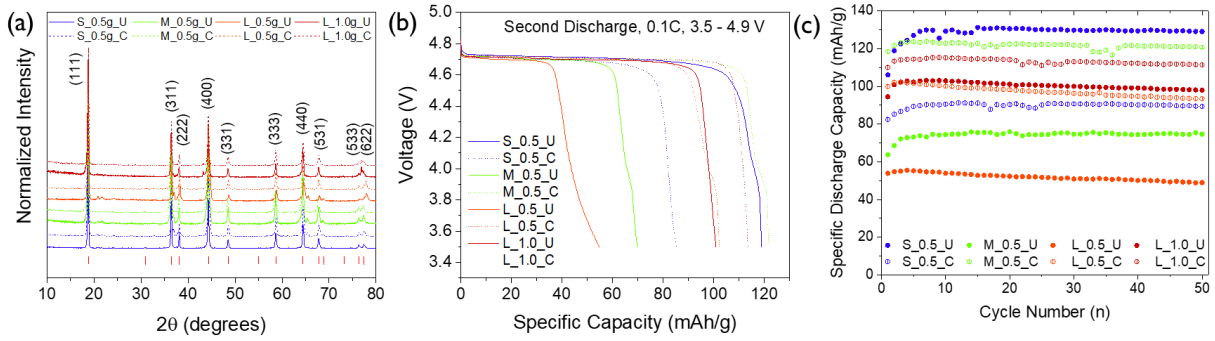

Figure 2-6. (a) XRD patterns, **(b)** discharge profiles, and **(c)** cycling performance of LNMO powders synthesized at 650 °C for 12 hours with an R ratio of 60 in small, medium, or large crucibles, 0.5 or 1.0 g batch size, and covered or uncovered. Tick lines in XRD represent disordered spinel phase peak locations.

2.4. Conclusions

In conclusion, we synthesized LNMO materials while systematically investigating the parameters for the molten salt synthesis including various synthesis times, molten salt ratios, crucible volumes, batch sizes, and covering conditions to influence exposed surface area. An 8-hour synthesis led to the formation of more uniform particle distributions, while 12 hours increased octahedral particle size, and 16 hours led to particle agglomeration and truncation. A trend in morphology and performance with changing R ratio was hard to discern; however, larger ratios allowed for particle growth concurrently with increased impurity formation. In changing the exposed surface area, specific capacity increased with lower SA/V ratios. Limiting oxygen content to the precursors by covering the crucibles during heating allowed for the formation of pure phase LNMO with high specific capacity. Although the molten salt synthesis method is thought to be facile, here we illustrate that small variations from batch to batch including specific crucible dimensions or batch size are non-trivial in dictating the final product properties. Changes in

individual particle morphologies as well as particle-to-particle variation indicate that heterogeneity at different length scales must be taken into account to understand the properties and performance of single-crystal cathode materials. Utilizing synthesis conditions to tune materials sizes and morphologies represents a method of synthetic tailoring to address degradation and dictate performance of electrode materials.

2.5. Experimental Section

2.5.1. Materials Synthesis

Materials were synthesized using stoichiometric amounts of $Ni(NO_3)_2 \cdot 6H_2O$ and $Mn(NO_3)_2 \cdot 4H_2O$, and a eutectic ratio of LiCl and KCl. The ratio of transition metal precursors to salts, defined as R, was varied to R = 30, 45, and 60, where R = 30 corresponds to 1:30 transition metal precursors to salt flux. The total amounts of starting material were calculated to yield 0.5 or 1.0 grams of LNMO. Transition metal precursors and salts were dissolved in a minimal amount of deionized water and ground with a mortar and pestle. The mixture was transferred to a 20, 30, or 50 mL alumina crucible (hereafter notated small, medium, or large), and either left uncovered or covered. Materials were heated in air in a box furnace at a ramp rate of 2 °C/min and held for 8, 12, or 16 hours at 650 °C. A 30-minute hold at 350 °C was performed to allow for complete formation of the spinel phase[22,23] and oxygen incorperation[24]. After heating, the powders were allowed to cool naturally and were thoroughly washed with deionized water and isopropyl alcohol to remove salt residue, and then dried in a vacuum oven at 100 °C overnight.

2.5.2. Electrochemical Measurements

Coin cells were prepared with 80 wt% active material, 10 wt% polyvinylidene fluoride (PVDF) binder, and 10 wt% carbon black dissolved in N-methylpyrrolidone (NMP) solvent. Electrodes were cast using a doctor-blade method, cut into disks, and dried at 120 °C overnight, before being transferred to an Ar-filled glovebox. CR2032-type coin cells cans were used, with Li-foil as the anode, Celgard 2325 as the separators, and $LiPF_6$ (1 M) in ethylene carbonate (EC): dimethyl carbonate (DMC) (3:7 v/v) as the electrolyte. Cells were cycled from 3.5 to 4.9 V vs. Li/Li^+ at 0.1 C rate (1C = 147 mAh/g).

2.5.3. Materials Characterization

Scanning electron microscopy (SEM) images were collected using a LEO FESEM at an acceleration voltage of 5.0 kV. Powder X-ray diffraction (XRD) patterns were acquired on a benchtop Rigaku Miniflex II (λ Cu Kα = 1.5406 Å) from 10 to 80° 2θ with a step size of 0.02° 2θ and 1.0 s count time.

2.6. Acknowledgments

The work was supported by the National Science Foundation under Grant No. DMR-1832613.

2.7. References

(1) Armand, M.; Tarascon, J. M. Building Better Batteries. *Nature* **2008**, *451* (7179), 652–657.

(2) Yang, Y.; Xu, R.; Zhang, K.; Lee, S.; Mu, L.; Liu, P.; Waters, C. K.; Spence, S.; Xu, Z.; Wei, C.; Kautz, D. J.; Yuan, Q.; Dong, Y.; Yu, Y.; Xiao, X.; Lee, H.; Pianetta, P.; Cloetens, P.; Lee, J.; Zhao, K.; Lin, F.; Liu, Y. Quantification of Heterogeneous Degradation in Li-Ion Batteries. *Adv. Energy Mater.* **2019**, *9* (25), 1900674.

(3) Li, J.; Sharma, N.; Jiang, Z.; Yang, Y.; Monaco, F.; Xu, Z.; Hou, D.; Ratner, D.; Pianetta, P.; Cloetens, P.; Lin, F.; Zhao, K.; Liu, Y. Dynamics of Particle Network in Composite Battery Cathodes. *Science (80-.).* **2022**, *376* (6592), 517–521.

(4) Chemelewski, K. R.; Shin, D. W.; Li, W.; Manthiram, A. Octahedral and Truncated High-Voltage Spinel Cathodes: The Role of Morphology and Surface Planes in Electrochemical Properties. *J. Mater. Chem. A* **2013**, *1* (10), 3347–3354.

(5) Zhu, J.; Chen, G. Single-Crystal Based Studies for Correlating the Properties and High-Voltage Performance of Li[NixMnyCo1-x-y]O2 Cathodes. *J. Mater. Chem. A* **2019**, *7* (10), 5463–5474.

(6) Qin, X.; Gong, J.; Guo, J.; Zong, B.; Zhou, M.; Wang, L.; Liang, G. Synthesis and Performance of LiNi 0.5 Mn 1.5 O 4 Cathode Materials with Different Particle Morphologies and Sizes for Lithium-Ion Battery. *J. Alloys Compd.* **2019**, 240–249.

(7) Fan, X.; Hu, G.; Zhang, B.; Ou, X.; Zhang, J.; Zhao, W.; Jia, H.; Zou, L.; Li, P.; Yang, Y. Crack-Free Single-Crystalline Ni-Rich Layered NCM Cathode Enable Superior Cycling Performance of Lithium-Ion Batteries. *Nano Energy* **2020**, *70*, 104450.

(8) Qian, G.; Zhang, Y.; Li, L.; Zhang, R.; Xu, J.; Cheng, Z.; Xie, S.; Wang, H.; Rao, Q.; He, Y.; Shen, Y.; Chen, L.; Tang, M.; Ma, Z. F. Single-Crystal Nickel-Rich Layered-Oxide Battery Cathode Materials: Synthesis, Electrochemistry, and Intra-Granular Fracture. *Energy Storage Mater.* **2020**, *27*, 140–149.

(9) Liu, X.; Zheng, B.; Zhao, J.; Zhao, W.; Liang, Z.; Su, Y.; Xie, C.; Zhou, K.; Xiang, Y.; Zhu, J.; Wang, H.; Zhong, G.; Gong, Z.; Huang, J.; Yang, Y. Electrochemo-Mechanical Effects on Structural Integrity of Ni-Rich Cathodes with Different Microstructures in All Solid-State Batteries. *Adv. Energy Mater.* **2021**, *11* (8), 2003583.

(10) Kim, J. H.; Myung, S. T.; Yoon, C. S.; Kang, S. G.; Sun, Y. K. Comparative Study of LiNi0.5Mn1.5O 4-δ and LiNi0.5Mn1.5O4 Cathodes Having Two Crystallographic Structures: Fd3m and P4332. *Chem. Mater.* **2004**, *16* (5), 906–914.

(11) Uematsu, H.; Ishiguro, N.; Abe, M.; Takazawa, S.; Kang, J.; Hosono, E.; Nguyen, N. D.; Dam, H. C.; Okubo, M.; Takahashi, Y. Visualization of Structural Heterogeneities in Particles of Lithium Nickel Manganese Oxide Cathode Materials by Ptychographic X-Ray Absorption Fine Structure. *J. Phys. Chem. Lett.* **2021**, *12* (24), 5781–5788.

(12) Spence, S. L.; Hu, A.; Jiang, M.; Xu, Z.; Yang, Z.; Rahman, M. M.; Li, L.; Chu, Y. S.; Xiao, X.; Huang, X.; Lin, F. Mapping Lattice Distortions in LiNi 0.5 Mn 1.5 O 4 Cathode Materials. *ACS Energy Lett.* **2022**, 690–695.

(13) Kuppan, S.; Xu, Y.; Liu, Y.; Chen, G. Phase Transformation Mechanism in Lithium

Manganese Nickel Oxide Revealed by Single-Crystal Hard X-Ray Microscopy. *Nat. Commun.* **2017**, *8*, 14309.

(14) Finegan, D. P.; Vamvakeros, A.; Tan, C.; Heenan, T. M. M.; Daemi, S. R.; Seitzman, N.; Di Michiel, M.; Jacques, S.; Beale, A. M.; Brett, D. J. L.; Shearing, P. R.; Smith, K. Spatial Quantification of Dynamic Inter and Intra Particle Crystallographic Heterogeneities within Lithium Ion Electrodes. *Nat. Commun.* **2020**, *11* (1), 631.

(15) Spence, S. L.; Xu, Z.; Sainio, S.; Nordlund, D.; Lin, F. Tuning the Morphology and Electronic Properties of Single-Crystal LiNi 0.5 Mn 1.5 O 4−δ : Exploring the Influence of LiCl–KCl Molten Salt Flux Composition and Synthesis Temperature. *Inorg. Chem.* **2020**, *59*, 10591–10603.

(16) Kim, J. H.; Myung, S. T.; Sun, Y. K. Molten Salt Synthesis of LiNi0.5Mn1.5O4 Spinel for 5 V Class Cathode Material of Li-Ion Secondary Battery. *Electrochim. Acta* **2004**, *49* (2), 219–227.

(17) Wang, W.-N.; Meng, D.; Qian, G.; Xie, S.; Shen, Y.; Chen, L.; Li, X.; Rao, Q.; Che, H.; Liu, J.; He, Y.-S.; Ma, Z.-F.; Li, L. Controlling Particle Size and Phase Purity of "Single-Crystal" LiNi $_{0.5}$ Mn $_{1.5}$ O $_{4}$ in Molten-Salt-Assisted Synthesis. *J. Phys. Chem. C* **2020**, acs.jpcc.0c09313.

(18) Hai, B.; Shukla, A. K.; Duncan, H.; Chen, G. The Effect of Particle Surface Facets on the Kinetic Properties of LiMn1.5Ni0.5O4 Cathode Materials. *J. Mater. Chem. A* **2013**, *1* (3), 759–769.

(19) Duncan, H.; Hai, B.; Leskes, M.; Grey, C. P.; Chen, G. Relationships between Mn3+ Content, Structural Ordering, Phase Transformation, and Kinetic Properties in LiNixMn2-XO4 Cathode Materials. *Chem. Mater.* **2014**, *26* (18), 5374–5382.

(20) Moorhead-Rosenberg, Z.; Huq, A.; Goodenough, J. B.; Manthiram, A. Electronic and Electrochemical Properties of Li1-XMn1.5Ni0.5O4 Spinel Cathodes As a Function of Lithium Content and Cation Ordering. *Chem. Mater.* **2015**, *27* (20), 6934–6945.

(21) Zhou, J.; Hong, D.; Wang, J.; Hu, Y.; Xie, X.; Fang, H. Electronic Structure Variation of the Surface and Bulk of a LiNi 0.5Mn1.5O4 Cathode as a Function of State of Charge: X-Ray Absorption Spectroscopic Study. *Phys. Chem. Chem. Phys.* **2014**, *16* (27), 13838–13842.

(22) Whittingham, M. S. Lithium Batteries and Cathode Materials. *Chem. Rev.* **2004**, *104* (10), 4271–4301.

(23) Huang, X.; Chen, K.; Liu, Y. Structural Evolutions of LiNi0.5Mn1.5O4 Nanorods Synthesized by Different Lithium Sources and Effects on Electrochemical Performances. *Ionics (Kiel).* **2019**, 1–10.

(24) Liu, H.; Zhang, X.; He, X.; Senyshyn, A.; Wilken, A.; Zhou, D.; Fromm, O.; Niehoff, P.; Yan, B.; Li, J.; Muehlbauer, M.; Wang, J.; Schumacher, G.; Paillard, E.; Winter, M.; Li, J. Truncated Octahedral High-Voltage Spinel LiNi0.5Mn1.5O4 Cathode Materials for Lithium Ion Batteries: Positive Influences of Ni/Mn Disordering and Oxygen Vacancies. *J. Electrochem. Soc.* **2018**, *165* (9), A1886–A1896.

Chapter 3. Mapping Lattice Distortions in $LiNi_{0.5}Mn_{1.5}O_4$ Cathode Materials

Stephanie L. Spence[1], Anyang Hu[1], Meng Jiang[1], Zhengrui Xu[1], Zhijie Yang[1], Muhammad Mominur Rahman[1], Luxi Li[2], Yong S. Chu[3], Xianghui Xiao[3], Xiaojing Huang[3], Feng Lin[1*]*

[1]Department of Chemistry, Virginia Tech, Blacksburg, VA 24061, USA

[2]Advanced Photon Source, Argonne National Laboratory, Lemont, IL 60439, USA

[3]National Synchrotron Light Source II, Brookhaven National Laboratory, Upton, NY 11973, USA

This chapter has been published in *ACS Energy Letters*, **DOI:** 10.1021/acsenergylett.1c02759, and reprinted with permission from the American Chemical Society: Spence, S. L.; Hu, A.; Jiang, M.; Xu, Z.; Yang, Z.; Rahman, M.M.; Li, L.; Chu, Y.S.; Xiao, X.; Huang, X.; Lin, F. Mapping Lattice Distortions in $LiNi_{0.5}Mn_{1.5}O_4$ Cathode Materials. *ACS Energy Lett.* **2022**, *7*, 690-695.

3.1. Abstract

Spinel $LiNi_{0.5}Mn_{1.5}O_4$ (LNMO) can adopt two crystallographic structures: an ordered $P4_332$ structure and a disordered $Fd\bar{3}m$ structure. The disordered phase is associated with the reduction of a small amount of Mn^{4+} to Mn^{3+}. LNMO single-crystals likely contain local regions of both ordered and disordered regions, which ensemble-averaged characterizations fail to distinguish. Herein, we employ high-spatial-resolution synchrotron X-ray nanodiffraction techniques to identify lattice distortions and structural defects in LNMO samples with octahedral and plate-like morphologies containing ~6% and ~22% of Mn^{3+}, respectively. Differences in properties between the two particles give rise to different distributions of lattice variations, which may indicate differences in phase distributions. Bragg coherent diffraction is also used to observe phase heterogeneities in single grains. Lattice distortions and structural defects could shut down or open up local diffusion pathways for lithium ions, making lithium ion diffusion more complicated and potentially more tortuous than that in a perfect LNMO lattice.

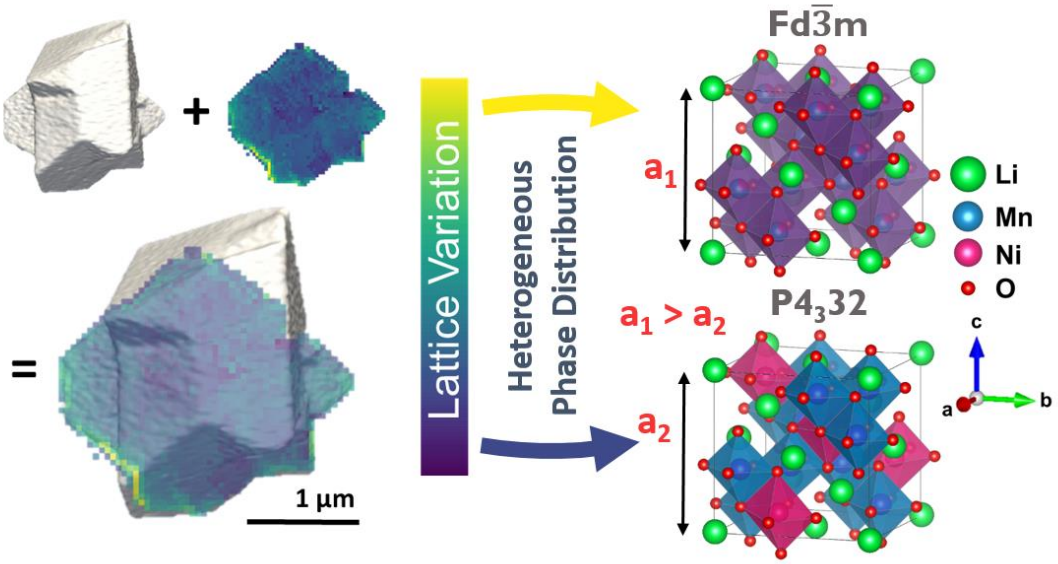

Figure 3-1. Table of Contents Figure.

3.2. Introduction

Despite the prevalence of lithium-ion batteries, continued improvements in electrochemical performance, safety, and lifetime are required to expand applications to larger scales, including electric vehicles and grid energy storage.[1] Spinel $LiNi_{0.5}Mn_{1.5}O_4$ (LNMO) is a promising high-voltage cathode material for lithium-ion batteries due to its high energy and high power. LNMO has a working potential of 4.7 – 4.9 V vs Li/Li^+, a theoretical capacity of 148 mAh/g, and a theoretical energy density of 650 Wh/kg at the materials level.[2–4] Three-dimensional lithium-ion pathways present in the spinel framework allow for facile ion transport and can potentially enable high rate performance.[5]

LNMO can adopt two crystallographic structures: an ordered primitive simple cubic with the $P4_332$ space group where Mn and Ni ions occupy 12b and 4a octahedral sites, respectively, and a disordered face-centered cubic with the $Fd\bar{3}m$ space group where Mn and Ni ions are randomly arranged on the 16d octahedral sites.[6] The formation of the disordered spinel phase requires higher synthesis temperatures than the ordered phase and is often associated with the loss of oxygen from the material lattice, as well as the reduction of a small amount of Mn^{4+} to Mn^{3+} for charge compensation.[6–8] Rock-salt $Li_xNi_{1-x}O$-type impurity formation, Jahn-Teller distortion, and transition metal dissolution suggest the presence of Mn^{3+} is disadvantageous to the application of LNMO.[9] However, a small amount of Mn^{3+} has been reported to be beneficial to performance.[10,11] An additional voltage plateau is observed in the charge/discharge curve of disordered LNMO at ~4.0 V due to the Mn^{3+}/Mn^{4+} redox, whereas Ni is the only redox-active transition metal in the fully ordered material.[6]

The relationship between structural disordering and Mn^{3+} content is not straightforward, therefore much effort in LNMO research has attempted to gain further understanding between the

two.[10,12] Thus far, a quantitative relationship is still not available. Efforts have been undertaken to control the global structural ordering of LNMO and correlate properties to electrochemical performance.[10,12–16] Careful synthesis can be used to control the formation of LNMO with either ordered or disordered structures or to minimize impurity phases. Practically, it is difficult to obtain pure disordered or ordered phase LNMO. In reality, varying degrees of cation ordering are likely present throughout local regions of individual particles in the synthesized materials.[17,18] Factors such as particle size and facet orientation may influence how cation ordered regimes distribute in single-particle samples. The presence of phase and chemical heterogeneities can exacerbate the degradation of Li-ion cathode materials upon cycling, therefore understanding such heterogeneities is vital for improving stability and performance.[19–21]

We hypothesize that the distribution of Mn^{3+} in disordered LNMO materials may be heterogeneous and that the extent of structural ordering varies between samples, depending on the synthesis conditions. The larger ionic radius of Mn^{3+} compared to Mn^{4+} can increase lattice spacing and internal strain within particles.[12] Changes in lattice spacing have been used to identify phase heterogeneity in $LiMn_2O_4$ during lithiation.[22] We, therefore, propose significant phase heterogeneity exists within the particles of LMNO prepared under different synthesis conditions and containing different quantities of Mn^{3+}.

Herein, we investigate structural defects and lattice distortion at the individual particle scale for octahedral and plate-like LNMO samples using high-spatial-resolution nanodiffraction mapping techniques to demonstrate that lattice distortion can provide significant insights into understanding phase heterogeneity in single-crystal LNMO. Combining techniques such as powder X-ray diffraction, X-ray absorption near-edge structure (XANES) analysis, Bragg Coherent X-ray Diffraction, and nanodiffraction, we observe differences in electronic states and

structural heterogeneities between two LNMO samples. Continued exploration of the structural characteristics of LNMO samples of various morphologies and Mn oxidation states can provide valuable insights into the relationship between several materials' properties, as well as the influence on the resultant electrochemical performance.

3.3. Results and Discussion

The octahedral LNMO sample was prepared at 650 °C using eutectic LiCl:KCl as a molten salt flux, while the plate sample was prepared at 750 °C in pure LiCl flux (see **Supporting Information** for experimental details).[23,24] Samples were thoroughly characterized through ensemble-averaged techniques, which revealed that a mixture of ordered and disordered spinel phases were present in both samples (see **Supporting Information**; **Figure S3-1**, **Figure S3-2**, and **Figure S3-3** for detailed discussion). The Mn^{3+} content was estimated for each sample from the electrochemical discharge profiles and calculated to be 5.7% and 22.0% for the octahedral and plate samples, respectively. Ensemble-averaged characterization techniques cannot distinguish local structural variations and, therefore, cannot provide a full picture of the materials' properties; high-spatial resolution diffraction is necessary to identify the distribution of the different phase regions within the particles.

3.3.1. Investigating Structure through Bragg Coherent X-ray Diffraction

Bragg Coherent X-ray Diffraction relies on coherent X-ray interference and can be used to study defects and strain in single-crystal materials.[25] Bragg coherent diffraction imaging has been used to study dislocation evolution in LNMO under operating conditions.[26] Bragg Coherent X-ray Diffraction is used to measure the 2D diffraction patterns of the pristine LNMO material. Particles

with two-phase coexistence are observed as in **Figure 3-1**. The two bright Bragg peaks appear at different diffraction angles indicating that there are two phases. The fringes about the Bragg center show the sharp surface structure in these local domains (or primary particles). The interference between the two Bragg spots indicates that the diffraction from two phases comes from the same particle. This behavior was also observed previously by Singer et al. during the two-phase transformation of LNMO spinel material during the charging process.[27] This observation illustrates that large structural heterogeneities exist within individual particles of LNMO. Analysis of this Bragg diffraction pattern suggests the complexity of the LNMO system. To determine the origin of such complexity, we next utilize nanodiffraction techniques.

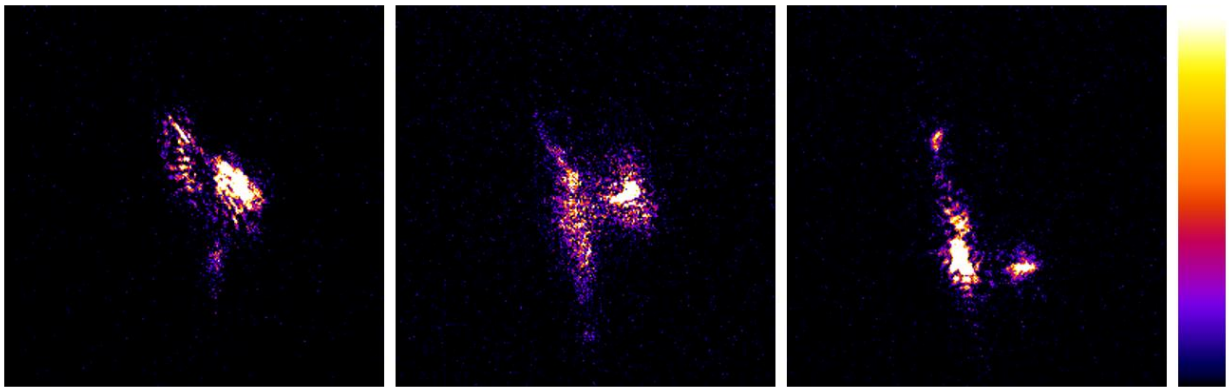

Figure 3-1. Bragg coherent diffraction patterns of octahedral LNMO crystals at the (111) Bragg position illustrating the coexistence of two phases. The color bar represents the diffraction intensity (white: highest intensity; black: lowest intensity).

3.3.2. Investigating Lattice Distortion Heterogeneity through Nanodiffraction

Both Mn^{3+} and cation disorder have been found to increase with increased synthesis temperatures above 700 °C.[24,28] The presence of both Mn^{4+} and Mn^{3+} unevenly distributed can lead

to strain and lattice parameter distortion within particles due to the differences in ionic radii of Mn, where more Mn^{3+} will lead to increased lattice spacing. Operando X-ray diffraction computed tomography (XRD-CT) has been used to spatially quantify inter- and intra-particle crystallographic heterogeneities in $Li_xMn_2O_4$ through tracking lattice parameter variation.[22] Through high-spatial-resolution nanodiffraction, we can observe the heterogeneity and distribution of lattice distortions in individual LNMO particles.

For the octahedral sample, the shape of the target particle for nanodiffraction was reconstructed by three-dimensional X-ray fluorescence tomography (**Figure S3-4a**; **Movie S3-1**). While our material is primarily single-crystal, the target particle selected contains multiple inter-grown crystals. The unique features of the selected particle can provide additional insight into the structural parameters near the domain boundaries within the particles. X-ray fluorescence mapping shows the elemental distribution of Ni and Mn in the particle, which are relatively homogenous (**Figure S3-4b**: **Movie S3-2**).

The nano-diffraction technique with a scanning hard X-ray beam was used to examine lattice defects in the LNMO samples. A schematic of the experimental setup of the hard X-ray nanoprobe (HXN) is illustrated in **Figure 3-2a**. In the setup, the sample was illuminated with X-rays focused to a ~30 nm spot size, the crystal orientation was adjusted to excite a Bragg diffraction, and a pixel-array detector was oriented to record the diffracted pattern from each scan position allowing for spatially resolved diffraction measurements.[29] The sample is rocked over a two-degree range in the vicinity of the selected Bragg peak while a 2D raster scan with 50 nm step size is conducted at each rocking angle resulting in the mapping shown in **Figure 3-2b** for the octahedral sample. The final image resolution is a convolution between the beam profile and the image pixel size (50 x 50 nm^2). Rocking curves at each Bragg position are shown in **Movie S3-3-**

S3-8. Scanning probe measurements were conducted in the on-the-fly scan mode to mitigate unnecessary radiation to the sample. For each peak, lattice distortions can be extracted by tracking the location of the Bragg diffraction peak over the rocking angular range at each scanned position.[29] The rocking-curve nano-diffraction measurement collects the 3D Bragg diffraction pattern at each scanned point. The position of the 3D diffraction pattern can be decomposed into three orthogonal directions, which include two components on the plane defined by the corresponding Debye-Scherrer ring (perpendicular and tangential to the ring direction) and one component perpendicular to that plane. As shown in **Figure 3-2c**, these three components represent the d-spacing, lattice bending in the z-axis, and lattice twisting in the y-axis, respectively.

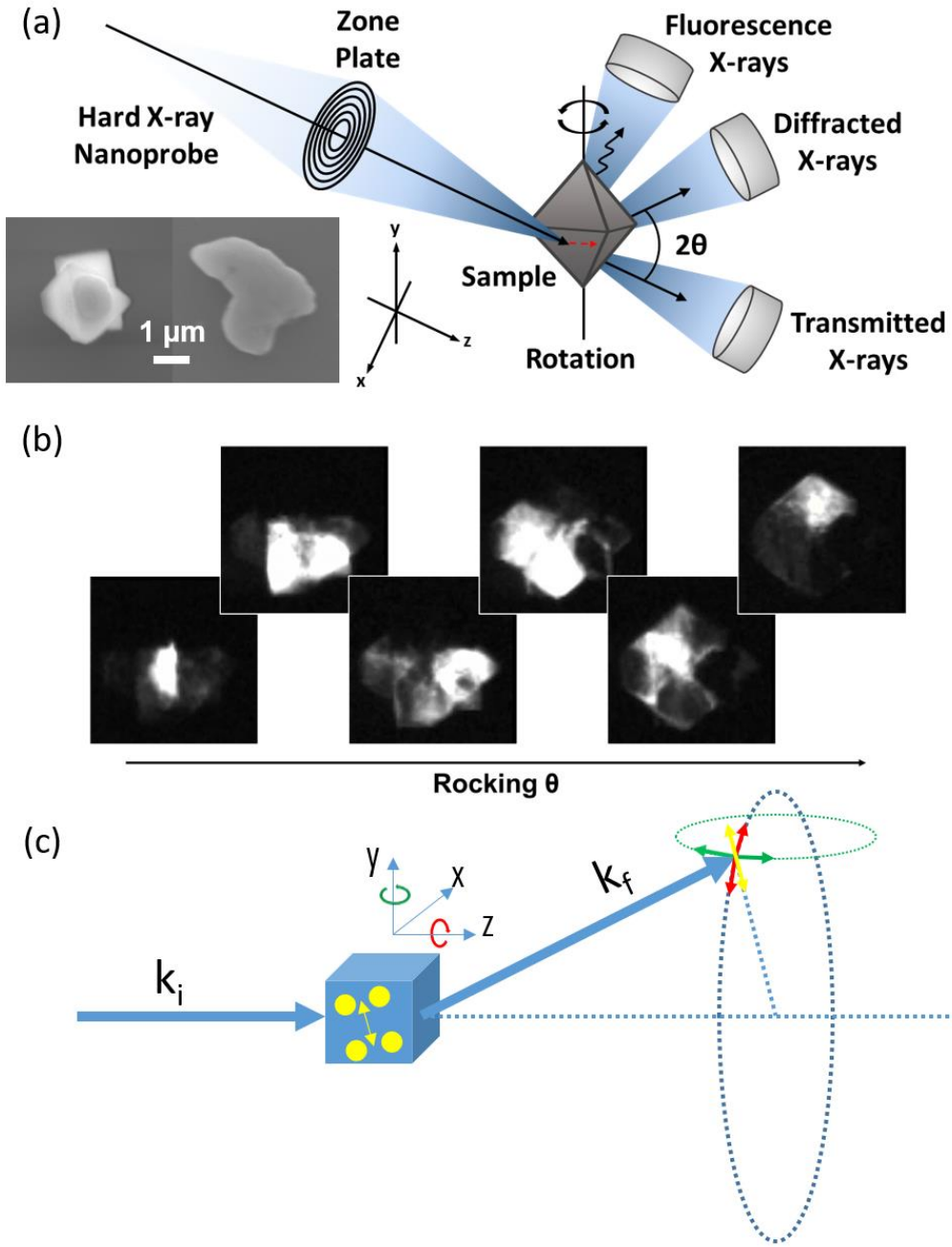

Figure 3-2. (a) Schematic illustration of hard X-ray nanoprobe experimental setup. Insert: SEM images of octahedral and plate target particles for HXN measurements. **(b)** 2D raster mapping of the octahedral sample particle as the particle is rocked over θ. The pixel size for the diffraction images is 50 x 50 nm^2. **(c)** Diffraction geometry and lattice distortions of d-spacing, lattice bending in the z-axis, and lattice twisting in the y-axis extracted from data.

The increase in lattice variation for Δd/d in the measured peaks can be attributed to changing d-spacing in the spinel phases and/or internal strain, while changes in bending y-axis and twisting z-axis arise from out-of-plane distortions as the crystals are not completely flat. The results of the nanodiffraction mapping for the octahedral sample at (311), (331), and (333) Bragg locations are shown in **Figure 3-3**. Visually, there are obvious heterogeneities in each map, which show the relative distribution of the total distortions present for each measurement. The change in d-spacing is significant near the particle surfaces for the (311) and (333) peaks (**Figure S3-5**). An increase in disorder near the particle surfaces can be rationalized by the surface oxygen loss and/or Ni-rich impurity formation which occurs primarily on the surface and can accompany the reduction of Mn.[30] At each measured peak, both bending y-axis and twisting z-axis maps show abrupt changes at a boundary within the particle, suggesting different domains with different crystal orientations or rotations. The radial-like change in distortion intensity indicates the likely presence of a screw dislocation (see arrows in **Figure 3-3**). We observe components of the dislocation in both the y and z directions, with a larger contribution from the z-axis. From the strain map, we see these domains have similar d-spacing but are rotated.

The plate sample was measured at the (111), (311), and (222) Bragg positions, and the nanodiffraction mapping is summarized in **Figure 3-4**. The differences in the shape of the maps for the (111) and (311) compared to the (222) positions of the plate sample indicate there are two distinct grains or crystal domains within the particle with slightly different orientations. Overlaying the images results in the full shape of the target particle (**Figure S3-6**). Similar to the octahedral sample, a large-scale heterogeneity for rotation was observed in the y- and z-axes. All distortions are more prominent towards the boundary of the two large particle grains (**Figure S3-6** and **S3-7**).

The plate sample also contains several, small local domains with abrupt changes in the distortion intensities.

For each map, a pixel intensity analysis was performed resulting in histograms illustrating the relative distribution of the distortions (**Figure 3-5**). For each plot, a larger variation (or standard deviation) corresponds to a larger overall distortion. The distortion variation appears facet dependent. **Figure S3-8** shows schematics of the atomic arrangements at each crystal plane. Comparing the measurements at the (311) plane for the octahedral and plate samples, the plate samples show a slightly wider distribution in the variations with a larger skewing towards increased d-spacing, bending y-axis, and twisting z-axis values. The (333) plane of the octahedral and the (111) plane of the plate show similar distribution behavior to their corresponding (311) planes. Finally, the (331) plane of the octahedral sample and (222) plane of the plate sample show the smallest relative distortions.

The average d-spacings for the (311) plane of the octahedral and the plate samples were calculated as 0.2469 nm and 0.2548 nm, respectively. This is consistent with the expectation that the plate sample containing more overall Mn^{3+} (with increased ionic radius) would contain larger d-spacing. We speculate that the areas with increased relative d-spacing in the distortion maps correlate with regions that contain more Mn^{3+}. There is a slightly wider degree of y-bending and z-twisting variation for the plate sample, which may be due to more Mn^{3+} or the presence of multiple domains with slightly different orientations. Ultimately, we observe inherent distortions in the two samples prepared under different synthesis conditions with octahedral and plate-like morphologies. The significant lattice distortion heterogeneity in both samples is indicative of phase heterogeneity which may be induced by an uneven distribution of Mn^{3+}.

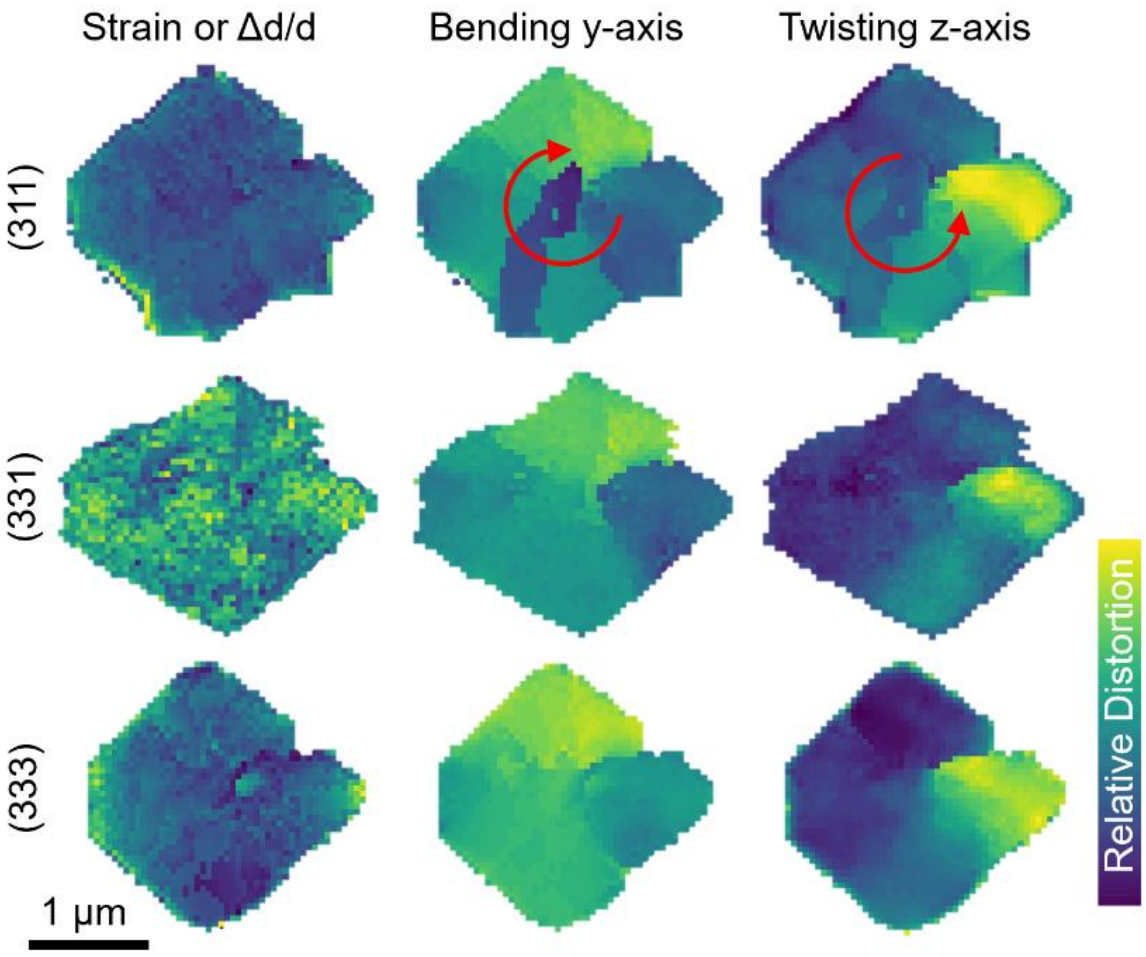

Figure 3-3. Lattice distortion mapping of octahedral LNMO at (311), (331), and (333) Bragg positions. Red arrows indicate direction of radial increase in distortion intensity.

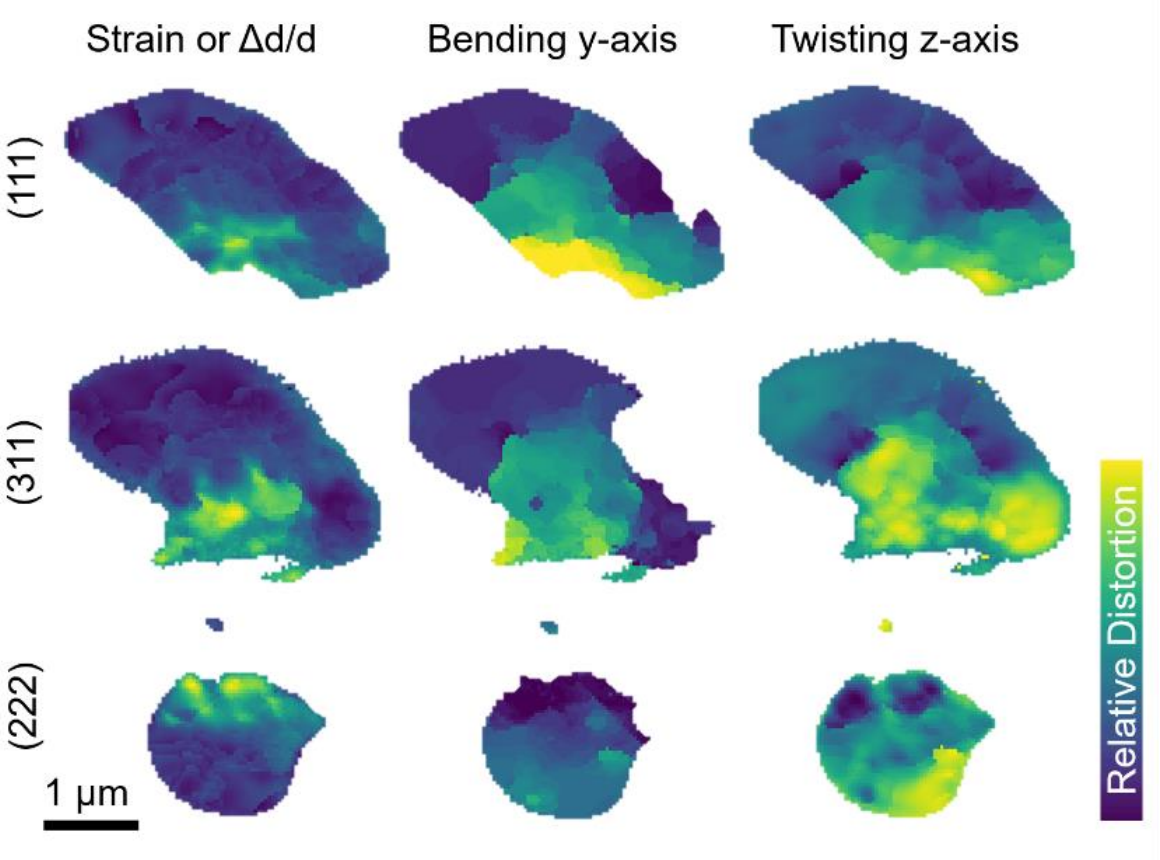

Figure 3-4. Lattice distortion mapping of plate LNMO at (111), (311), and (222) Bragg positions.

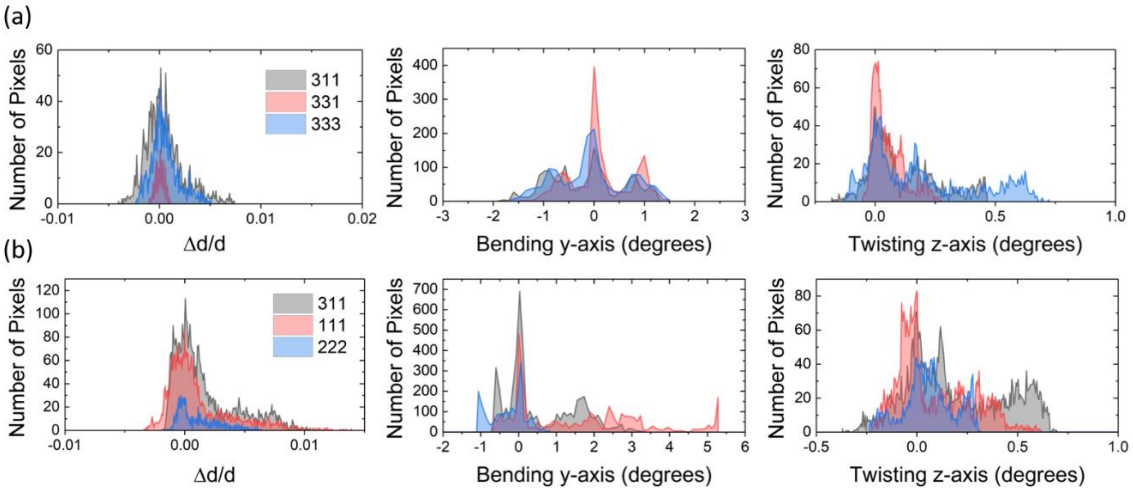

Figure 3-5. Lattice variation histograms based on pixel intensity analysis for the **(a)** octahedral and **(b)** plate particle samples.

3.4. Conclusion

In conclusion, lattice distortions were investigated in LNMO cathode materials with octahedral and plate-like morphologies. A mixed Mn oxidation state was present in pristine materials synthesized via a molten salt synthesis route. The total Mn^{3+} contents were estimated through electrochemical testing to be ~6% and ~22% for octahedral and plate materials, respectively. Nanodiffraction analysis illustrated large heterogeneities for lattice distortions in single particles, with greater distortions at particle surfaces, a screw dislocation defect in the octahedral particle, and multiple, small crystal domains in the plate particle. Large structural and phase heterogeneities are therefore likely present in the samples.

This preliminary study serves as a proof of concept for analyzing the variations in lattice distortion as a proxy for understanding phase heterogeneity in spinel LNMO. The high power density of LNMO make it an attractive cathode material, but its commercialization is hindered in part by its complex phase transition behavior. Lattice distortions and structural defects could shut down or open up local diffusion pathways for lithium ions, making the lithium ion diffusion more complicated and potentially more tortuous than that in a perfect LNMO lattice. Understanding the inherent structural and defect properties in the material under various synthesis conditions can help inform synthetic efforts to mitigate large heterogeneities, as well as provide a rational for performance degradation. Future studies expanding on this work can be undertaken to fully relate the distribution of lattice distortion to samples with various materials properties and at different states of charge. Such studies can begin to elucidate the relationship between physical properties in cathode materials that can then be used to help design and optimize materials for high-performance lithium-ion batteries.

3.5. Acknowledgments

The work was supported by the National Science Foundation under Grant No. DMR-1832613. Use of the Stanford Synchrotron Radiation Lightsource, SLAC National Accelerator Laboratory, is supported by the U.S. Department of Energy, Office of Science, Office of Basic Energy Sciences under Contract No. DE-AC02-76SF00515. This research used resources of the Advanced Photon Source, a U.S. Department of Energy (DOE) Office of Science User Facility operated for the DOE Office of Science by Argonne National Laboratory under Contract No. DE-AC02-06CH11357. This research used 3-ID of the National Synchrotron Light Source II, a U.S. Department of Energy (DOE) Office of Science User Facility operated for the DOE Office of Science by Brookhaven National Laboratory under Contract No. DE-SC0012704. The authors would like to acknowledge Dr. Chunguang Kuai for assistance with synchrotron XRD measurements and Dr. Chengjun Sun for assistance with XANES measurements.

3.6. References

(1) Armand, M.; Tarascon, J. M. Building Better Batteries. *Nature* **2008**, *451* (7179), 652–657.

(2) Patoux, S.; Daniel, L.; Bourbon, C.; Lignier, H.; Pagano, C.; Le Cras, F.; Jouanneau, S.; Martinet, S. High Voltage Spinel Oxides for Li-Ion Batteries: From the Material Research to the Application. *J. Power Sources* **2009**, *189* (1), 344–352.

(3) Santhanam, R.; Rambabu, B. Research Progress in High Voltage Spinel LiNi0.5Mn1.5O4 Material. *J. Power Sources* **2010**, *195* (17), 5442–5451.

(4) Zhong, Q. Synthesis and Electrochemistry of LiNixMn2−xO4. *J. Electrochem. Soc.* **1997**, *144* (1), 205.

(5) Huang, Y.; Dong, Y.; Li, S.; Lee, J.; Wang, C.; Zhu, Z.; Xue, W.; Li, Y.; Li, J. Lithium Manganese Spinel Cathodes for Lithium-Ion Batteries. *Adv. Energy Mater.* **2020**, 2000997.

(6) Kim, J. H.; Myung, S. T.; Yoon, C. S.; Kang, S. G.; Sun, Y. K. Comparative Study of LiNi0.5Mn1.5O 4-δ and LiNi0.5Mn1.5O4 Cathodes Having Two Crystallographic Structures: Fd3m and P4332. *Chem. Mater.* **2004**, *16* (5), 906–914.

(7) Kunduraci, M.; Al-Sharab, J. F.; Amatucci, G. G. High-Power Nanostructured LiMn2-XNixO4 High-Voltage Lithium-Ion Battery Electrode Materials: Electrochemical Impact of Electronic Conductivity and Morphology. *Chem. Mater.* **2006**, *18* (15), 3585–3592.

(8) Kim, S.; Hegde, V. I.; Yao, Z.; Lu, Z.; Amsler, M.; He, J.; Hao, S.; Croy, J. R.; Lee, E.; Thackeray, M. M.; Wolverton, C. First-Principles Study of Lithium Cobalt Spinel Oxides: Correlating Structure and Electrochemistry. *ACS Appl. Mater. Interfaces* **2018**, *10* (16), 13479–13490.

(9) Liu, G. Q.; Wen, L.; Wang, X.; Ma, B. Y. Effect of the Impurity LixNi1-XO on the Electrochemical Properties of 5 v Cathode Material LiNi0.5Mn 1.5O4. *J. Alloys Compd.* **2011**, *509* (38), 9377–9381.

(10) Duncan, H.; Hai, B.; Leskes, M.; Grey, C. P.; Chen, G. Relationships between Mn3+ Content, Structural Ordering, Phase Transformation, and Kinetic Properties in LiNixMn2-XO4 Cathode Materials. *Chem. Mater.* **2014**, *26* (18), 5374–5382.

(11) Moorhead-Rosenberg, Z.; Huq, A.; Goodenough, J. B.; Manthiram, A. Electronic and Electrochemical Properties of Li1-XMn1.5Ni0.5O4 Spinel Cathodes As a Function of Lithium Content and Cation Ordering. *Chem. Mater.* **2015**, *27* (20), 6934–6945.

(12) Xiao, J.; Chen, X.; Sushko, P. V.; Sushko, M. L.; Kovarik, L.; Feng, J.; Deng, Z.; Zheng, J.; Graff, G. L.; Nie, Z.; Choi, D.; Liu, J.; Zhang, J.-G.; Whittingham, M. S. High-Performance $LiNi_{0.5}Mn_{1.5}O_4$ Spinel Controlled by Mn^{3+} Concentration and Site Disorder. *Adv. Mater.* **2012**, *24* (16), 2109–2116.

(13) Cabana, J.; Casas-Cabanas, M.; Omenya, F. O.; Chernova, N. A.; Zeng, D.; Whittingham,

M. S.; Grey, C. P. Composition-Structure Relationships in the Li-Ion Battery Electrode Material LiNi0.5Mn1.5O4. *Chem. Mater.* **2012**, *24* (15), 2952–2964.

(14) Liu, H.; Zhang, X.; He, X.; Senyshyn, A.; Wilken, A.; Zhou, D.; Fromm, O.; Niehoff, P.; Yan, B.; Li, J.; Muehlbauer, M.; Wang, J.; Schumacher, G.; Paillard, E.; Winter, M.; Li, J. Truncated Octahedral High-Voltage Spinel LiNi0.5Mn1.5O4 Cathode Materials for Lithium Ion Batteries: Positive Influences of Ni/Mn Disordering and Oxygen Vacancies. *J. Electrochem. Soc.* **2018**, *165* (9), A1886–A1896.

(15) Casas-Cabanas, M.; Kim, C.; Rodríguez-Carvajal, J.; Cabana, J. Atomic Defects during Ordering Transitions in LiNi0.5Mn1.5O4 and Their Relationship with Electrochemical Properties. *J. Mater. Chem. A* **2016**, *4* (21), 8255–8262.

(16) Hong, S. K.; Mho, S. Il; Yeo, I. H.; Kang, Y.; Kim, D. W. Structural and Electrochemical Characteristics of Morphology-Controlled Li[Ni0.5Mn1.5]O4 Cathodes. *Electrochim. Acta* **2015**, *156*, 29–37.

(17) Aktekin, B.; Valvo, M.; Smith, R. I.; Sørby, M. H.; Lodi Marzano, F.; Zipprich, W.; Brandell, D.; Edström, K.; Brant, W. R. Cation Ordering and Oxygen Release in LiNi0.5-XMn1.5+ XO4-y (LNMO): In Situ Neutron Diffraction and Performance in Li Ion Full Cells. *ACS Appl. Energy Mater.* **2019**, *2* (5), 3323–3335.

(18) Kim, J. H.; Huq, A.; Chi, M.; Pieczonka, N. P. W.; Lee, E.; Bridges, C. A.; Tessema, M. M.; Manthiram, A.; Persson, K. A.; Powell, B. R. Integrated Nano-Domains of Disordered and Ordered Spinel Phases in LiNi0.5Mn1.5O4 for Li-Ion Batteries. *Chem. Mater.* **2014**, *26* (15), 4377–4386.

(19) Tian, C.; Xu, Y.; Nordlund, D.; Lin, F.; Liu, J.; Sun, Z.; Liu, Y.; Doeff, M. Charge Heterogeneity and Surface Chemistry in Polycrystalline Cathode Materials. *Joule* **2018**, *2* (3), 464–477.

(20) Kuppan, S.; Xu, Y.; Liu, Y.; Chen, G. Phase Transformation Mechanism in Lithium Manganese Nickel Oxide Revealed by Single-Crystal Hard X-Ray Microscopy. *Nat. Commun.* **2017**, *8*, 14309.

(21) Xu, Y.; Hu, E.; Zhang, K.; Wang, X.; Borzenets, V.; Sun, Z.; Pianetta, P.; Yu, X.; Liu, Y.; Yang, X. Q.; Li, H. In Situ Visualization of State-of-Charge Heterogeneity within a LiCoO2 Particle That Evolves upon Cycling at Different Rates. *ACS Energy Lett.* **2017**, *2* (5), 1240–1245.

(22) Finegan, D. P.; Vamvakeros, A.; Tan, C.; Heenan, T. M. M.; Daemi, S. R.; Seitzman, N.; Di Michiel, M.; Jacques, S.; Beale, A. M.; Brett, D. J. L.; Shearing, P. R.; Smith, K. Spatial Quantification of Dynamic Inter and Intra Particle Crystallographic Heterogeneities within Lithium Ion Electrodes. *Nat. Commun.* **2020**, *11* (1), 631.

(23) Hai, B.; Shukla, A. K.; Duncan, H.; Chen, G. The Effect of Particle Surface Facets on the Kinetic Properties of LiMn1.5Ni0.5O4 Cathode Materials. *J. Mater. Chem. A* **2013**, *1* (3),

759–769.

(24) Spence, S. L.; Xu, Z.; Sainio, S.; Nordlund, D.; Lin, F. Tuning the Morphology and Electronic Properties of Single-Crystal LiNi 0.5 Mn 1.5 O 4−δ : Exploring the Influence of LiCl–KCl Molten Salt Flux Composition and Synthesis Temperature. *Inorg. Chem.* **2020**, *59*, 10591–10603.

(25) Li, L.; Xie, Y.; Maxey, E.; Harder, R. Methods for Operando Coherent X-Ray Diffraction of Battery Materials at the Advanced Photon Source. *J. Synchrotron Radiat.* **2019**, *26* (1), 220–229.

(26) Ulvestad, U.; Singer, A.; Clark, J. N.; Cho, H. M.; Kim, J. W.; Harder, R.; Maser, J.; Meng, Y. S.; Shpyrko, O. G. Topological Defect Dynamics in Operando Battery Nanoparticles. *Science (80-.).* **2015**, *348* (6241), 1344–1347.

(27) Singer, A.; Ulvestad, A.; Cho, H. M.; Kim, J. W.; Maser, J.; Harder, R.; Meng, Y. S.; Shpyrko, O. G. Nonequilibrium Structural Dynamics of Nanoparticles in LiNi1/2Mn3/2O4cathode under Operando Conditions. *Nano Lett.* **2014**, *14* (9), 5295–5300.

(28) Song, J.; Shin, D. W.; Lu, Y.; Amos, C. D.; Manthiram, A.; Goodenough, J. B. Role of Oxygen Vacancies on the Performance of Li[Ni 0.5-XMn 1.5+ x]O 4 (x = 0, 0.05, and 0.08) Spinel Cathodes for Lithium-Ion Batteries. *Chem. Mater.* **2012**, *24* (15), 3101–3109.

(29) Hong, Y. S.; Huang, X.; Wei, C.; Wang, J.; Zhang, J. N.; Yan, H.; Chu, Y. S.; Pianetta, P.; Xiao, R.; Yu, X.; Liu, Y.; Li, H. Hierarchical Defect Engineering for LiCoO2 through Low-Solubility Trace Element Doping. *Chem* **2020**, *6* (10), 2759–2769.

(30) Chen, Y.; Sun, Y.; Huang, X. Origin of the Ni/Mn Ordering in High-Voltage Spinel LiNi0.5Mn1.5O4: The Role of Oxygen Vacancies and Cation Doping. *Comput. Mater. Sci.* **2016**, *115*, 109–116.

3.7. Supporting Information

3.7.1. Experimental Methods

To prepare the single-crystal LNMO samples, stoichiometric amounts of $Ni(NO_3)_2 \cdot 6H_2O$ (Sigma Aldrich) and $Mn(NO_3)_2 \cdot 4H_2O$ (Sigma Aldrich) (1:3) were dissolved in a minimum amount of deionized water. A eutectic ratio of 59:41 LiCl (Ward's Science) and KCl (Alfa Aesar) or pure LiCl salt was added and the mixture was ground in a mortar. The molar ratio of transition metals to salts was 1:30. The mixture was then heated in a 40 mL, uncovered, porcelain crucible housed in a box furnace in an air environment. The mixture was heated at a ramp rate of 2 °C/min and held for 8 hours at 650 °C or 750 °C. The resultant powers were thoroughly washed with deionized water and isopropyl alcohol to remove salt residue, then dried in a vacuum oven at 80 °C overnight to obtain LNMO.

For the electrochemical test, coin cells were prepared with LNMO cathodes comprised of 80 wt% active material, 10 wt% polyvinylidene fluoride (PVDF) binder, and 10 wt% carbon black, a Li-foil anode, and Celgard 2400 separators with $LiPF_6$ (1 M) in ethylene carbonate (EC):dimethyl carbonate (DMC) (3:7 v/v) electrolyte. The cells were cycled at 0.1 C from 3.5 to 4.9 V vs. Li/Li^+.

Particle morphology was observed with scanning electron microscopy (SEM) using a LEO FESEM at an acceleration voltage of 5.0 kV. The X-ray diffraction (XRD) patterns were acquired on beamline 11-3 at Stanford Synchrotron Radiation Lightsource (SSRL). The 2θ scale was converted to the corresponding angles with λ=1.5406 Å, the wavelength of Cu Kα radiation. Raman spectra were collected on a WITec Raman spectrometer with a 633 nm laser beam. Hard XAS measurements were acquired at beamline 20-BM-B of the Advanced Photon Source (APS) at Argonne National Laboratory. The incident beam was monochromatized using a Si (111) fixed-exit and double-crystal monochromator. Energy calibration was made by aligning the first

derivative maximum of a reference of Mn XANES spectra collected simultaneously from a metal foil in the reference channel. X-ray scanning nanodiffraction was performed at the Hard X-ray Nanoprobe beamline 3-ID at the National Synchrotron Light Source II. Bragg Coherent X-ray Diffraction was conducted at beamline 34-ID-C of the Advanced Photon Source (APS) at Argonne National Laboratory.

3.7.2. Ensemble-averaged Structural and Electronic Characterization

Figure S3-1a and **S3-1b** show the SEM images of the resultant materials which have well-defined octahedral and plate-like morphologies, respectively. Both samples have wide particle size distributions, which makes the materials suitable for different characterization techniques that have different particle size requirements. The XRD pattern of the ordered spinel phase contains additional low-intensity super-lattice peaks that are not present in the disordered phase pattern and originate from the long-range ordering of Ni and Mn.[1] The crystal structures for $P4_332$ and $Fd\bar{3}m$ spinel phases are shown in **Figures S3-1c** and **S3-1d**, respectively, to illustrate the differences in cation ordering in the two possible phases. While LNMO samples likely contain local regions of both ordered and disordered regimes, standard lab X-ray diffraction is typically unable to distinguish a small amount of the ordered phase in a highly disordered material. Synchrotron XRD was performed on the LNMO samples (**Figure S3-1e**). Low-intensity super-lattice peaks were observed in the octahedral sample at (310), (330)/(411), and (510) Bragg positions with lower intensity than the calculated peaks for a full ordered spinel, indicating that some fraction of the material is ordered (**Figure S3-1f**). While powder XRD is informative of crystal structure, it only provides bulk sample information. High-spatial resolution diffraction is therefore often necessary to identify and quantify the distribution of the different phase regions within the particles.

X-ray absorption spectroscopy (XAS) analysis can be used to characterize local structure and oxidation state information for certain elements in a given material. We have previously performed soft XAS analysis to probe the transition metal oxidation states on the surface (2-5 nm) and sub-surface (up to 50 nm) of the materials.[2] Results indicated that LNMO surfaces contain slightly more reduced Mn than the sub-surface and the bulk due to the possible oxygen loss and impurity formation which are more favorable on the material surface.[3] Ni oxidation state has been examined by soft XAS and showed that Ni is consistent in the 2+ state, which is expected for pristine LNMO material.[3] X-ray absorption near-edge structure (XANES) analysis provides a bulk probe of materials and shows that for both octahedral and plate LNMO samples, the Mn K-edge energy is in-between that of the Mn^{3+} and Mn^{4+} reference spectra (edge energies of the spectra are defined as energies at half-height of the white-line peak) (**Figure S3-1g**). This spectral shape is characteristic of Mn coordination in a spinel structure with an oxidation state close to 4+.[4,5] Based on the pre-edge, it appears that the plate sample has a slightly lower Mn average valence state.

Extended X-ray absorption fine structure (EXAFS) can be examined to evaluate quantitative structural information including coordination number and inter-atomic distances. Fourier transforming the Mn K-edge EXAFS spectra in R-space (k^3 weighting) gives information on the Mn-O and Mn-(Mn, Ni) atomic distances in spinel LNMO, which are located at 1.50 and 2.52 Å, respectively (**Figure S3-1h**).[6,7] The plate sample shows slightly smaller inter-atomic distances compared to the octahedral sample which can be attributed to the influence of more impurity phases. Additionally, the presence of Mn^{3+} in a material can lead to the distorted MnO_6 octahedra resulting from Jahn-Teller distortion, which can decrease the magnitude of the Mn-O bond.[8] This is observed for the plate-like sample indicating more Jahn-Teller distortion.

The discharge profile was also used to investigate electrochemical properties in the LNMO materials (**Figure S3-1i**). The LNMO cathodes were cycled at 0.1 C from 3.5 to 4.9 V vs Li/Li^+. Electrochemical activity is largely due to a two-step Ni^{2+}/Ni^{3+} redox reaction, however, electrochemically active Mn^{3+} can also participate; subsequently a Mn^{3+}/Mn^{4+} redox reaction results in a small voltage plateau at approximately 4.0 V. The percentage of total capacity obtained between 3.8 to 4.25 V can be used to estimate the total Mn^{3+} in the sample. For our samples, Mn^{3+} content was estimated from the discharge profiles to be 5.7% for the octahedral sample and 22.0% for the plate sample. The average Mn valence state was then calculated as 3.94 and 3.78 for octahedral and plate samples, respectively, which is consistent with the pre-edge features of the Mn K-edge XAS (**Figure S3-1g**). A large presence of Mn^{3+} suggests materials may contain both ordered and disordered regions. Cycling performance for both materials over 50 cycles at 0.1 C-rate and at various C-rates is shown in **Figure S3-2**. The plate sample shows a lower specific capacity due to the presence of electrochemically inactive impurity phases, but better rate capability performance, which may potentially be due to large quantities of Mn^{3+} increasing solid solution behavior during ion intercalation and deintercalation.

Raman spectroscopy is also sensitive to local crystal structure and was performed to determine the degree of Ni and Mn ordering in the LNMO samples (**Figure S3-3**). Peak splitting at 600 cm^{-1} and the appearance of low-intensity peaks at ~230 and ~260 cm^{-1} are fingerprints of the lower symmetry ordered phase.[9,10] The absence of such features indicates the materials are highly disordered, however, Raman spectroscopy can be limited by the thickness of the material, making the quantification relatively surface sensitive.

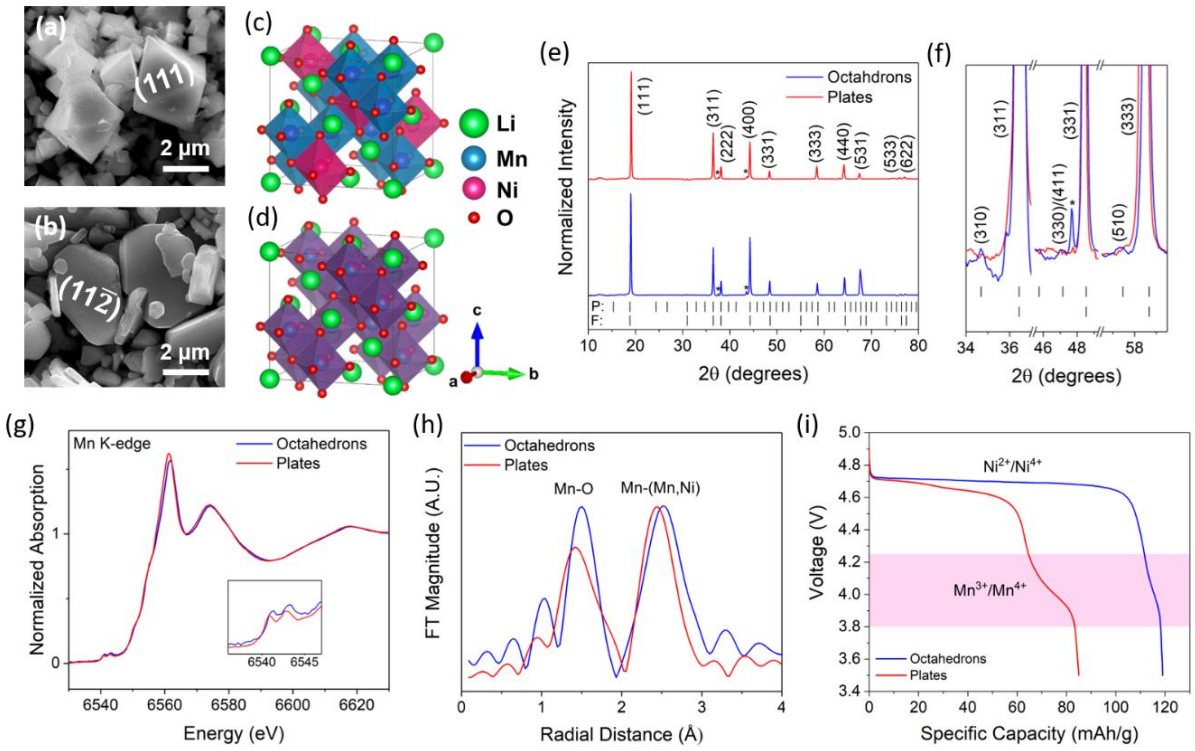

Figure S3-1. SEM of **(a)** octahedral and **(b)** plate LNMO samples. Crystal structures of **(c)** $Fd\bar{3}m$ and **(d)** $P4_332$ LNMO. Blue octahedrons represent Mn and fuchsia octahedrons represent Ni. **(e)** Synchrotron XRD patterns of LNMO and **(f)** expanded view of the (311), (331), and (333) and corresponding (310), (330)/(411), and (510) superlattice peaks. Asterisks indicate impurity phases. F = location of $Fd\bar{3}m$ diffraction peaks. P = location of $P4_332$ diffraction peaks. **(g)** Mn K-edge X-ray absorption near-edge structure (XANES) spectra. **(h)** Fourier-transformed Mn K-edge extended X-ray absorption fine structure (EXAFS). **(i)** Discharge curves of LNMO. Capacity contribution in the 3.8 – 4.25 V region is due to the Mn^{3+}/Mn^{4+} redox.

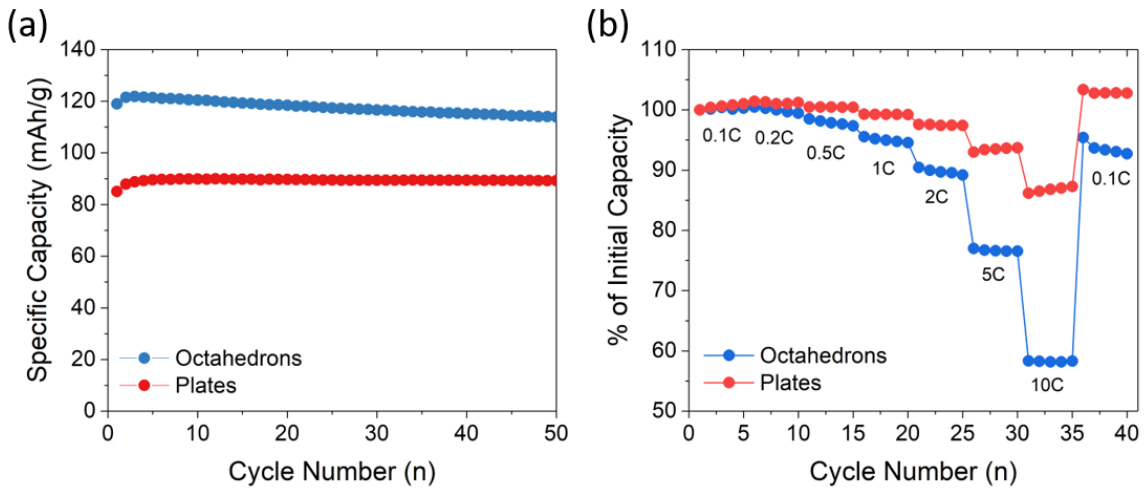

Figure S3-2. Cycling performance of LNMO octahedron and plate samples between 3.5 and 4.9 V at **(a)** 0.1 C-rate over 50 cycles and **(b)** at various C-rates.

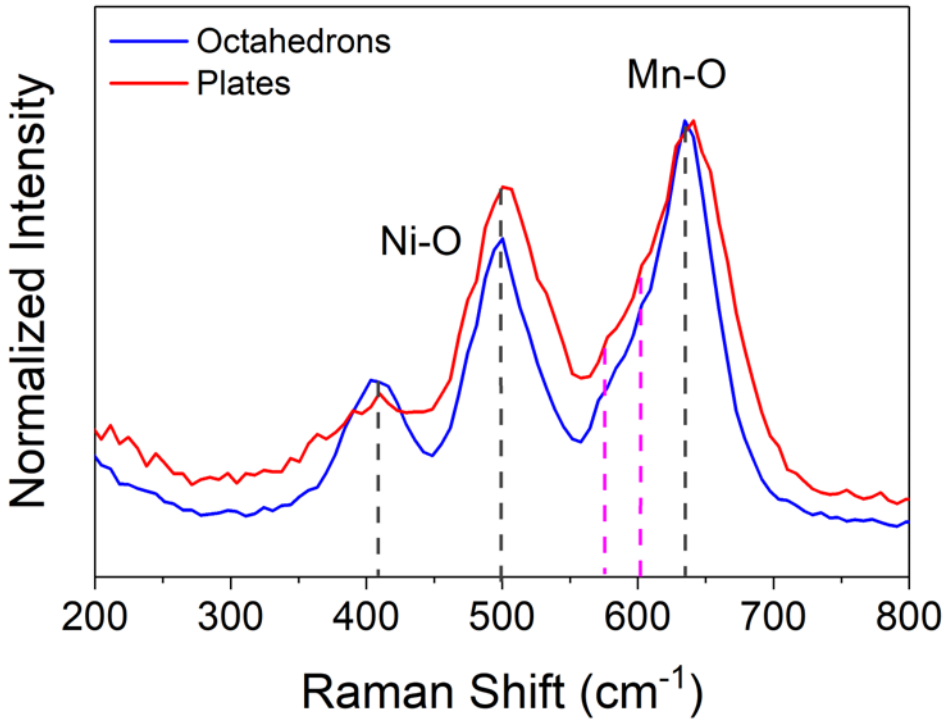

Figure S3-3. Raman spectrum of LNMO.

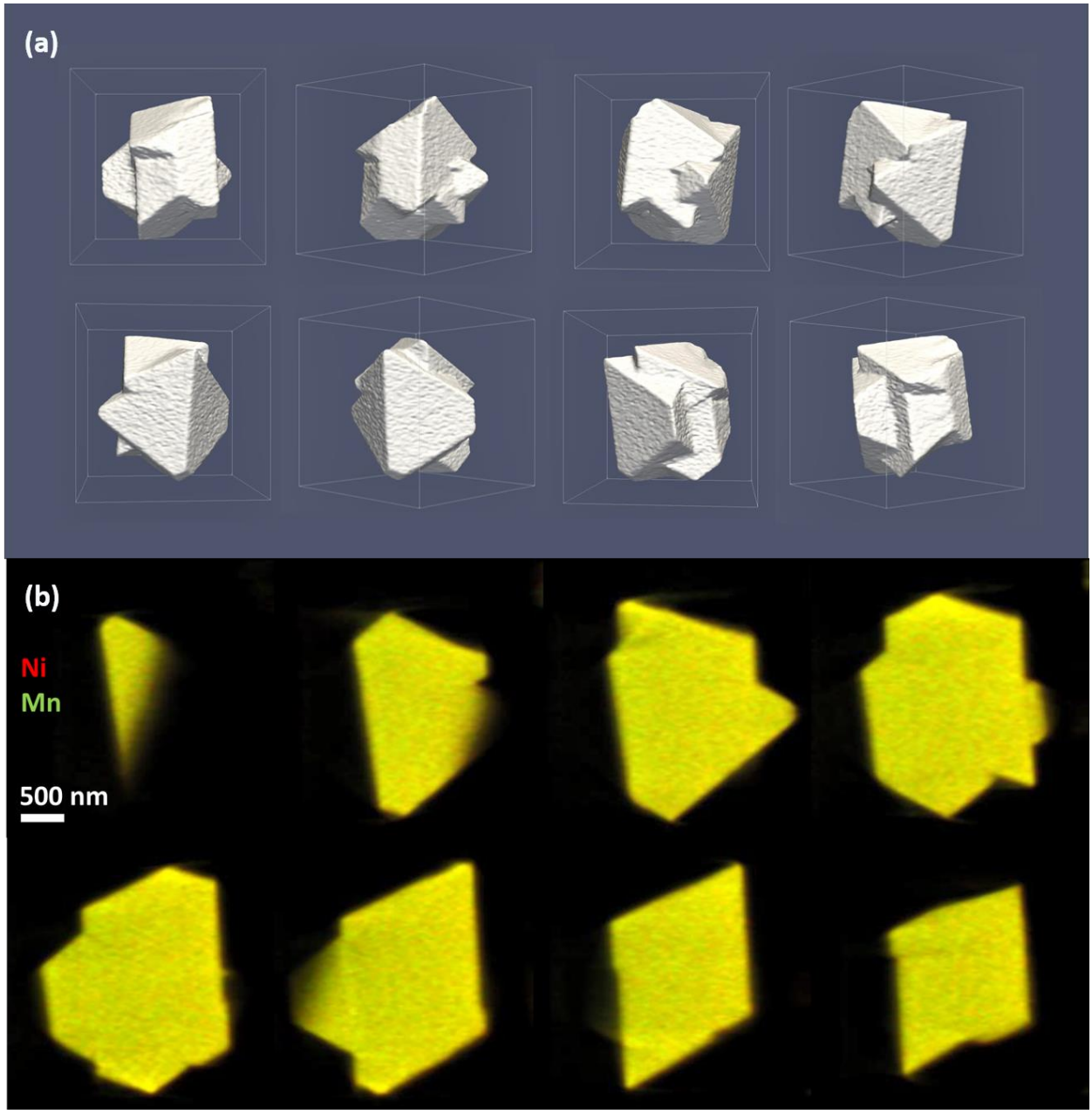

Figure S3-4. (a) Octahedral target particle 3D tomography reconstruction. **(b)** Octahedral target particle X-ray fluorescence mapping slices as a function of particle depth. The pixel size of the fluorescence images are 50 x 50 nm^2.

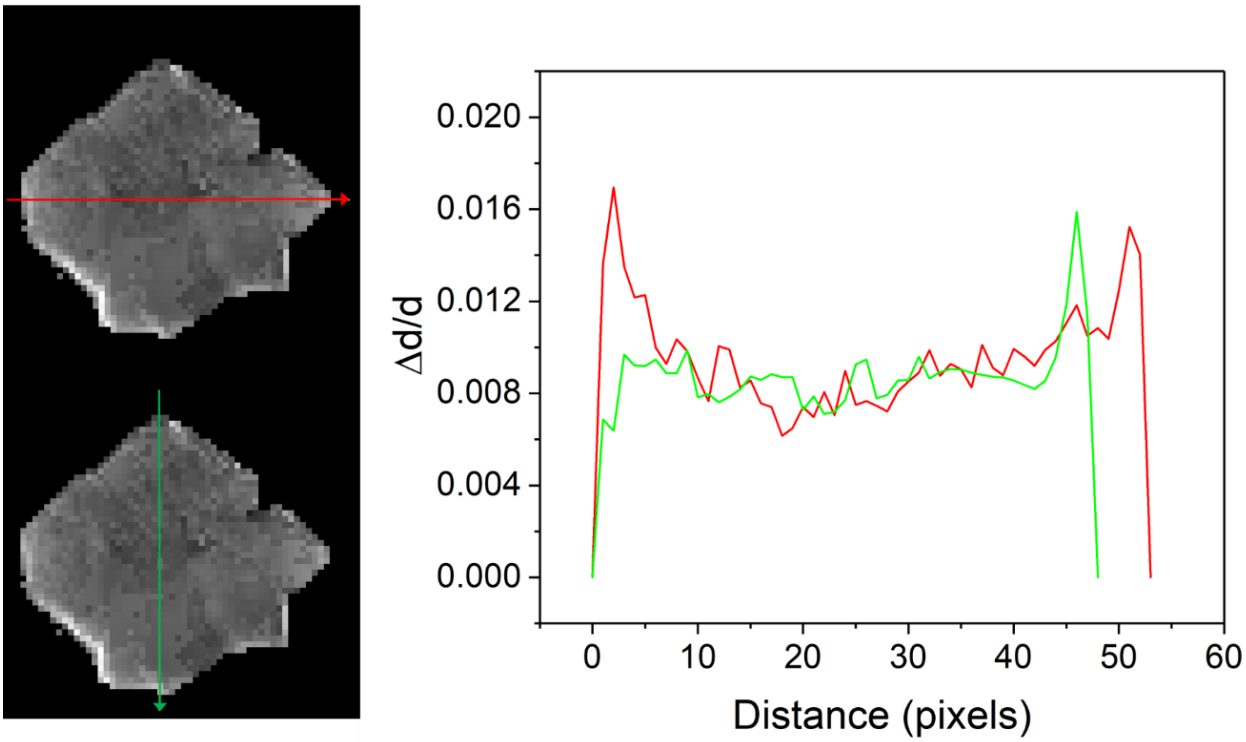

Figure S3-5. Lattice variation depth profile for octahedral particle at (311) Bragg reflection.

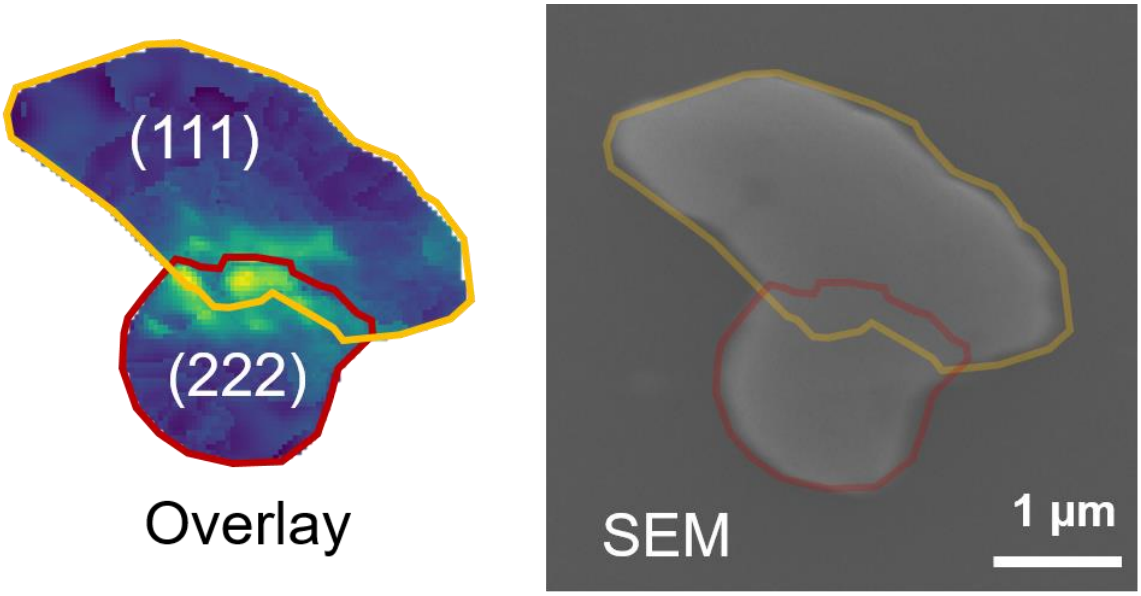

Figure S3-6. Overlay of (111) and (222) nanodiffraction strain maps compared to SEM of the full target particle for the plate sample.

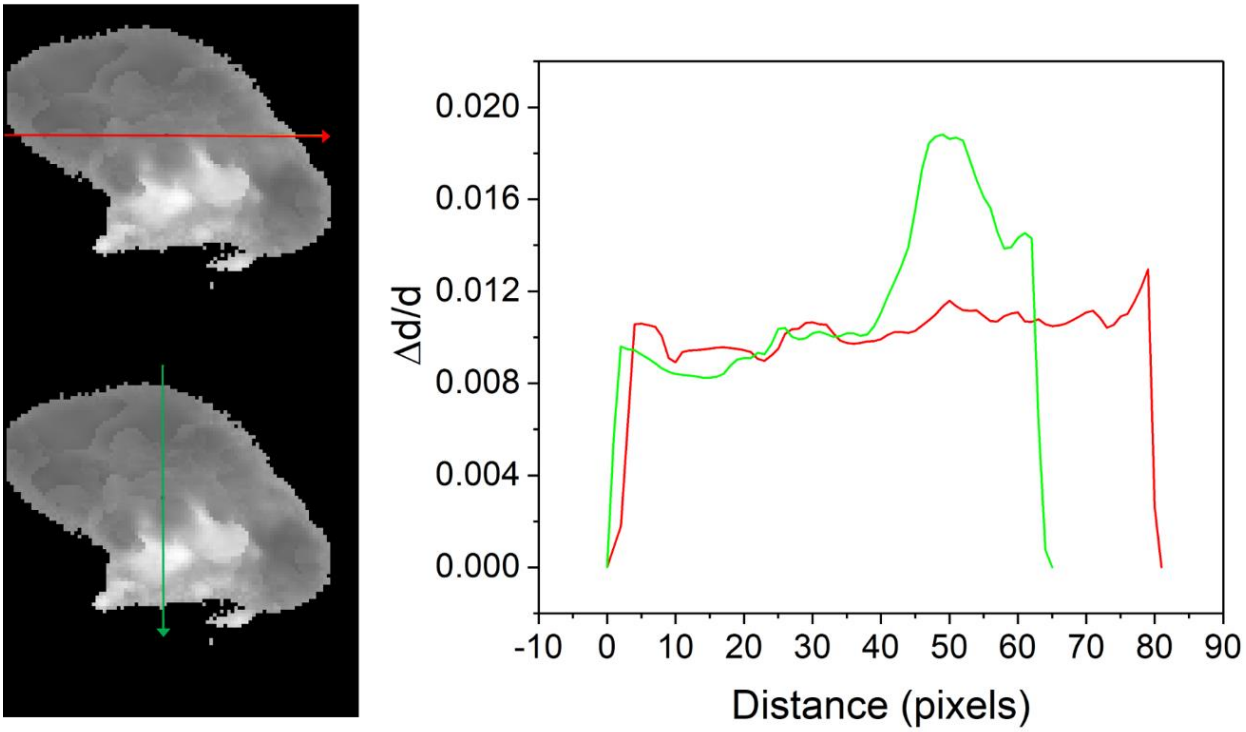

Figure S3-7. Lattice variation depth profile for plate particle at (311) Bragg reflection.

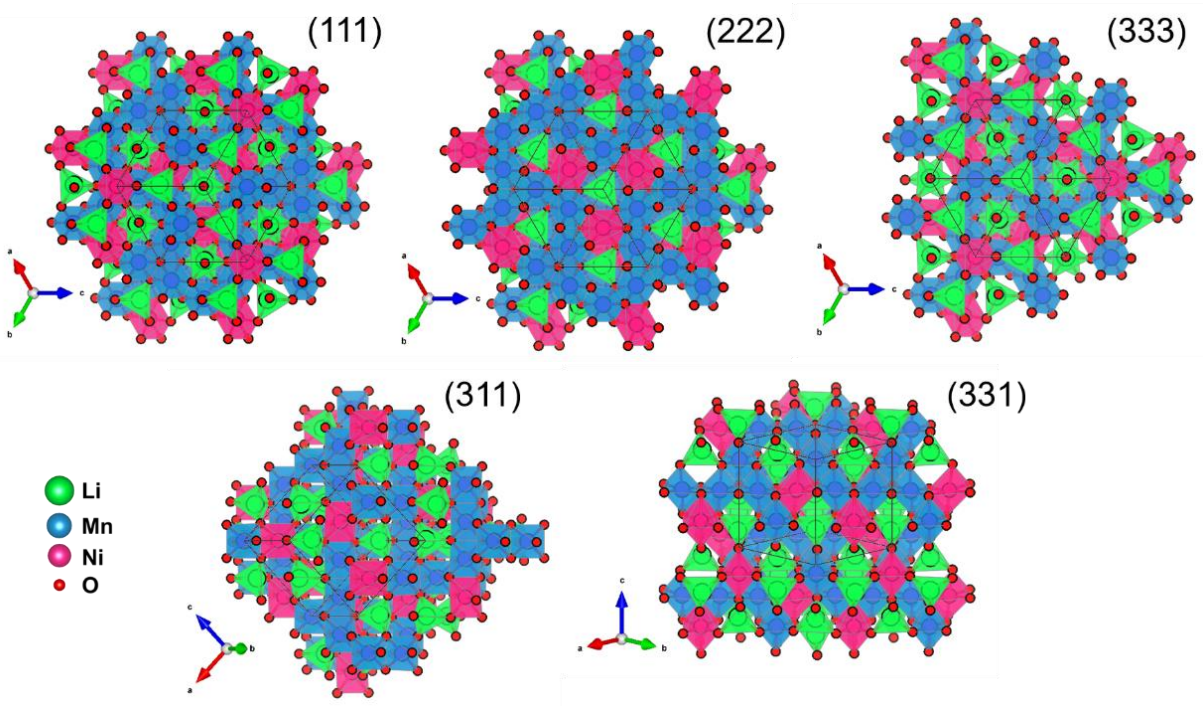

Figure S3-8. Schematic of atomic arrangements at different surface orientations of $P4_332$ cubic spinel. In the $Fd\bar{3}m$ cubic spinel, Mn and Ni are randomly arranged.

Supporting Movies available at: https://pubs.acs.org/doi/10.1021/acsenergylett.1c02759.

3.7.3. References

(1) Kim, J. H.; Myung, S. T.; Yoon, C. S.; Kang, S. G.; Sun, Y. K. Comparative Study of LiNi0.5Mn1.5O 4-δ and LiNi0.5Mn1.5O4 Cathodes Having Two Crystallographic Structures: Fd3m and P4332. *Chem. Mater.* **2004**, *16* (5), 906–914.

(2) Lin, F.; Liu, Y.; Yu, X.; Cheng, L.; Singer, A.; Shpyrko, O. G.; Xin, H. L.; Tamura, N.; Tian, C.; Weng, T.-C.; Yang, X.-Q.; Meng, Y. S.; Nordlund, D.; Yang, W.; Doeff, M. M. Synchrotron X-Ray Analytical Techniques for Studying Materials Electrochemistry in Rechargeable Batteries. *Chem. Rev.* **2017**, *117* (21), 13123–13186.

(3) Spence, S. L.; Xu, Z.; Sainio, S.; Nordlund, D.; Lin, F. Tuning the Morphology and Electronic Properties of Single-Crystal LiNi 0.5 Mn 1.5 O 4−δ : Exploring the Influence of LiCl–KCl Molten Salt Flux Composition and Synthesis Temperature. *Inorg. Chem.* **2020**, *59*, 10591–10603.

(4) Greco, G.; Brutti, S.; Vitucci, F. M.; Lombardo, L.; Köntje, M.; Savoini, A.; Paolone, A.; Panero, S. Investigation of the Chemical Disorder of LiNi 0.5 Mn 1.5 O 4 Lattice by Means of Extended X-Ray Absorption Fine Structure Spectroscopy. *J. Phys. Chem. C* **2014**, *118* (46), 26471–26478.

(5) Ammundsen, B.; Jones, D. J.; Rozière, J.; Burns, G. R. Effect of Chemical Extraction of Lithium on the Local Structure of Spinel Lithium Manganese Oxides Determined by X-Ray Absorption Spectroscopy. *Chem. Mater.* **1996**, *8* (12), 2799–2808.

(6) Terada, Y.; Yasaka, K.; Nishikawa, F.; Konishi, T.; Yoshio, M.; Nakai, I. In Situ XAFS Analysis of Li(Mn, M)2O4 (M = Cr, Co, Ni) 5 V Cathode Materials for Lithium-Ion Secondary Batteries. *J. Solid State Chem.* **2001**, *156* (2), 286–291.

(7) Yoon, J.; Kim, D.; Um, J. H.; Jeong, M.; Oh, W.; Yoon, W. S. Effect of Local Structural Changes on Rate Capability of LiNi0.5Mn1.5O4-δ Cathode Material for Lithium Ion Batteries. *J. Alloys Compd.* **2016**, *686*, 593–600.

(8) Rana, J.; Glatthaar, S.; Gesswein, H.; Sharma, N.; Binder, J. R.; Chernikov, R.; Schumacher, G.; Banhart, J. Local Structural Changes in LiMn1.5Ni0.5O4 Spinel Cathode Material for Lithium-Ion Batteries. *J. Power Sources* **2014**, *255*, 439–449.

(9) Amdouni, N.; Zaghib, K.; Gendron, F.; Mauger, A.; Julien, C. M. Structure and Insertion Properties of Disordered and Ordered LiNi 0.5Mn1.5O4 Spinels Prepared by Wet Chemistry. *Ionics (Kiel).* **2006**, *12* (2), 117–126.

(10) Liu, H.; Wang, J.; Zhang, X.; Zhou, D.; Qi, X.; Qiu, B.; Fang, J.; Kloepsch, R.; Schumacher, G.; Liu, Z.; Li, J. Morphological Evolution of High-Voltage Spinel LiNi0.5Mn1.5O4 Cathode Materials for Lithium-Ion Batteries: The Critical Effects of Surface Orientations and Particle Size. *ACS Appl. Mater. Interfaces* **2016**, *8* (7), 4661–4675.

Chapter 4. Heterogeneous Evolution of Lattice Distortions and Mn Dissolution Behavior in High-Voltage $LiNi_{0.5}Mn_{1.5}O_4$ Cathode Materials: How Close Does Chemical Delithiation Approximate Electrochemical Charging?

Stephanie L. Spence[1], Anyang Hu[1], Sami Sainio[2], Dennis Nordlund[2], Xiaojing Huang[3], Feng Lin[1*]*

[1]Department of Chemistry, Virginia Tech, Blacksburg, VA 24061, USA

[2]Stanford Synchrotron Radiation Lightsource, SLAC National Accelerator Laboratory, Menlo Park, CA 94035, USA

[3]National Synchrotron Light Source II, Brookhaven National Laboratory, Upton, NY 11973, USA

4.1. Abstract

Spinel $LiNi_{0.5}Mn_{1.5}O_4$ (LNMO) is an attractive cathode material for its high voltage of operation (~4.7 V vs Li/Li^+) allowing for high power density and robust three-dimensional Li-ion conduction channels allowing for fast charging. It is well established that the cation ordering of Ni and Mn can influence the electrochemical performance of the material, where disordering is associated with the presence of Mn^{3+}. This material is plagued by Mn dissolution and heterogeneous phase change during Li^+ removal, which can exacerbate particle degradation and capacity fading. Li^+ removal, Mn dissolution, and phase transformations each influence the lattice variation in spinel cathode materials during charging. Herein, a high-spatial-resolution X-ray nanodiffraction study is developed and employed to observe lattice distortion evolution at the tens-of-nanometer scale in plate LNMO single-crystals upon chemical delithiation. With deep delithiation, lattice distortion distribution increases heterogeneously within the particle. Fracturing is found to occur primarily at domain boundaries between nano-sized grains. We conclude that aggressive chemical delithiation methods lead to crack formation which may result from severe transition metal dissolution and are not always viable to replicate electrochemical cycling conditions. While materials' interactions with electrolytes under practical operating conditions must be taken into account, our results offer fundamental insights into the degradation mechanisms of single crystal LNMO utilizing *ex situ* nanodiffraction measurement techniques that may aid research efforts in studying and developing stable high-voltage cathodes.

4.2. Introduction

Of Li-ion battery (LIB) active cathode materials, $LiNi_{0.5}Mn_{1.5}O_4$ (LNMO) is of great interest due to its inherent high voltage, high energy density, and robust three-dimensional spinel

framework allowing for extended cycling stability and fast Li-ion transport enabling high rate capability.[1] In addition, spinel LNMO is a cost-effective and Co-free alternative to layered materials based on commercial $LiCoO_2$ and $LiNi_{1-x-y}Mn_xCo_yO_2$.[2] Polymorphs of LNMO include a $P4_332$ ordered spinel and an $Fd\bar{3}m$ disordered spinel structure, which differ in their arrangement of Ni and Mn cations.[3] Pure ordered or disordered spinel phase materials are difficult to synthesize. Practically, short-range ordered regions of Ni and Mn are found to proliferate even in a highly disordered material.[4,5] Antiphase boundaries can hinder Li-ion transport, negatively affecting the reversible rate performance of the material.[4] Crystallographic heterogeneities within particles complicate attempts to reveal structure-property relationships in LNMO and thus, understanding of inherent heterogeneities utilizing both lab-based and advanced X-ray techniques has been the focus of several studies.[4,6,7]

In LNMO, Ni^{2+}/Ni^{4+} dual redox occurs at approximately 4.7 V vs Li/Li^+. Phase transformations upon Li^+ removal maintain the cubic spinel framework with a two-phase reaction occurring in the ordered spinel and a solid solution reaction occurring for the disordered spinel.[8,9] Approximately 3% and 3.3% volume change occurs during the transitions from $LiNi_{0.5}Mn_{1.5}O_4$ to $Li_{0.5}Ni_{0.5}Mn_{1.5}O_4$ to $Ni_{0.5}Mn_{1.5}O_4$.[10,11] The solid solution behavior is kinetically advantageous and contributes to improved ionic conductivity and rate capability observed in the disordered spinel material.[12] Two- or three-phase intra-particle coexistence has been observed, suggesting large heterogeneity of delithiation.[10] Large volume change and lattice mismatch between cubic phases can lead to strain accumulation in particles and induce mechanical degradation and failure of the cathode.

While the fully ordered material contains Mn in a stoichiometric 4+ oxidation state, the presence of a small amount of Mn^{3+} is associated with the high temperature formation of the

disordered spinel phase and plays a large part in dictating the properties and electrochemical performance of LNMO.[9,13–16] On the one hand, the presence of Mn^{3+} has been found to increase the electronic conductivity by two orders of magnitude, providing superior rate capability.[17] On the other hand, Mn^{3+} is well known to disproportionate into Mn^{2+} and Mn^{4+} leading to the dissolution of active material into the electrolyte.[18–20] Dissolution of Mn^{3+} ions via the disproportionation reaction can migrate through the electrolyte and deposit on the anode, poisoning the solid-electrolyte interphase (SEI) and leading to severe capacity fading and as such is a major barrier to the commercialization of LNMO.[21] Disproportionation can be caused by trace amounts of acidic HF present in the electrolyte [22,23] However, Mn^{3+} disproportionation is not the sole cause of Mn dissolution in cathode materials, as increased dissolution and Mn reduction at particle surfaces have been reported upon charging spinel materials to voltages higher than 4.1 V (where all Mn should be in the 4+ oxidation state).[24,25] The surface instability of highly delithiated materials can lead to oxygen migration and loss, electrolyte oxidation, and surface rearrangement to Mn_3O_4 phases containing more soluble Mn^{2+}, thus leading to significant Mn dissolution.[25,26]

Chemical delithiation is widely adopted as a method to study battery cathode materials at different states of charge; however, it is not fully determined if the properties of chemically delithiated samples can accurately represent the properties of the material under electrochemical cycling.[27,28] The amount of Li^+ chemically extracted from spinel $LiMn_2O_4$ (LMO) in acidic conditions was found to be proportional to the initial amount of Mn^{3+}.[29] Disproportionation of Mn^{3+} is therefore reported to be the only mechanism of Li^+ removal and Mn dissolution in chemically delithiated spinel samples in acidic conditions, in contrast to the case of electrochemical cycling discussed above. Strong oxidizing agents such as NO_2BF_4 in acetonitrile with a potential of ~5.1 V vs Li/Li^+ can be used to controllably remove Li^+ from spinel LMO and

LNMO[11,30,31] Trace water impurities in acetonitrile or acetonitrile decomposition can provide protons that can facilitate transition metal dissolution.[32] Additionally, in chemically delithiated samples, more severe cracking is reported to occur due to the rapid removal of Li^+ which may increase particle surface areas and accelerate dissolution and harmful side reactions.[27] Rapid Li^+ removal can also lead to more pronounced variations in local concentrations and significant particle heterogeneity.[10] Despite the limitations to chemical delithiation, it is a useful tool when *in situ* electrochemical cycling is not feasible.

Our earlier study focused on revealing the heterogeneity of lattice distortions in LNMO samples prepared with differing percentages of cation disordering and Mn^{3+}.[7] In this work, we use high-spatial-resolution nanodiffraction to examine lattice distortion evolution upon chemical delithiation and reveal spatial strain development in a disordered LNMO sample with plate morphology and approximately 20% of the total capacity obtained from electrochemically active Mn^{3+}. This method can be used as an experimental platform to track materials degradation, which can cause additional transition metal dissolution and capacity fading. We discuss Mn dissolution behaviors during chemical delithiation and the viability of chemical delithiation to replicate electrochemical cycling conditions. In the pristine material, lattice variation is expected to coincide with order/disorder local phase heterogeneity as Mn^{3+} has a larger ionic radius than Mn^{4+}. Upon deep delithiation, we hypothesize that lattice distortions increase as Li^+ removal, Mn dissolution, and cubic phase transformations occur heterogeneously in disordered and ordered local regions. The phase heterogeneity and increased amount of antiphase boundaries can be barriers to Li^+ transport and contribute to loss of performance in LNMO over long-term cycling.

4.3. Results and Discussion

4.3.1. Evolution of Lattice Defects Investigated through Nanodiffraction Mapping

To examine the evolution of structural heterogeneity in high-voltage LNMO materials, an *ex situ* study was designed using high-spatial-resolution X-ray nanodiffraction to measure lattice distortions in a single particle before and after chemical delithiation treatment. LNMO material with plate-like morphology was synthesized according to a molten salt synthesis method.[13,33] **Figure 3-1a** shows the scanning electron microscopy (SEM) image of the pristine target particle for nanodiffraction measurements. It has been reported that the plate-like morphology preferentially exposes $(11\bar{2})$ surfaces. A set of nanodiffraction measurements were performed on the target particle and then the particle was chemically delithiated by gently stirring the mounted sample in a solution of NO_2BF_4 in acetonitrile. Nanodiffraction was then re-measured on the same particle. The SEM of the particle after chemical delithiation is shown in **Figure 4-1b**. The particle well maintains its shape after chemical delithiation; however, severe physical degradation of the surface is observed.

Nanodiffraction measurements were carried out using a Hard X-ray Nanoprobe (HXN). The schematic of the experimental setup is shown in **Figure 4-1c**. In the HXN measurement, the sample is illuminated with X-rays focused to a ~30 nm spot size, and diffraction patterns are collected at orientations where the Bragg condition is satisfied.[34] 2D raster scanning is performed as the sample is rotated in the vicinity of a selected Bragg angle to produce the rocking curves shown in **Figure 4-1d**. Selecting pixels at different locations in the 3D rocking curve shows the variation in the maximum intensity of the Bragg angle within the particle due to inherent structural heterogeneity. The shift in the 3D Bragg diffraction pattern can be deconvoluted into three orthogonal directions, which represent the relative change in *d*-spacing, lattice bending along the

y-axis, and lattice twisting along the *z*-axis. Performing this deconvolution at each pixel results in spatially resolved maps with 50 x 50 nm^2 resolution that can be used to visualize the distribution of lattice distortions within the particle. Spinel LNMO is structurally robust enough to withstand repeated measurements and an on-the-fly scan mode was used to mitigate radiation damage.

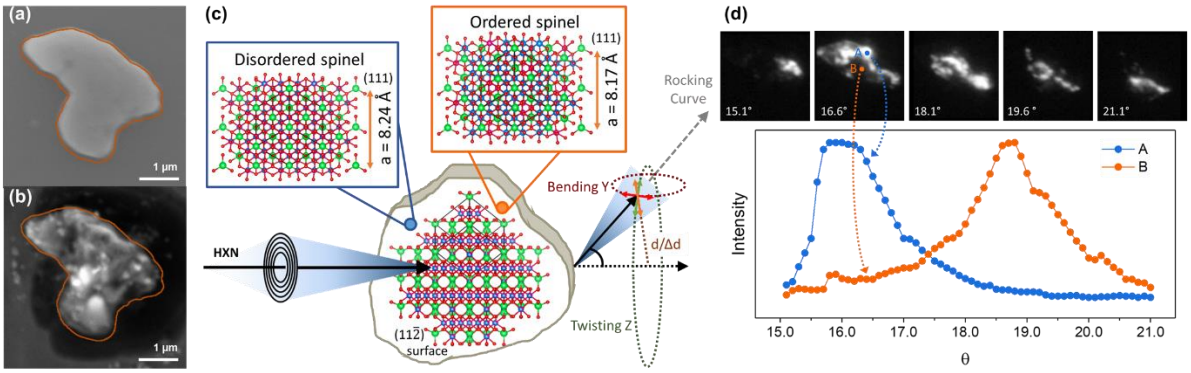

Figure 4-1. SEM images of target plate LNMO particle **(a)** before and **(b)** after chemical delithiation treatment. **(c)** Schematic of the HXN experimental setup and atomic structures of the (11$\bar{2}$) surface and the (111) planes containing different lattice parameters, a, in ordered and disordered spinel phases. **(d)** 2D rocking curves as a function of θ and corresponding Bragg intensity as a function of θ at two pixels in the particle.

Nanodiffraction maps were collected at Bragg angles corresponding to (111), (311), and (222) planes (**Figure 4-2**, **4-3**, and **4-4**). Color maps represent the relative variation of the lattice distortion. Two large regions with slightly different orientations are observed within the pristine particle resulting in a different map shape for the (222) measurement. Overlaid, they form the shape of the full plate particle. The change in *d*-spacing, $\Delta d/d$, or strain maps are shown in **Figure 4-2**. Spatial heterogeneity of the *d*-spacing is present in the pristine sample with increased strain at the boundary between the two large crystal domains (**Figure 4-2a**). The *d*-spacing averaged

across the entire map was calculated from the (311) peak to be 0.2548 nm before chemical delithiation, consistent for disordered spinel LNMO material. After chemical treatment, additional smaller, individual domains are present with a larger fluctuation of distortions (**Figure 4-2b**). Large grains present in the pristine map break down as severe distortion increases. The crystal orientations of these small grains may also change after treatment, and as a result, the total areas and shapes of the maps change significantly. Local nanocrystals may rotate as neighboring transition metals are dissolved, or the highly delithiated crystals may change their lattice parameter significantly and no longer satisfy the Bragg condition at the measured angle. Histograms comparing the distortion intensity for overlapping regions of pixels present in both the pristine and treated maps (indicated by highlighted regions in the distortion maps) further reveal increased lattice distortion heterogeneity after the chemical treatment (**Figure 4-2c**). The overlapping regions are limited in size, but provide a fair comparison of the same local regions of the particle before and after chemical delithiation treatment.

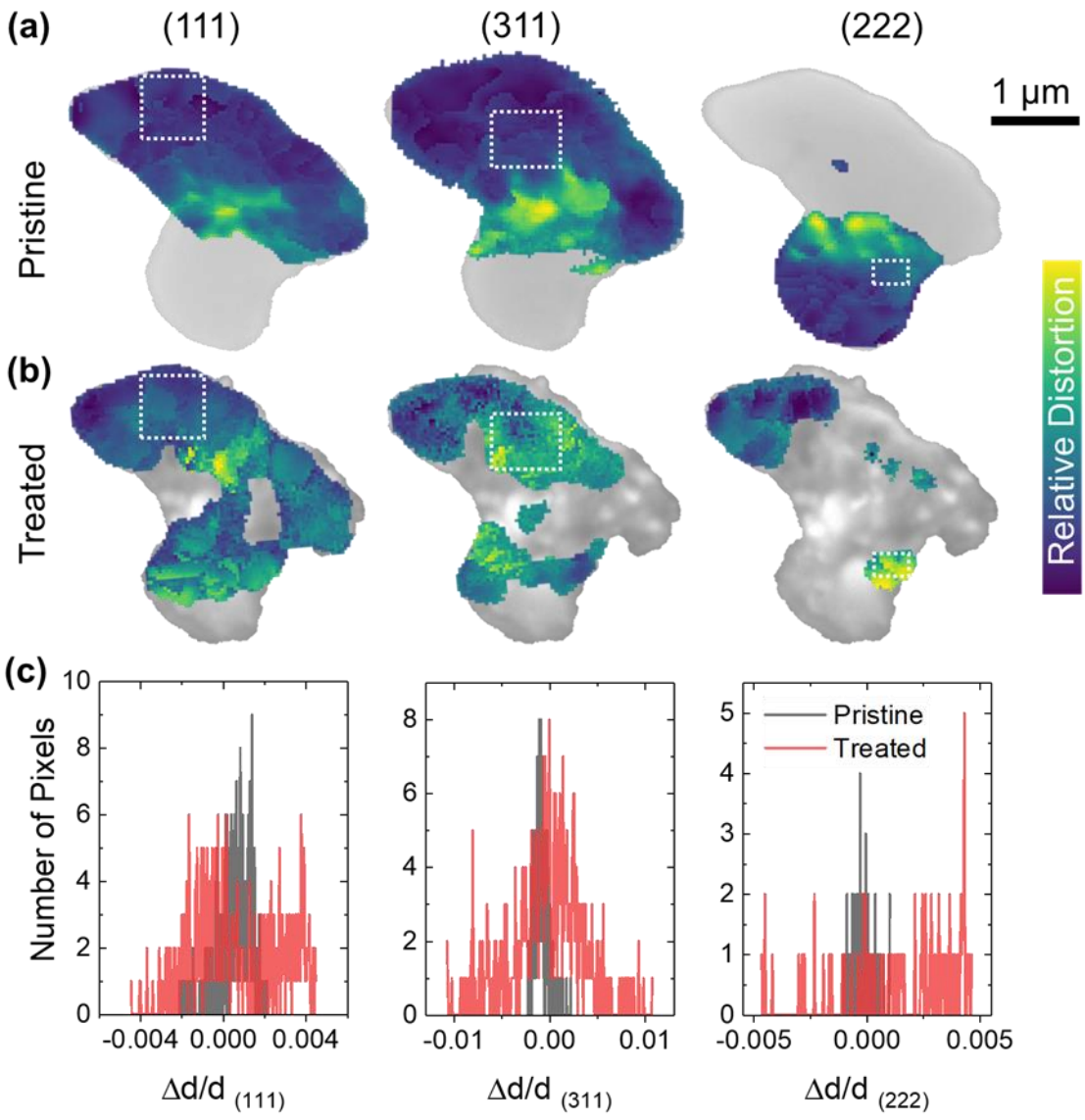

Figure 4-2. Distortion maps of Δ*d/d*, or lattice strain, for the **(a)** pristine LNMO particle and **(b)** after chemical delithiation treatment at each Bragg location. The color bar represents the relative distortion intensity where blue is less intense and yellow is more intense. **(c)** Histograms of lattice distortion distributions comparing overlapping regions (in white outline) in pristine and treated maps. Plots are shifted to be centered at 0.0. Pristine maps are adapted with permission.[7] 2022, American Chemical Society.

Figure 4-3 and **4-4** show comparisons of the pristine and treated distortion maps for bending *y*-axis and twisting *z*-axis lattice distortions, respectively. These out-of-plane distortions indicate that the particle is not completely flat. Once again, large heterogeneities are present with larger distortion intensities located closer to the intra-particle grain boundary for the pristine maps (**Figure 4-3a** and **4-4a**). More localized domains with abrupt changes in distortion intensity between them are observable in the bending *y*-axis and twisting *z*-axis maps compared to the strain maps. After chemical delithiation, these domains are further broken down into nano-sized regions (**Figure 4-3b** and **4-4b**). From the regional comparison histograms, increased distortion of *y*-axis bending is observed at each Bragg location after chemical delithiation (**Figure 4-3c**). For *z*-axis twisting, the map at the (311) peak shows more severe distortion initially; however, after chemical treatment, larger pixel-to-pixel variation is seen, indicating large fluctuations of lattice distortions between nanodomains (**Figure 4-4c**).

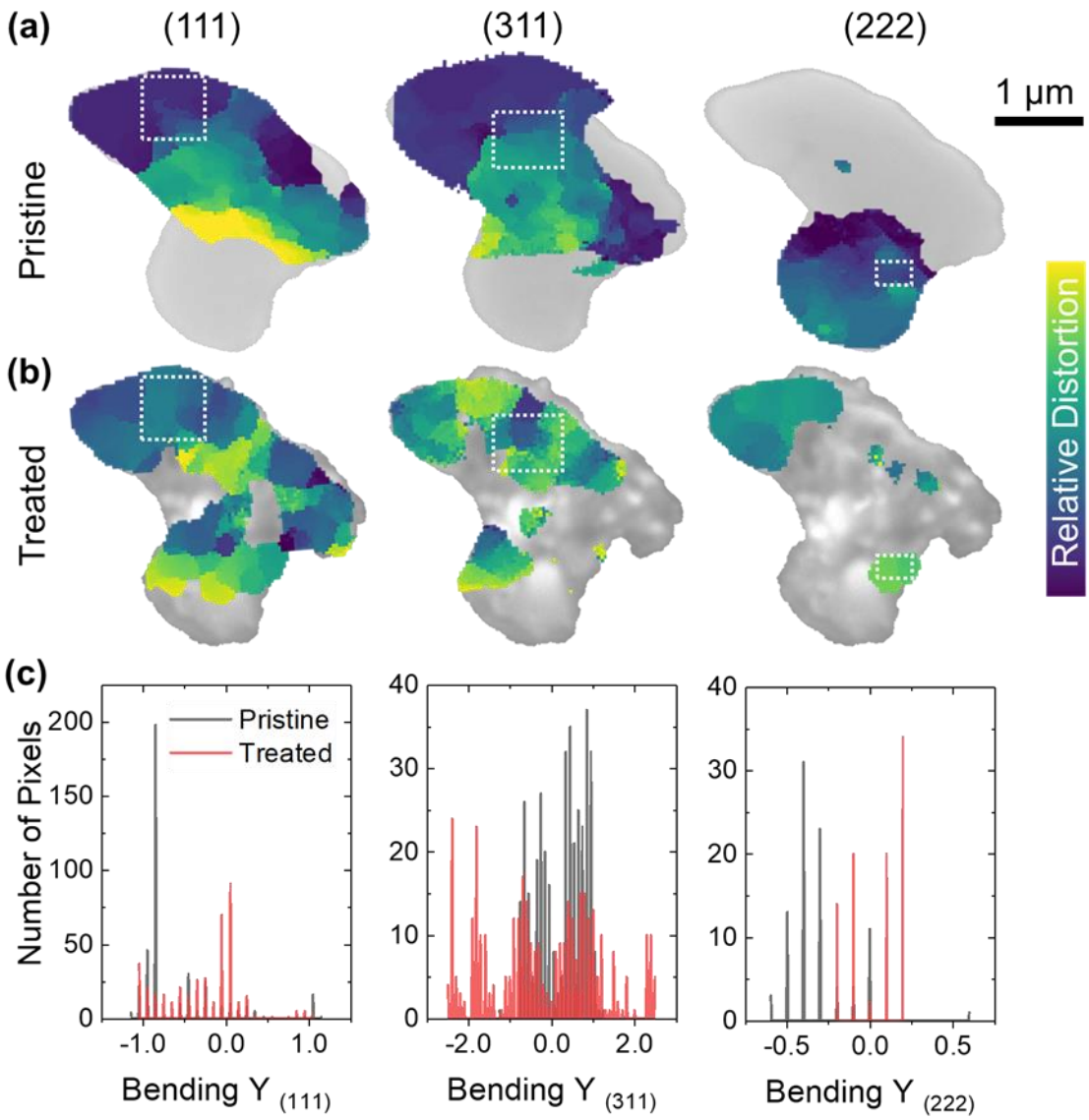

Figure 4-3. Distortion maps of lattice bending along the *y*-axis, for the **(a)** pristine LNMO particle and **(b)** after chemical delithiation treatment at each Bragg location. The color bar represents the relative distortion intensity where blue is less intense and yellow is more intense. **(c)** Histograms of lattice distortion distributions comparing overlapping regions (in white outline) in pristine and treated maps. Plots are shifted to be centered at 0.0. Pristine maps are adapted with permission.[7] 2022, American Chemical Society.

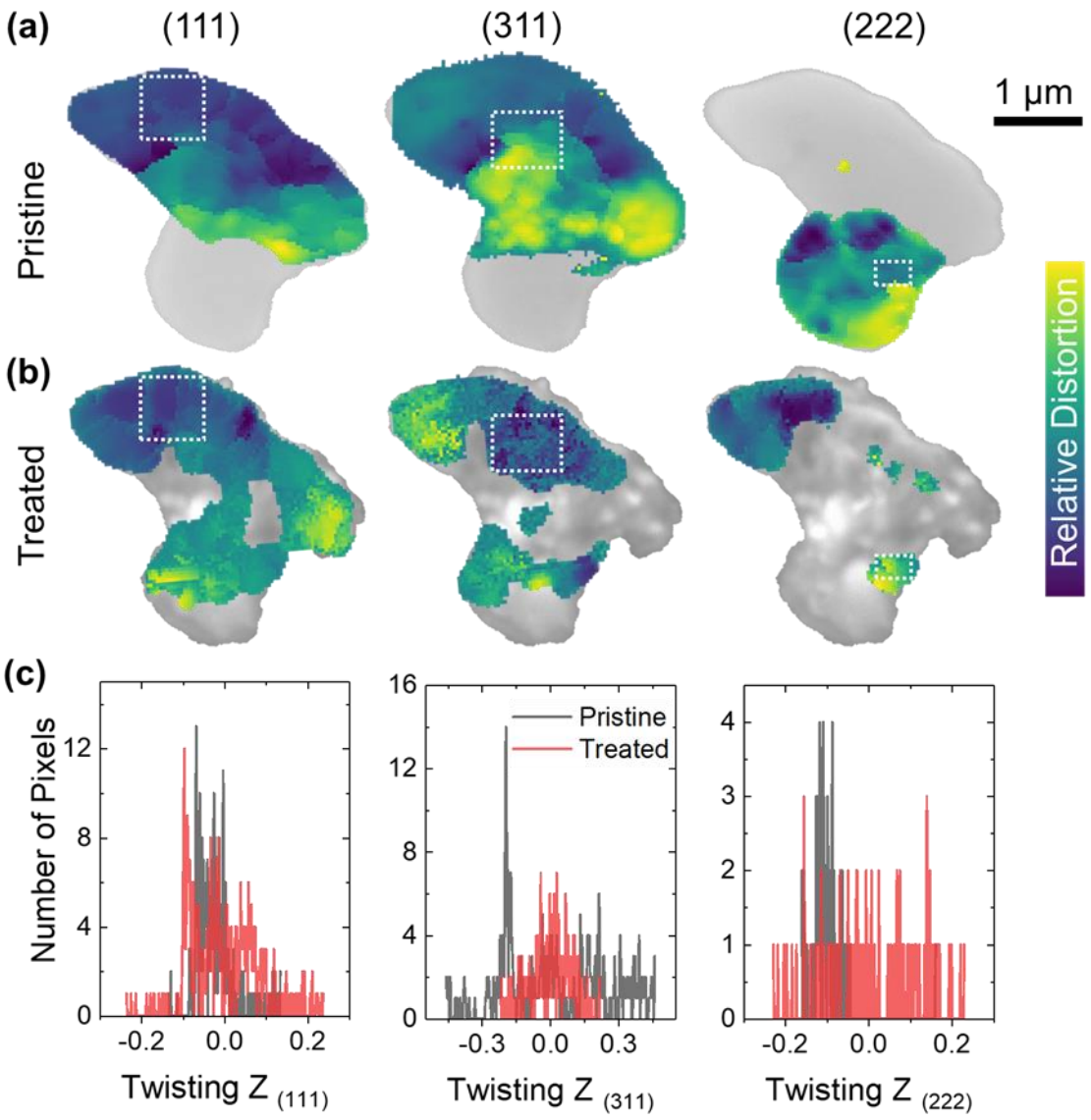

Figure 4-4. Distortion maps of lattice twisting along the *z*-axis, for the **(a)** pristine LNMO particle and **(b)** after chemical delithiation treatment at each Bragg location. The color bar represents the relative distortion intensity where blue is less intense and yellow is more intense. **(c)** Histograms of lattice distortion distributions comparing overlapping regions (in white outline) in pristine and treated maps. Plots are shifted to be centered at 0.0. Pristine maps are adapted with permission.[7] 2022, American Chemical Society.

Microstrain is a significant factor in capacity fading.[30,35] Heterogeneity of lattice distortions in the pristine particle may be caused by the uneven distribution of Mn^{3+} in the as-synthesized material. The larger ionic radius of Mn^{3+}, which is more present in cation disordered local regions, leads to increasing lattice spacing compared to Mn with a higher average oxidation state, as found in fully ordered regions. This allows strain distortion to be used as a proxy to understand the ordered/disordered spinel phase heterogeneity.[7] The pristine plate particle is highly heterogeneous with distinct crystal domains containing slightly different lattice parameters and crystal orientations. Intra-particle phase coexistence during Li^+ removal can lead to large volume change and strain accumulation. The increased Li^+ diffusion kinetics in disordered regions versus ordered regions exacerbate the heterogeneous phase change.[8] A large change in the lattice parameter during phase transformations has also been found to lead to greater Mn dissolution amounts in LNMO.[36] Dissolution processes may also be selective for areas with higher degrees of defects, which are non-uniformly distributed.[37] In the pristine particle, areas with a larger intensity of lattice distortions may therefore experience greater Mn dissolution upon chemical delithiation treatment. Indeed, the severe change of surface features in the particle observed in the SEM images and the breakdown of large crystal grains observed in the nanodiffraction maps may be a result of physical changes in the particle due to transition metal dissolution at domain boundaries. X-ray fluorescence (XRF) spectroscopy measurements taken in the nanodiffraction setup also reveal a decrease in the Mn to Ni ratio in the individual target particle after delithiation treatment, indicating that Mn loss has occurred (**Figure S4-1**). The increasing lattice distortions after chemical delithiation may therefore be attributed to the heterogeneous delithiation, phase transformation, and dissolution processes, but the nanodiffraction measurements, which measure only a single particle, may not be fully representative of each particle in the cathode.

4.3.2. Bulk Chemical Delithiation and Transition Metal Dissolution Behaviors

Mn dissolution is understood to be the largest barrier to the practical application of spinel LMO and LNMO materials. Acidic environments, such as HF generated by electrolyte decomposition can facilitate the Mn disproportionation reaction, as illustrated by **Figure 4-5a**. In the case of chemical delithiation with NO_2BF_4, Li^+ removal follows the reaction illustrated in **Figure 4-5b**, with the presence of trace water leading to transition metal dissolution. Oxygen migration and loss, electrolyte oxidation, and surface rearrangement can lead to additional transition metal loss, while severe particle cracking can accompany chemical treatment. Chemical delithiation of a bulk LNMO powder sample was performed using 40 and 80 mole% of NO_2BF_4 in acetonitrile. SEM images show that the material contains plate-like particles several microns in size, with irregular, nanometer-sized particles decorating the surface. Increasing the percentage of oxidant used led to cracking within the larger particles, as well as decreasing the size of the smaller surface particles (**Figure 4-5c-e**). Energy dispersive X-ray spectroscopy (EDS) reveals a decrease in the Mn to Ni ratio with increasing oxidant percent, indicating Mn loss occurs more prominently, in agreement with the XRF measurement of the individual nanodiffraction particle (**Table S4-1**). X-ray diffraction (XRD) patterns collected on the pristine and chemical delithiated materials (**Figure 4-5f**) show a spinel $Fd\bar{3}m$ structure, with a secondary Li_2MnO_3 impurity phase present in all samples. With increasing oxidant percentage, the spinel (311) Bragg peak shifts to a higher 2θ value, due to a contraction of the lattice during phase change; however, only 1.1% volume change occurs, indicating less than 50% Li removal.

Soft X-ray absorption spectroscopy (sXAS) was used to observe the changes in the oxidation state of Ni and Mn after chemical delithiation treatment. Synchrotron sXAS can directly probe transition metal 2p-3d transitions at the transition metal L-edge. The splitting of the spectra

into two regions, the L_3-edge at lower energy and the L_2-edge at higher energy, is a result of spin-orbital splitting. Detection in the total electron yield (TEY) collection mode can probe the surface-most 2-5 nm of a material, while fluorescence yield (FY) detection can probe up to 50 nm.[38] From **Figure 4-5g**, the Ni L-edge shows slight oxidation with increasing NO_2BF_4 percent, consistent with increasing Li^+ removal. The FY spectra show Ni is slightly more reduced on the surface compared to the bulk/sub-surface. The Mn L-edge spectra show a slight reduction with increasing oxidant, which is more prominent on the surface, as measured by TEY mode (**Figure 4-5h**). Mn reduction can be attributed to the presence of dissolved Mn species redepositing on the particle surface. We can conclude samples have undergone slight chemical delithiation at the surface.

The lattice distortion evolution behavior observed by nanodiffraction in the chemically delithiated LNMO particle may be influenced by our method of Li^+ removal. Lattice contraction, Ni oxidation, and Li^+ removal well replicate the processes that occur during electrochemical cycling. However, the amount of Li removed is limited, while Mn dissolution and severe particle fracturing may be exaggerated due to the strong oxidizing potential of NO_2BF_4 or the method of chemically delithiating a single particle. Therefore, the chemical delithiation method used herein may not fully represent electrochemical processes in spinel materials. Nanodiffraction during *in situ* electrochemical cycling with practical electrolytes is the next step in understanding lattice distortion heterogeneity and evolution in this material.

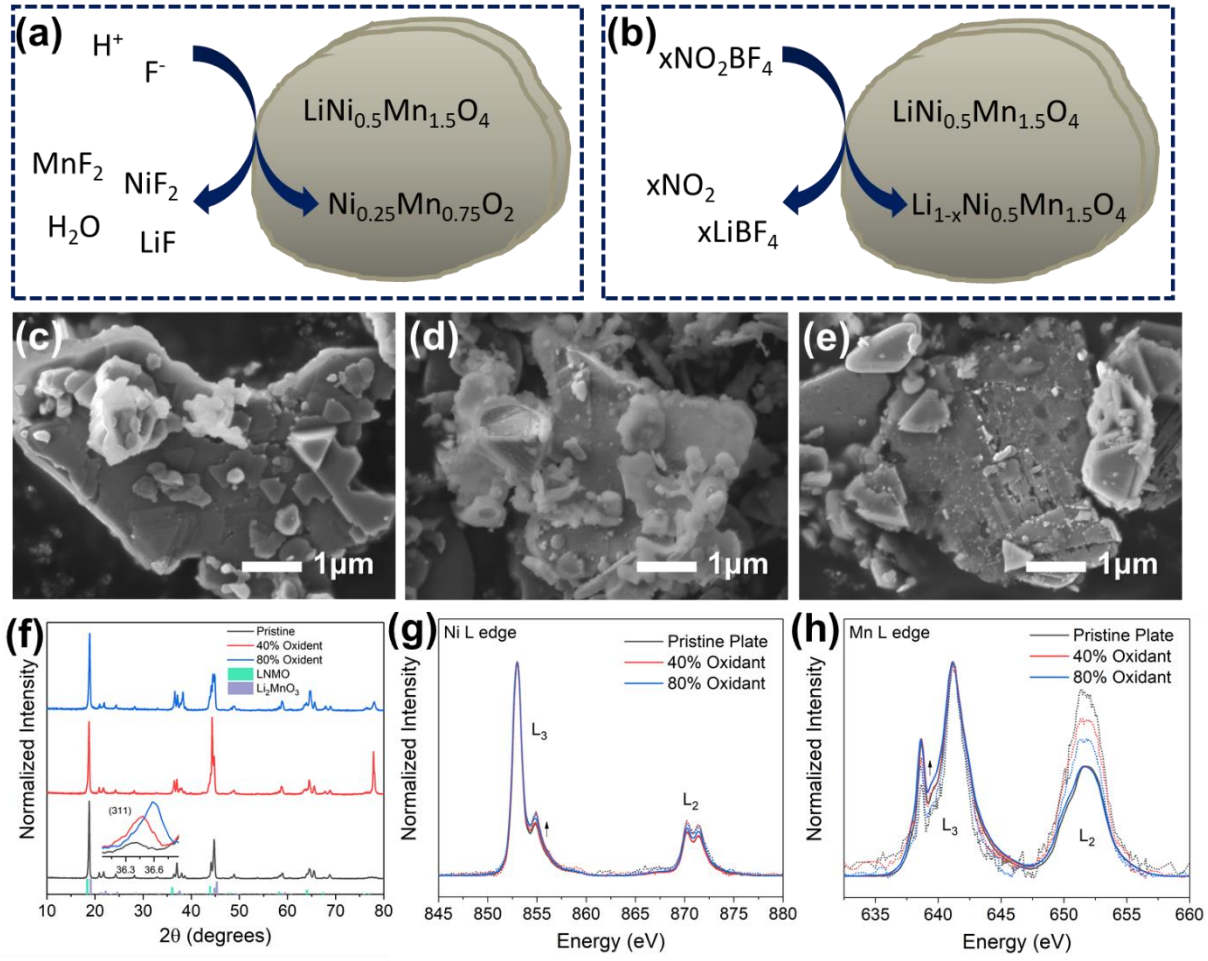

Figure 4-5. (a) Schematic showing the reaction of transition metal dissolution from LNMO in acidic conditions e.g. HF generated from electrolyte decomposition. **(b)** Schematic showing the reaction of chemical Li^+ removal from LNMO by NO_2BF_4 oxidizing agent. SEM images of **(c)** pristine LNMO powder and after reacting with **(d)** 40 % and **(e)** 80 % by mole NO_2BF_4 in acetonitrile. **(f)** XRD patterns. Soft XAS spectra in TEY (solid line) and FY (dotted line) collection modes of **(g)** Ni L-edge and **(h)** Mn L-edge.

4.4. Conclusion

In summary, we have utilized high-resolution nanodiffraction to measure single-crystal plate-like LNMO particles revealing spatially heterogeneous lattice distortions which we hypothesize can be correlated to ordered and disordered spinel phase distributions. Upon chemical delithiation with NO_2BF_4 in acetonitrile, the relative distributions of distortions increased, indicating phase transformations also occur heterogeneously and severe particle transformation including crack formation was observed. Transition metal dissolution and particle cracking phenomena can contribute to the capacity fading of LNMO full cells. The aggressive Li^+ removal during chemical delithiation suggests this method may not always be viable to replicate electrochemical cycling conditions. Ultimately, cathode materials' interactions with electrolytes under practical conditions must be taken into account to fully understand the transition metal dissolution process and degradation of the materials during device operation. Single-crystal LNMO is a green alternative to Co-containing cathodes; however, we rationalize that continued materials optimization to minimize structural heterogeneity and electrolyte engineering to stabilize interphases during high voltage cycling are required for the continued design and commercialization of LIBs containing LNMO cathodes. Identifying and understanding how structural and chemical heterogeneities influence the performance of LIB cathodes upon cycling is vital for developing materials design principles to mitigate degradation. Our work provides an experimental platform utilizing synchrotron X-ray techniques to investigate materials defects upon Li removal.

4.5. Experimental Section

4.5.1. Materials Synthesis

LNMO was prepared via a molten salt synthesis method. Precursors $Ni(NO_3)_2 \cdot 6H_2O$ (Sigma Aldrich) and $Mn(NO_3)_2 \cdot 4H_2O$ (Sigma Aldrich) were dissolved in a minimum amount of deionized water and ground with LiCl salt (Ward's Science) in a 1:30 transition metal to salt mole ratio. The mixture was heated at 750 °C for 8 hours in an air environment, and powders were subsequently washed with deionized water and isopropyl alcohol, and then dried in a 100 °C vacuum oven overnight. Chemical delithiation was performed by stirring the bulk powders in a 0.1 M NO_2BF_4 (ACROS Organics) in acetonitrile (Fisher) solution at room temperature for 24 hours. The material was then washed with acetonitrile and dried overnight. For the delithiated particle for nanodiffraction measurements, the sample holder was immersed in a slowly stirring solution of 0.2 M NO_2BF_4 in acetonitrile solution for 3 hours, then washed with fresh acetonitrile.

4.5.2. Materials Characterization

Morphological images were collected using a JEOL IT-500HR analytical field emission gun scanning electron microscope (SEM) with a 5 kV acceleration voltage. Powder X-ray diffraction (XRD) patterns were acquired on a benchtop Rigaku Miniflex II with a Cu Kα light source (λ = 1.5406 Å), and scanning from 10 to 80 ° 2θ with a step size of 0.02 ° 2θ and a 1.0 s count time. Soft X-ray absorption spectroscopy (sXAS) was performed at beamline 10-1 at Stanford Synchrotron Radiation Lightsource. A ring current of 350 mA and a 1000 L/mm spherical grating monochromator with a 20 μm entrance and exit slit were used to acquire $\sim 10^{11}$ ph/s at a 0.28 eV resolution in a 1 mm^2 beam spot. Data was collected under ultrahigh vacuum (10^{-9} Torr) in a single load at room temperature. Spectra were normalized by the current from freshly

evaporated gold on a fine grid positioned upstream from the main chamber. Nanodiffraction was performed at the Hard X-ray Nanoprobe (HXN) Beamline 3-ID at the National Synchrotron Light Source II. X-rays focused to a ~30 nm spot size were used to illuminate the sample. The sample crystal was rotated to excite a Bragg diffraction. A pixel array detector was oriented to record the diffracted pattern. Raster scans with 50 nm step size were collected for a series of two-degree range rocking angles to produce rocking curves.

4.6. Acknowledgements

The work was supported by the National Science Foundation under Grant No. DMR-1832613. Use of the Stanford Synchrotron Radiation Lightsource, SLAC National Accelerator Laboratory, is supported by the U.S. Department of Energy, Office of Science, Office of Basic Energy Sciences under Contract No. DE-AC02-76SF00515. This research used 3-ID of the National Synchrotron Light Source II, a U.S. Department of Energy (DOE) Office of Science User Facility operated for the DOE Office of Science by Brookhaven National Laboratory under Contract No. DE-SC0012704.

4.7. References

(1) Liu, D.; Zhu, W.; Trottier, J.; Gagnon, C.; Barray, F.; Guerfi, A.; Mauger, A.; Groult, H.; Julien, C. M.; Goodenough, J. B.; Zaghib, K. Spinel Materials for High-Voltage Cathodes in Li-Ion Batteries. *RSC Adv.* **2014**, *4* (1), 154–167.

(2) Li, W.; Cho, Y.-G. G.; Yao, W.; Li, Y.; Cronk, A.; Shimizu, R.; Schroeder, M. A.; Fu, Y.; Zou, F.; Battaglia, V.; Manthiram, A.; Zhang, M.; Meng, Y. S. Enabling High Areal Capacity for Co-Free High Voltage Spinel Materials in next-Generation Li-Ion Batteries. *J. Power Sources* **2020**, *473*, 228579.

(3) Kim, J. H.; Myung, S. T.; Yoon, C. S.; Kang, S. G.; Sun, Y. K. Comparative Study of LiNi0.5Mn1.5O 4-δ and LiNi0.5Mn1.5O4 Cathodes Having Two Crystallographic Structures: Fd3m and P4332. *Chem. Mater.* **2004**, *16* (5), 906–914.

(4) Kim, J. H.; Huq, A.; Chi, M.; Pieczonka, N. P. W.; Lee, E.; Bridges, C. A.; Tessema, M. M.; Manthiram, A.; Persson, K. A.; Powell, B. R. Integrated Nano-Domains of Disordered and Ordered Spinel Phases in LiNi0.5Mn1.5O4 for Li-Ion Batteries. *Chem. Mater.* **2014**, *26* (15), 4377–4386.

(5) Casas-Cabanas, M.; Kim, C.; Rodríguez-Carvajal, J.; Cabana, J. Atomic Defects during Ordering Transitions in LiNi0.5Mn1.5O4 and Their Relationship with Electrochemical Properties. *J. Mater. Chem. A* **2016**, *4* (21), 8255–8262.

(6) Finegan, D. P.; Vamvakeros, A.; Tan, C.; Heenan, T. M. M.; Daemi, S. R.; Seitzman, N.; Di Michiel, M.; Jacques, S.; Beale, A. M.; Brett, D. J. L.; Shearing, P. R.; Smith, K. Spatial Quantification of Dynamic Inter and Intra Particle Crystallographic Heterogeneities within Lithium Ion Electrodes. *Nat. Commun.* **2020**, *11* (1), 631.

(7) Spence, S. L.; Hu, A.; Jiang, M.; Xu, Z.; Yang, Z.; Rahman, M. M.; Li, L.; Chu, Y. S.; Xiao, X.; Huang, X.; Lin, F. Mapping Lattice Distortions in LiNi 0.5 Mn 1.5 O 4 Cathode Materials. *ACS Energy Lett.* **2022**, 690–695.

(8) Yoon, J.; Kim, D.; Um, J. H.; Jeong, M.; Oh, W.; Yoon, W. S. Effect of Local Structural Changes on Rate Capability of LiNi0.5Mn1.5O4-δ Cathode Material for Lithium Ion Batteries. *J. Alloys Compd.* **2016**, *686*, 593–600.

(9) Moorhead-Rosenberg, Z.; Huq, A.; Goodenough, J. B.; Manthiram, A. Electronic and Electrochemical Properties of Li1-XMn1.5Ni0.5O4 Spinel Cathodes As a Function of Lithium Content and Cation Ordering. *Chem. Mater.* **2015**, *27* (20), 6934–6945.

(10) Kuppan, S.; Xu, Y.; Liu, Y.; Chen, G. Phase Transformation Mechanism in Lithium Manganese Nickel Oxide Revealed by Single-Crystal Hard X-Ray Microscopy. *Nat. Commun.* **2017**, *8*, 14309.

(11) Saravanan, K.; Jarry, A.; Kostecki, R.; Chen, G. A Study of Roomerature LixMn1.5Ni0.5O4 Solid Solutions. *Sci. Rep.* **2015**, *5* (1), 8027.

(12) Zheng, J.; Xiao, J.; Yu, X.; Kovarik, L.; Gu, M.; Omenya, F.; Chen, X.; Yang, X. Q.; Liu, J.; Graff, G. L.; Whittingham, M. S.; Zhang, J. G. Enhanced Li + Ion Transport in LiNi 0.5Mn 1.5O 4 through Control of Site Disorder. *Phys. Chem. Chem. Phys.* **2012**, *14* (39), 13515–13521.

(13) Spence, S. L.; Xu, Z.; Sainio, S.; Nordlund, D.; Lin, F. Tuning the Morphology and Electronic Properties of Single-Crystal LiNi 0.5 Mn 1.5 O 4−δ : Exploring the Influence of LiCl–KCl Molten Salt Flux Composition and Synthesis Temperature. *Inorg. Chem.* **2020**, *59*, 10591–10603.

(14) Cabana, J.; Casas-Cabanas, M.; Omenya, F. O.; Chernova, N. A.; Zeng, D.; Whittingham, M. S.; Grey, C. P. Composition-Structure Relationships in the Li-Ion Battery Electrode Material LiNi0.5Mn1.5O4. *Chem. Mater.* **2012**, *24* (15), 2952–2964.

(15) Duncan, H.; Hai, B.; Leskes, M.; Grey, C. P.; Chen, G. Relationships between Mn3+ Content, Structural Ordering, Phase Transformation, and Kinetic Properties in LiNixMn2-XO4 Cathode Materials. *Chem. Mater.* **2014**, *26* (18), 5374–5382.

(16) Greco, G.; Brutti, S.; Vitucci, F. M.; Lombardo, L.; Köntje, M.; Savoini, A.; Paolone, A.; Panero, S. Investigation of the Chemical Disorder of LiNi 0.5 Mn 1.5 O 4 Lattice by Means of Extended X-Ray Absorption Fine Structure Spectroscopy. *J. Phys. Chem. C* **2014**, *118* (46), 26471–26478.

(17) Kunduraci, M.; Al-Sharab, J. F.; Amatucci, G. G. High-Power Nanostructured LiMn2-XNixO4 High-Voltage Lithium-Ion Battery Electrode Materials: Electrochemical Impact of Electronic Conductivity and Morphology. *Chem. Mater.* **2006**, *18* (15), 3585–3592.

(18) Hunter, J. C. Preparation of a New Crystal Form of Manganese Dioxide: λ-MnO2. *J. Solid State Chem.* **1981**, *39* (2), 142–147.

(19) Thackeray, M. M. Manganese Oxides for Rechargeable Lithium Batteries. *Prog. Solid State Chem.* **1997**, *25* (1–2), 1–75.

(20) Gummow, R. J.; de Kock, A.; Thackeray, M. M. Improved Capacity Retention in Rechargeable 4 V Lithium/Lithium-Manganese Oxide (Spinel) Cells. *Solid State Ionics* **1994**, *69* (1), 59–67.

(21) Shilina, Y.; Ziv, B.; Meir, A.; Banerjee, A.; Ruthstein, S.; Luski, S.; Aurbach, D.; Halalay, I. C. Combined Electron Paramagnetic Resonance and Atomic Absorption Spectroscopy/Inductively Coupled Plasma Analysis As Diagnostics for Soluble Manganese Species from Mn-Based Positive Electrode Materials in Li-Ion Cells. *Anal. Chem.* **2016**, *88* (8), 4440–4447.

(22) Benedek, R.; Thackeray, M. M. Reaction Energy for LiMn 2O 4 Spinel Dissolution in Acid. *Electrochem. Solid-State Lett.* **2006**, *9* (6).

(23) Pieczonka, N. P. W.; Liu, Z.; Lu, P.; Olson, K. L.; Moote, J.; Powell, B. R.; Kim, J.-H.

Understanding Transition-Metal Dissolution Behavior in LiNi 0.5 Mn 1.5 O 4 High-Voltage Spinel for Lithium Ion Batteries. *J. Phys. Chem. C* **2013**, 117–15947.

(24) Huang, Y.; Dong, Y.; Li, S.; Lee, J.; Wang, C.; Zhu, Z.; Xue, W.; Li, Y.; Li, J. Lithium Manganese Spinel Cathodes for Lithium-Ion Batteries. *Adv. Energy Mater.* **2020**, 2000997.

(25) Tang, D.; Sun, Y.; Yang, Z.; Ben, L.; Gu, L.; Huang, X. Surface Structure Evolution of LiMn2O4 Cathode Material upon Charge/Discharge. *Chem. Mater.* **2014**, *26* (11), 3535–3543.

(26) Wang, L.-F.; Ou, C.-C.; Striebel, K. A.; Chen, J.-S. Study of Mn Dissolution from LiMn2O4 Spinel Electrodes Using Rotating Ring-Disk Collection Experiments. *J. Electrochem. Soc.* **2003**, *150* (7), A905.

(27) Tian, C.; Xu, Y.; Nordlund, D.; Lin, F.; Liu, J.; Sun, Z.; Liu, Y.; Doeff, M. Charge Heterogeneity and Surface Chemistry in Polycrystalline Cathode Materials. *Joule* **2018**, *2* (3), 464–477.

(28) Augustyn, V.; Manthiram, A. Effects of Chemical versus Electrochemical Delithiation on the Oxygen Evolution Reaction Activity of Nickel-Rich Layered LiMO2. *J. Phys. Chem. Lett.* **2015**, *6* (19), 3787–3791.

(29) Knight, J. C.; Therese, S.; Manthiram, A. Delithiation Mechanisms in Acid of Spinel LiMn 2-x M x O 4 (M = Cr, Fe, Co, and Ni) Cathodes. *J. Electrochem. Soc.* **2015**, *162* (3), 426–431.

(30) Shin, Y.; Manthiram, A. Microstrain and Capacity Fade in Spinel Manganese Oxides. *Electrochem. Solid-State Lett.* **2002**, *5* (3), A55.

(31) Colligan, N.; Augustyn, V.; Manthiram, A. Evidence of Localized Lithium Removal in Layered and Lithiated Spinel Li1-XCoO2($0 \leq x \leq 0.9$) under Oxygen Evolution Reaction Conditions. *J. Phys. Chem. C* **2015**, *119* (5), 2335–2340.

(32) Choi, J.; Alvarez, E.; Arunkumar, T. A.; Manthiram, A. Proton Insertion into Oxide Cathodes during Chemical Delithiation. *Electrochem. Solid-State Lett.* **2006**, *9* (5), A241.

(33) Hai, B.; Shukla, A. K.; Duncan, H.; Chen, G. The Effect of Particle Surface Facets on the Kinetic Properties of LiMn1.5Ni0.5O4 Cathode Materials. *J. Mater. Chem. A* **2013**, *1* (3), 759–769.

(34) Hong, Y. S.; Huang, X.; Wei, C.; Wang, J.; Zhang, J. N.; Yan, H.; Chu, Y. S.; Pianetta, P.; Xiao, R.; Yu, X.; Liu, Y.; Li, H. Hierarchical Defect Engineering for LiCoO2 through Low-Solubility Trace Element Doping. *Chem* **2020**, *6* (10), 2759–2769.

(35) Shin, Y.; Manthiram, A. Influence of the Lattice Parameter Difference between the Two Cubic Phases Formed in the 4 V Region on the Capacity Fading of Spinel Manganese Oxides. *Chem. Mater.* **2003**, *15* (15), 2954–2961.

(36) Choi, W.; Manthiram, A. Comparison of Metal Ion Dissolutions from Lithium Ion Battery

Cathodes. *J. Electrochem. Soc.* **2006**, *153* (9), A1760.

(37) Bozhilov, K. N.; Le, T. T.; Qin, Z.; Terlier, T.; Palčić, A.; Rimer, J. D.; Valtchev, V. Time-Resolved Dissolution Elucidates the Mechanism of Zeolite MFI Crystallization. *Sci. Adv.* **2021**, *7* (25), 454–470.

(38) Lin, F.; Liu, Y.; Yu, X.; Cheng, L.; Singer, A.; Shpyrko, O. G.; Xin, H. L.; Tamura, N.; Tian, C.; Weng, T.-C.; Yang, X.-Q.; Meng, Y. S.; Nordlund, D.; Yang, W.; Doeff, M. M. Synchrotron X-Ray Analytical Techniques for Studying Materials Electrochemistry in Rechargeable Batteries. *Chem. Rev.* **2017**, *117* (21), 13123–13186.

4.8. Supporting Information

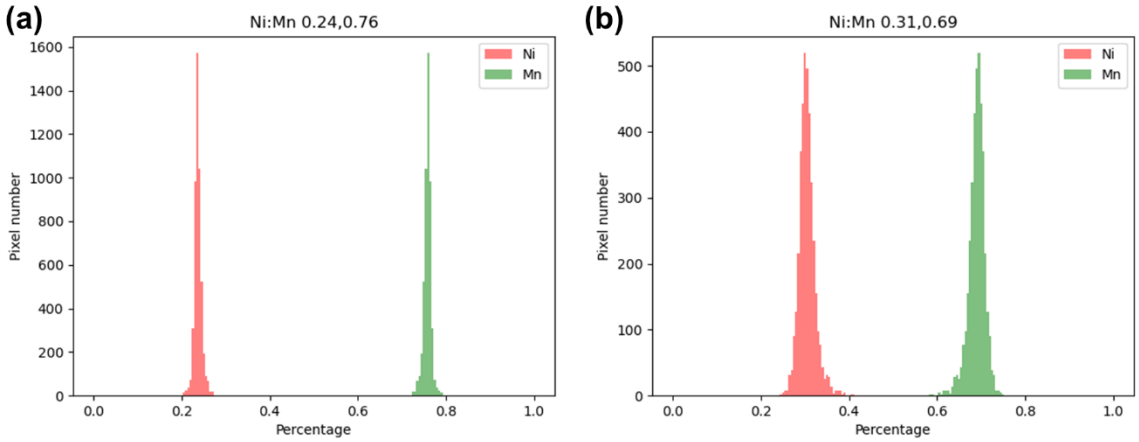

Figure S4-1. Atomic ratios of Ni and Mi in the **(a)** pristine LNMO particle and **(b)** after chemical delithiation treatment measured by X-ray fluorescence spectroscopy.

Table S4-1. Atomic ratios measured by EDS for LNMO powder samples in the pristine state and after chemical delithiation with various percentages of NO_2BF_4 oxidant.

Atomic Ratio	Theoretical	Pristine	40% Oxidant	80% Oxidant
O	**66.6**	**71.6**	**77.6**	**72.9**
Mn	**25.0**	**21.3**	**16.4**	**18.5**
Ni	**8.3**	**7.2**	**6.1**	**8.6**
Mn:Ni	**75:25**	**75:25**	**73:27**	**68:32**

Chapter 5. Visualizing Lattice Distortion Evolution Through *In Situ* Nanodiffraction of Single-Crystal $LiNi_{0.5}Mn_{1.5}O_4$ Cathode Material

Stephanie L. Spence[1], Anika Promi[1], Sami Sainio[2], Dennis Nordlund[2], Xiaojing Huang[3], Feng Lin[1*]*

[1]Department of Chemistry, Virginia Tech, Blacksburg, VA 24061, USA

[2]Stanford Synchrotron Radiation Lightsource, SLAC National Accelerator Laboratory, Menlo Park, CA 94035, USA

[3]National Synchrotron Light Source II, Brookhaven National Laboratory, Upton, NY 11973, USA

5.1. Abstract

The electrochemical properties and cycling performance in Li-ion batteries using high-voltage spinel $LiNi_{0.5}Mn_{1.5}O_4$ (LNMO) cathode material are significantly influenced by both the Ni/Mn ordering and Mn oxidation state of the material, which can vary depending on synthesis conditions and are difficult to discern spatially through traditional lab-based characterization techniques. Furthermore, upon Li removal, heterogeneous phase changes occur, which may hinder Li-ion transport at phase boundaries during battery operation, leading to poor cyclability. Herein, structural distortions in LNMO at different states of charge are spatially mapped at the nano-scale using *in situ* X-ray nanodiffraction. This study develops a platform to visualize dynamic lattice distortion behaviors in high-voltage cathode materials which can help to inform researchers' understanding of cycling degradation mechanisms and to develop strategies to optimize performance. We observe that an LNMO particle with mixed Ni/Mn ordering and a Mn oxidation state of less than 4 exhibits increased heterogeneity of strain upon Li removal, suggesting that inherent structural heterogeneity leads to multi-phase transformation behaviors during cycling at the individual particle scale.

5.2. Introduction

High-voltage spinel materials including $LiNi_{0.5}Mn_{1.5}O_4$ (LNMO) are considered promising cathode materials to address the increasing demands for improved battery performance due to their high operating potential of ~4.7 V versus Li/Li^+ and high energy density of ~650 Wh/kg.[1] These materials are free of the toxic and expensive element cobalt making them of interest for low-cost, green batteries. Renewed research interest in this material, originally discovered in 1997[2,3], is concerned with elucidating fundamental understandings relating to their complex structure and

phase transformation behaviors. LNMO can adopt two crystallographic structures depending on the synthesis conditions: an ordered simple cubic ($P4_332$) and a disordered face-centered cubic ($Fd\bar{3}m$) spinel.[4] The formation of the disordered phase occurs at temperatures at and above 700 °C and is associated with the loss of oxygen from the material lattice, as well as the reduction of a small amount of electrochemically inactive Mn^{4+} to active Mn^{3+} to provide an overall charge compensation.[4–6] These differences in electronic and crystal structure can influence the electrochemical performance of materials where increased structural disorder can lead to solid-solution phase change behavior upon (de)intercalation, resulting in increased Li^+ transport and improved rate performances.[7–10] The presence of Mn^{3+} is also linked to Mn dissolution that occurs in spinel oxide materials, leading to loss of active material and capacity fading, and is a major barrier to the commercialization of LNMO.[11–13]

The relationship between structural ordering and Mn^{3+} content is critical to the understanding of the intrinsic chemomechanical and electrochemical properties of LNMO. Particles can contain heterogeneously distributed local regions of both ordered and disordered phases, which can create internal anti-phase boundaries, hindering ion transport.[14,15] Additionally, upon Li removal, cubic phase transformations can occur heterogeneously leading to two or three phase coexistence at the inter- and intra- particle levels.[16,17] Large-scale heterogeneities can lead to strain accumulation and asynchronous cycling behaviors resulting in degradation and, ultimately, battery failure.[18] The lattice distortion within particles, influenced by the changes in Mn ionic radii with changing oxidation state change, can be used as a proxy for understanding intrinsic and dynamic phase heterogeneity.[19] Elucidating the origins of such heterogeneities has been an important area of study in LNMO materials[14,17,19] and can help researchers develop strategies to mitigate chemomechanical failures such as optimizing phase distribution during

synthesis or with post-synthesis treatments.[20] Heterogeneity has been measured by *ex situ* and *in situ* XRD studies however, such methods typically lack high spatial resolution.

To investigate the extent and heterogeneity of structural defects and lattice distortions at the individual particle scale, herein, we have employed a high-spatial-resolution, synchrotron X-ray nanodiffraction technique and developed a method to measure LNMO samples prepared under various synthesis conditions and at different degrees of Li removal. This technique can help us to spatially visualize how lattice distortions evolve in LNMO particles during Li (de)intercalation, or at different states of charge (SOC). Correlating lattice strain and the degree of Li removal can also reveal fundamental mechanisms of phase change in LNMO materials. We hypothesize that the lattice distortions and internal strain should coincide with spinel ordered and disordered phase heterogeneity due to (1) the larger ionic radius of Mn^{3+} compared to Mn^{4+} leading to lattice expansion inherent in the more disordered material at the pristine state, and (2) differing rates and mechanism of phase change in disordered and ordered regimes during Li removal upon charging. A greater degree of heterogeneous phase regions present in both the inherent structure and evolved under dynamic conditions can negatively affect battery-cycling stability due to increased phase boundaries limiting Li transport and increasing internal strain.

5.3. Results and Discussion

5.3.1. Materials Properties of Octahedral LNMO with Different Mn^{3+} Contents

LNMO powders were synthesized via a tunable molten salt method at 650 or 750 °C, resulting in ~500 nm sized well-defined octahedral particles (**Figure 5-1a** and **b**). From the XRD patterns (**Figure 5-1c**), both samples show good crystallinity for the $Fd\bar{3}m$ disordered spinel structure with minimal impurity phases. The sample prepared at 750 °C shows a slight shift of

Bragg peaks to lower angles compared to the 650 °C calcination, indicating a larger *d*-spacing of the lattice to accommodate the presence of more Mn in a reduced 3+ oxidation state, which coincides with previous results.[21] Coin cells were prepared and cycled from 3.5 to 4.9 V vs Li/Li^+. The voltage profile can be used to estimate the amount of electrochemically active Mn^{3+} present in LNMO materials by calculating the percentage of total capacity obtained from the Mn^{3+}/Mn^{4+} redox plateau occurring at ~4.0 V. **Figure 5-1d** and **e** show the charge and discharge voltage profiles for the 650 and 750 °C samples, which give 5.7% and 22.3% active Mn^{3+}, and 102.3 and 43.4 mAh/g specific capacities in the first discharge, respectively. The larger capacity of the 650 °C sample can be attributed to the optimal Mn^{3+} content minimizing secondary phases and structural distortions.[19,21] Both materials experience an activation period over the first ~15 cycles caused by the changes in surface structure, electrolyte decomposition, and solid-electrolyte interphase (SEI) formation during the initial cycling, which leads to a slight increase in discharge capacity and Columbic efficiency (**Figure 5-1f**).[22] Utilizing the molten salt method allows for facile tuning of the electronic properties, while keeping particle morphology and size consistent.

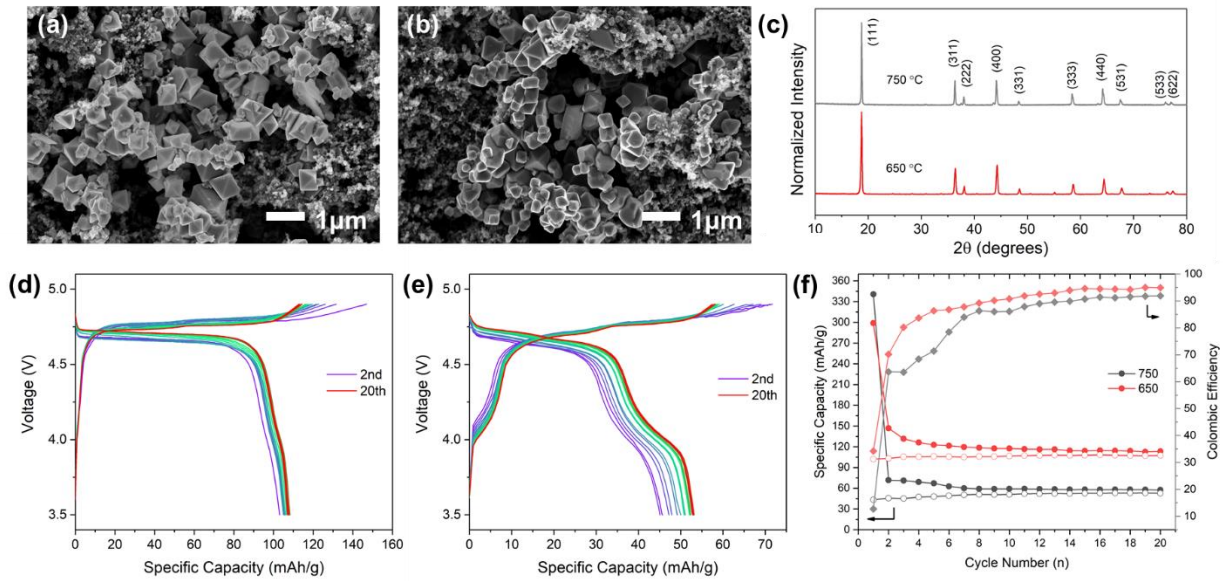

Figure 5-1. SEM images of LNMO powders synthesized at **(a)** 650 °C and **(b)** 750 °C. **(c)** XRD patterns. Voltage profiles of coin cells prepared with LNMO powders synthesized at **(d)** 650 °C and **(e)** 750 °C. **(f)** Cycling performance and Columbic efficiency. Cells were cycled from 3.5 to 4.9 V vs Li/Li^+ at C/3.

To further investigate changes in the oxidation state of the materials, soft X-ray absorption spectroscopy (XAS) measurements were performed on the electrodes in the pristine state and at 4.7 V, where materials are approximately 50% charged. XAS is surface sensitive to transition metal 2p to 3d transitions at the metal L-edge and oxygen 1s to 2p transitions at the O K-edge to probe unoccupied states.[23,24] From the total electron yield (TEY) detection mode, we can obtain information about the top surface 2-5 nm of the material, while the fluorescence yield (FY) gives sub-surface information from up to 50 nm. For both LNMO samples, the Ni L-edges remain unchanged from the pristine state to charged, indicating deep delithiation and Ni redox was not yet reached at the beginning of the 4.7 V plateau (**Figure 5-2a** and **b**). In the pristine state, the 750 °C sample contains slightly more reduced Mn than the 650 °C sample, consistent with previous

measurements for LNMO prepared at higher temperatures.[21] At 4.7 V, Mn shows a significant reduction for the 650 °C sample and a slight reduction for the 750 °C sample (**Figure 5-2c** and **d**). This is contradictory to the transition metal oxidation we would expect to observe during Li removal; however, increasing Mn^{2+} and Mn^{3+} contributions may be due to the presence of dissolved Mn species redepositing on the surface of the electrodes after charging to high voltages.[25,26] The O K-edge is consistent with a decreasing intensity ratio of the lower-energy and higher-energy pre-edge peaks going from pristine to partially charged samples (**Figure 5-2e** and **f**). The soft XAS results suggest that mixed Mn^{4+} and Mn^{3+} are present in the pristine samples and that Mn dissolution and re-deposition are severe upon charging.

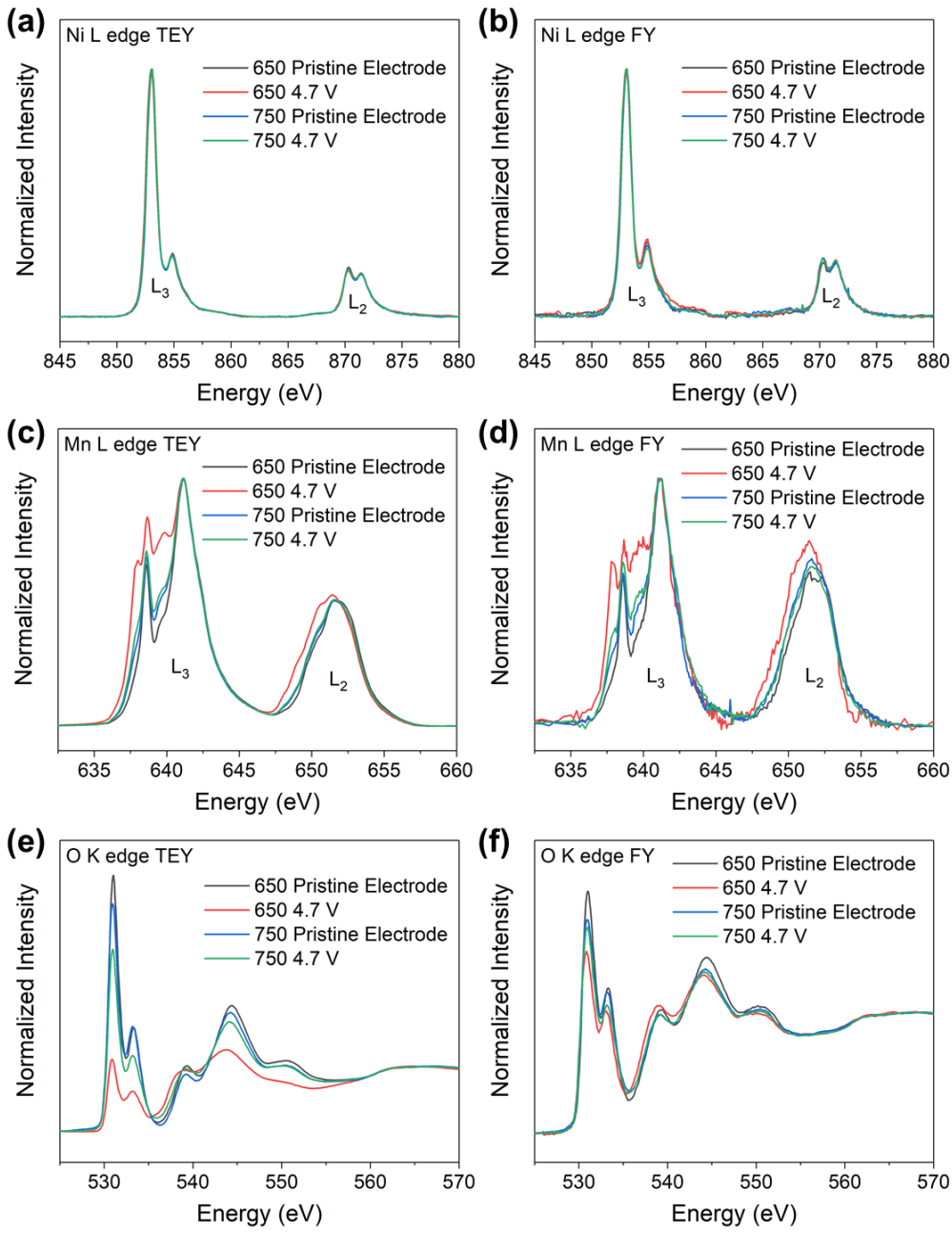

Figure 5-2. Soft XAS spectra of LNMO powders synthesized at 650 °C and 750 °C in the pristine state and at 4.7 V. Ni L-edge in **(a)** TEY (2-5 nm) and **(b)** FY (up to 50 nm) data collection modes. Mn L-edge in **(c)** TEY (2-5 nm) and **(d)** FY (up to 50 nm) data collection modes. O K-edge in **(e)** TEY (2-5 nm) and **(f)** FY (up to 50 nm) data collection modes.

5.3.2. *In Situ* Nanodiffraction Measurements

Electrochemical cycling, lab-based X-ray diffraction, and soft XAS techniques all provide ensemble-averaged bulk information about materials samples and cannot distinguish the local structural and chemical heterogeneities, which may arise at the micro or nanoscale. Herein, we turn to high-spatial-resolution X-ray synchrotron nanodiffraction using the Hard X-ray Nanoprobe (HXN) to spatially map lattice distortion variations within individual particles. Measurements performed in an *in situ* setup can provide information about strain evolution during electrochemical cycling. **Figure 5-3** shows an illustrated schematic and photograph images of the *in situ* nanodiffraction electrochemical cell design and measurements. In this technique, X-rays are focused to a spot size of ~30 nm and diffraction signal is collected at a Bragg angle of interest.[27] The sample is rotated near the Bragg angle, which was selected as the (311) peak in this study, while raster scanning is performed to produce rocking curve images across a two degree range. Beam damage to the sample is minimized by performing on-the-fly scan mode measurements. The 3D diffraction pattern can then be broken up into three orthogonal directions corresponding to *d*-spacing change ($\Delta d/d$) or strain, *y*-axis bending, and *z*-axis twisting. Spatial maps of the individual lattice distortions are then used to visualize structural heterogeneity for the sample particles at different SOC with 50 x 50 nm^2 resolution.

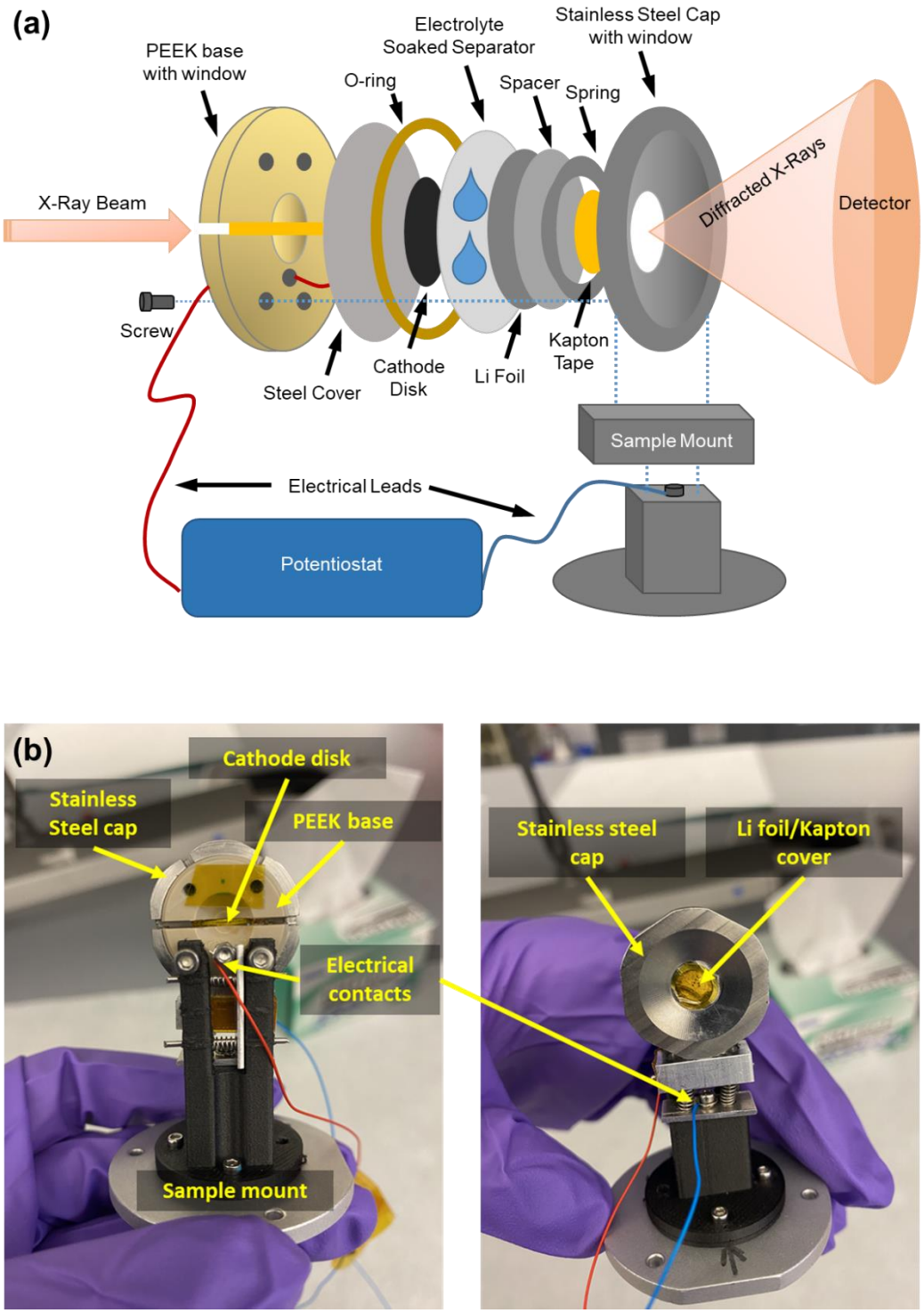

Figure 5-3. (a) Schematic and **(b)** photographs of *in situ* nanodiffraction cell design for the Hard X-ray Nanoprobe.

The electrochemical data for the *in situ* cycling of the 750 °C sample is shown in **Figure 5-4a** illustrating where along the cycling process the nanodiffraction measurements were performed. A target particle with a size of ~8 μm was identified and tracked. A pristine nanodiffraction measurement was performed on the particle before charging. After a formation cycle, the cell was cycled at a rate of C/3 and held at 4.7 and 4.9 V during charging and 3.5 V during discharging for nanodiffraction measurements. The lattice distortion maps show the progression of the strain intensity during the cycling process (**Figure 5-4b**). Histograms of the total strain distribution are plotted in **Figure 5-4c** where the peak widths correspond to overall heterogeneity. Heterogeneous strain is observed in the pristine particle containing about ~22% of electrochemically active Mn^{3+}, based on previous calculations, with a larger distortion intensity concentrated toward the interior of the particle. Structural defects can be identified by the abrupt changes in distortion intensity. Additionally, two distinct peaks present in the histogram suggest local domains with different *d*-spacings representing cation ordered and disordered phases are likely present. Upon charging to 4.7 V, the relative distortion becomes slightly more homogeneous as bulk electrochemically active Mn is oxidized at ~4.0 V. However, the two-phase transformation occurs concurrently producing up to a ~6.3% volume change[16,28], and at 4.9 V, the distortion map shows larger relative strain toward the particle interior. The histogram shows the strain is reduced overall at the fully charged state as delithiation shifts the *d*-spacing to lower values, but tailing of the distribution curve may indicate solid-solution phase change behavior propagating toward the particle interior as evidenced by the spatial map. The discharged state shows an overall increase in strain as transition metals are subsequently reduced. It should be noted that the particle position shifts between measurements, and due to the geometry of the *in situ* cell limiting the angular range of observation, only portions of the particle are observed in the later nanodiffraction

measurements. Furthermore, in electrode materials, heterogeneities are found to occur between particles, which can show different degrees of electrochemical activity.[17] The nanodiffraction measurements are limited to single particle measurements which do not allow for statistical analysis.

The bending *y*-axis and twisting *z*-axis nanodiffraction maps provide information on the out-of-plane distortions of the particle in the *y* and *z* planes, respectively. From the maps and sharp peaks of the histogram in **Figure 5-5a** and **c**, the particle shows minimal *y*-bending distortions. The absolute values of the bending distortion shift as the particle changes orientation slightly between measurements. The twisting in the *z*-axis shows a gradient in the relative distortion across the particle in the pristine state and several distinct peaks in the histogram, indicating the presence of multiple domains with different *z* orientations (**Figure 5-5b** and **d**). Upon charging, the gradient remains, and abrupt changes in the relative distortion values are observed, coinciding with structural defects that are inherent to the particle. Overall, the bending *y*-axis and twisting *z*-axis lattice distortions do not evolve spatially as significantly as the stain, but indicate the particle undergoes chemomechanical changes during charging/discharging.

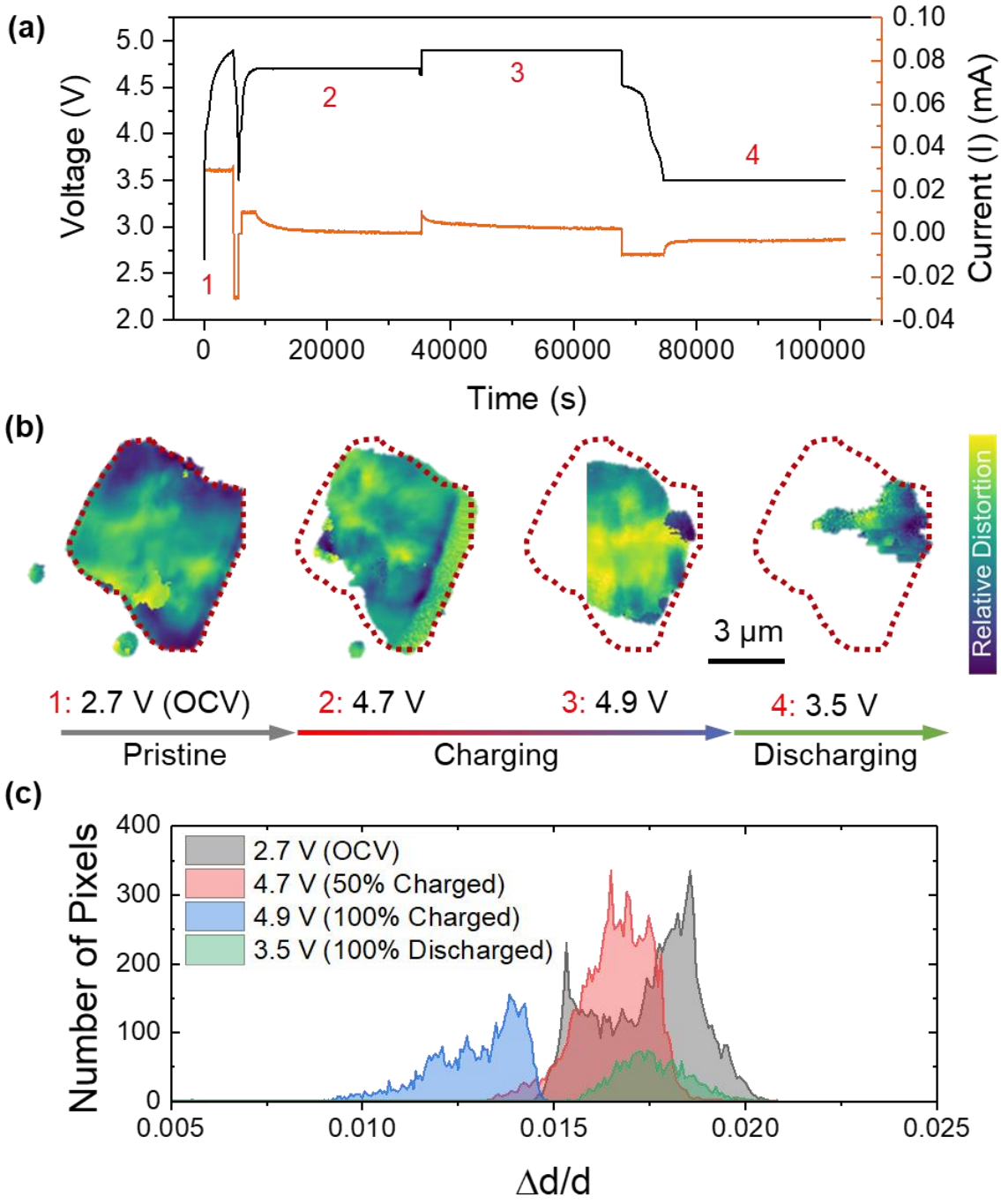

Figure 5-4. (a) *In situ* cycling data for the LNMO sample prepared at 750 °C. Points where nanodiffraction measurements were performed are labeled. The sample was cycled at C/3 from 3.5 to 4.9 V. **(b)** Strain lattice distortion maps at the (311) Bragg position at different SOC. **(c)** Strain variation histograms based on pixel intensity analysis.

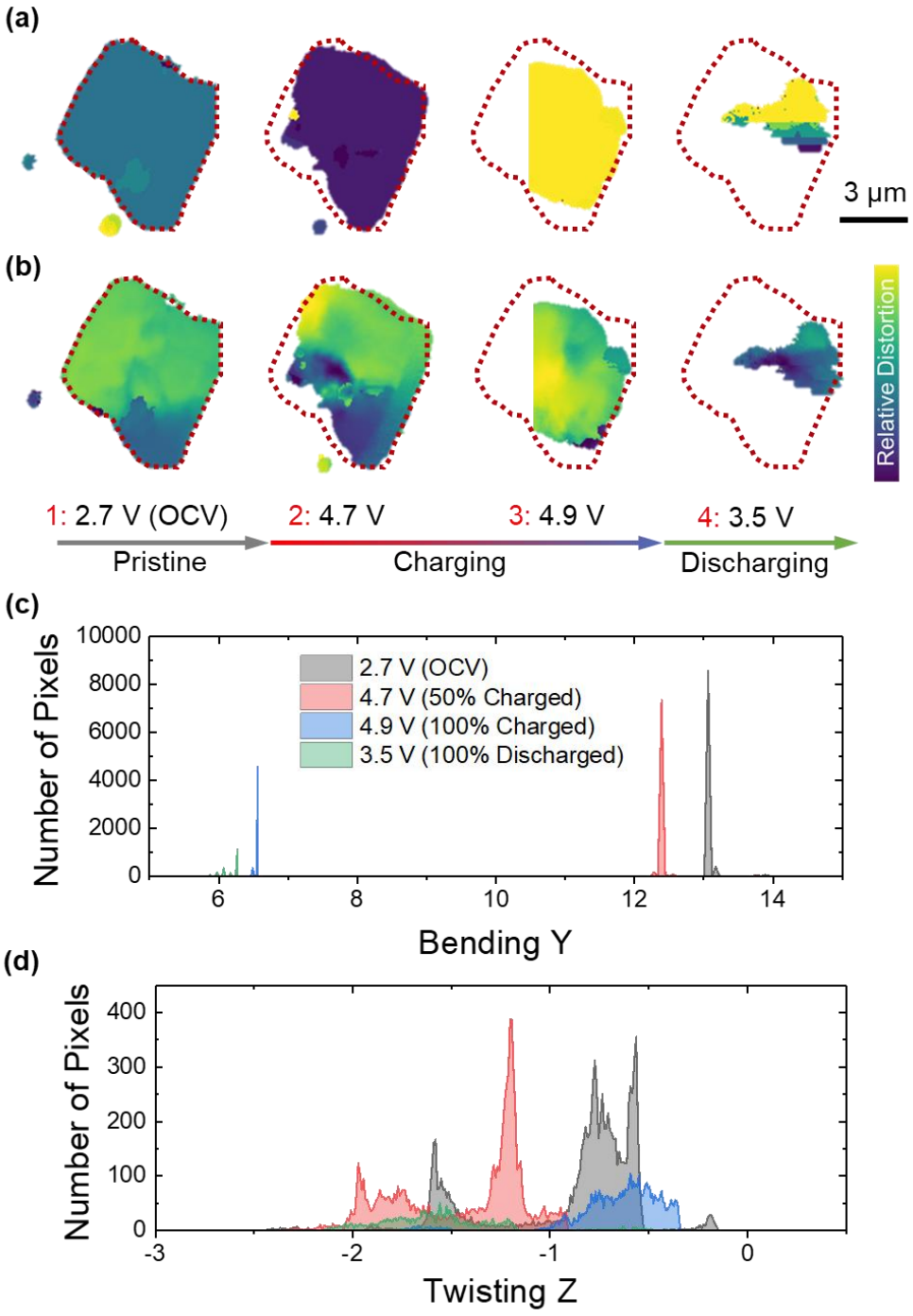

Figure 5-5. (a) Bending *y*-axis and **(b)** twisting *z*-axis lattice distortion maps at the (311) Bragg position for the LNMO sample prepared at 750 °C at different SOC. **(c)** Bending *y*-axis and **(d)** twisting *z*-axis variation histograms based on pixel intensity analysis.

For the sample prepared at 650 °C, a stable representative particle could not be identified for repeat nanodiffraction measurements. A cluster of nanometer-sized particles was measured after the final discharge and during an additional charging process; however, the low capacity obtained suggests that the cell may have shorted before holding at the desired voltages. Nevertheless, the *in situ* strain mapping (**Figure 5-6**) follows a similar trend to the 750 °C particle with increased heterogeneity and peak skewing (rightmost peaks) in the charged state compared to the discharged state. The bending *y*-axis and twisting *z*-axis distortions show severe distortions due to variations in orientation and phase distribution between and within the many particles measured (**Figure 5-7**).

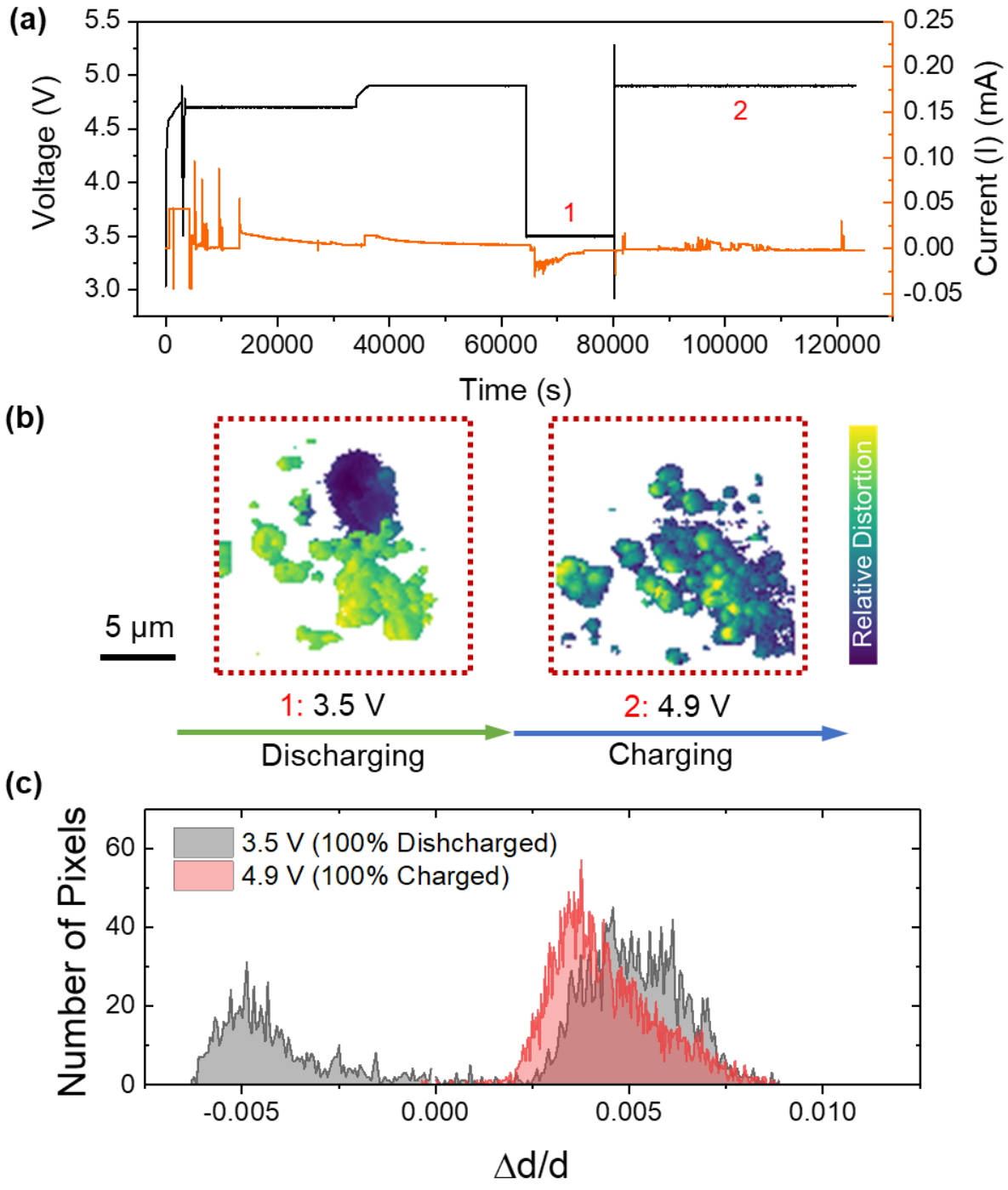

Figure 5-6. (a) *In situ* cycling data curves for the LNMO sample prepared at 650 °C. Points where nanodiffraction measurements were performed are labeled. The sample was cycled at C/3 from 3.5 to 4.9 V. **(b)** Strain lattice distortion maps at the (311) Bragg position at different SOC. **(c)** Lattice distortion variation histograms based on pixel intensity analysis.

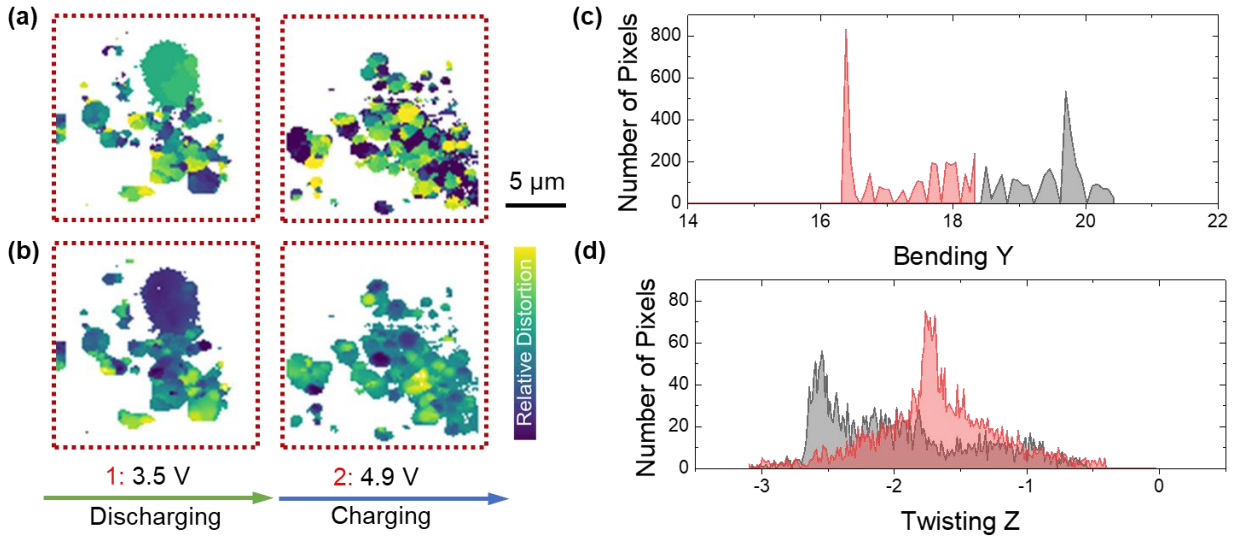

Figure 5-7. (a) Bending *y*-axis and **(b)** twisting *z*-axis lattice distortion maps at the (311) Bragg position for the LNMO sample prepared at 650 °C at different SOC. **(c)** Bending *y*-axis and **(d)** twisting *z*-axis variation histograms based on pixel intensity analysis.

The *in situ* nanodiffraction mappings provide information on lattice parameter variation, which we can use as a proxy for evaluating cation disordering or Mn^{3+} distribution in the pristine state. The large heterogeneity observed suggests the presence of ordered and disordered phase local domains are inherent in the particles after synthesis. Upon Li (de)intercalation, we monitor distortion changes to provide insight into cubic phase transformation behaviors. The strain first contracts heterogeneously and then enlarges upon electrochemical Li removal, suggesting dynamic phase change behaviors or different mechanisms of Li removal. These finding support the multi-phase transformation mechanism of LNMO which can induce large strain within micrometer, single particles.

5.4. Conclusions

The complex properties of high-voltage LNMO cathode material including cation ordering and transition metal oxidation state and their influence on electrochemical cycling behaviors have led to significant research interests. Herein, we design experiments utilizing high-resolution nanodiffraction techniques using *in situ* measurements to spatially visualize structural defects and lattice distortions in LNMO at different states of charge. We observe significant inherent strain heterogeneity in the globally disordered sample synthesized at 750 °C. Synthesis at 650 °C results in minimal electrochemically active Mn^{3+} content (5.7%) but the strain was still heterogeneous between and within particles. Upon Li removal, stain evolution is not linear, suggesting severe structural and phase transformation heterogeneities which can present barriers to complete delithiation. Insights relating the structural and chemical properties and electrochemical performance of LNMO can aid our understanding of materials degradation and capacity fading mechanisms and are crucial for continuing studies in the rational design of cathode materials for high-energy Li-ion batteries. Combined with characterization techniques at different length scales, nanodiffraction studies can be developed for further *ex situ* or *in situ* experiments to provide multi-modal diagnostic capabilities.

5.5. Experimental Section

5.5.1. Materials Synthesis

LNMO powders were prepared by the molten salt synthesis method using $Ni(NO_3)_2 \cdot 6H_2O$ and $Mn(NO_3)_2 \cdot 4H_2O$ precursors dissolved in deionized water and mixed in a mortar and pestle with eutectic LiCl and KCl salts. The ratio of precursors to salts was 1: 30. The mixture was heated in a box furnace at 650 or 750 °C for 8 hours and allowed to cool naturally. The powders were

then washed with deionized water and isopropyl alcohol to remove excess salt, then dried at 100 °C in a vacuum oven overnight. Electrodes were formed by mixing 80% active material, 10% carbon black, and 10% polyvinylidene fluoride (PVDF) binder with N-methylpyrrolidone (NMP). A ratio of 40% active material, 30% carbon black, and 30% PVDF was used to prepare electrodes for HXN measurements (~0.2 mg/cm^2 loading). A doctor blade was used to cast the slurry onto carbon coated aluminum foil. Electrode disks were cut and dried at 120 °C overnight. For cycled electrode measurements, cells were disassembled and electrodes were received in an Ar-filled glovebox and sealed in Kapton tape.

5.5.2. Electrochemical Measurements

Coin cells were assembled using CR2032-type parts, Li foil anodes, Celgard 2400 separators, and 1M $LiPF_6$ in 3:7 vol% ethylene carbonate (EC): dimethyl carbonate (DMC) electrolyte. Coin cells were cycled between 3.5 and 4.9 V vs Li/Li$^+$ at room temperature.

5.5.3. Materials Characterization

SEM images were collected on a LEO FESEM at an acceleration voltage of 5.0 kV. Soft XAS was performed at beamline 10-1 at Stanford Synchrotron Radiation Lightsource. A ring current of 350 mA and a 1000 L/mm spherical grating monochromator with a 20 μm entrance and exit slit were used to acquire ~10^{11} ph/s at a 0.28 eV resolution in a 1 mm^2 beam spot. Data was collected under ultrahigh vacuum (10^{-9} Torr) in a single load at room temperature. Spectra were normalized by the current from freshly evaporated gold on a fine grid positioned upstream from the main chamber. Nanodiffraction was performed at Beamline 3-ID, Hard X-ray Nanoprobe (HXN) in the National Synchrotron Light Source II at Brookhaven National Laboratory. The *in*

situ measurements were performed using a custom *in situ* cell assembly. The galvanostatic charge and discharge measurements were performed using an electrochemical workstation (BioLogic potentiostat). X-rays focused to a ~30 nm spot size were used to illuminate the sample. The sample crystal was rotated to excite a Bragg diffraction. A pixel array detector was oriented to record the diffracted pattern. Raster scans with 50 nm step size were collected for a series of two-degree range rocking angles to produce rocking curves.

5.6. Acknowledgements

The work was supported by the National Science Foundation under Grant No. DMR-1832613. Use of the Stanford Synchrotron Radiation Lightsource, SLAC National Accelerator Laboratory, is supported by the U.S. Department of Energy, Office of Science, Office of Basic Energy Sciences under Contract No. DE-AC02-76SF00515. This research used 3-ID of the National Synchrotron Light Source II, a U.S. Department of Energy (DOE) Office of Science User Facility operated for the DOE Office of Science by Brookhaven National Laboratory under Contract No. DE-SC0012704.

5.7. References

(1) Liu, D.; Zhu, W.; Trottier, J.; Gagnon, C.; Barray, F.; Guerfi, A.; Mauger, A.; Groult, H.; Julien, C. M.; Goodenough, J. B.; Zaghib, K. Spinel Materials for High-Voltage Cathodes in Li-Ion Batteries. *RSC Adv.* **2014**, *4* (1), 154–167.

(2) Zhong, Q.; Bonakdarpour, A.; Zhang, M.; Gao, Y.; Dahn, J. R. Synthesis and Electrochemistry of LiNi x Mn2 − x O 4. *J. Electrochem. Soc.* **1997**, *144* (1), 205–213.

(3) Amine, K.; Tukamoto, H.; Yasuda, H.; Fujita, Y. Preparation and Electrochemical Investigation of LiMn2 − XMexO4 (Me: Ni, Fe, and x = 0.5, 1) Cathode Materials for Secondary Lithium Batteries. *J. Power Sources* **1997**, *68* (2), 604–608.

(4) Kim, J. H.; Myung, S. T.; Yoon, C. S.; Kang, S. G.; Sun, Y. K. Comparative Study of LiNi0.5Mn1.5O 4-δ and LiNi0.5Mn1.5O4 Cathodes Having Two Crystallographic Structures: Fd3m and P4332. *Chem. Mater.* **2004**, *16* (5), 906–914.

(5) Kunduraci, M.; Al-Sharab, J. F.; Amatucci, G. G. High-Power Nanostructured LiMn2-XNixO4 High-Voltage Lithium-Ion Battery Electrode Materials: Electrochemical Impact of Electronic Conductivity and Morphology. *Chem. Mater.* **2006**, *18* (15), 3585–3592.

(6) Kim, S.; Hegde, V. I.; Yao, Z.; Lu, Z.; Amsler, M.; He, J.; Hao, S.; Croy, J. R.; Lee, E.; Thackeray, M. M.; Wolverton, C. First-Principles Study of Lithium Cobalt Spinel Oxides: Correlating Structure and Electrochemistry. *ACS Appl. Mater. Interfaces* **2018**, *10* (16), 13479–13490.

(7) Duncan, H.; Hai, B.; Leskes, M.; Grey, C. P.; Chen, G. Relationships between Mn3+ Content, Structural Ordering, Phase Transformation, and Kinetic Properties in LiNixMn2-XO4 Cathode Materials. *Chem. Mater.* **2014**, *26* (18), 5374–5382.

(8) Moorhead-Rosenberg, Z.; Huq, A.; Goodenough, J. B.; Manthiram, A. Electronic and Electrochemical Properties of Li1-XMn1.5Ni0.5O4 Spinel Cathodes As a Function of Lithium Content and Cation Ordering. *Chem. Mater.* **2015**, *27* (20), 6934–6945.

(9) Yoon, J.; Kim, D.; Um, J. H.; Jeong, M.; Oh, W.; Yoon, W. S. Effect of Local Structural Changes on Rate Capability of LiNi0.5Mn1.5O4-δ Cathode Material for Lithium Ion Batteries. *J. Alloys Compd.* **2016**, *686*, 593–600.

(10) Zheng, J.; Xiao, J.; Yu, X.; Kovarik, L.; Gu, M.; Omenya, F.; Chen, X.; Yang, X. Q.; Liu, J.; Graff, G. L.; Whittingham, M. S.; Zhang, J. G. Enhanced Li + Ion Transport in LiNi 0.5Mn 1.5O 4 through Control of Site Disorder. *Phys. Chem. Chem. Phys.* **2012**, *14* (39), 13515–13521.

(11) Hunter, J. C. Preparation of a New Crystal Form of Manganese Dioxide: λ-MnO2. *J. Solid State Chem.* **1981**, *39* (2), 142–147.

(12) Thackeray, M. M. Manganese Oxides for Rechargeable Lithium Batteries. *Prog. Solid State Chem.* **1997**, *25* (1–2), 1–75.

(13) Gummow, R. J.; de Kock, A.; Thackeray, M. M. Improved Capacity Retention in Rechargeable 4 V Lithium/Lithium-Manganese Oxide (Spinel) Cells. *Solid State Ionics* **1994**, *69* (1), 59–67.

(14) Kim, J. H.; Huq, A.; Chi, M.; Pieczonka, N. P. W.; Lee, E.; Bridges, C. A.; Tessema, M.

M.; Manthiram, A.; Persson, K. A.; Powell, B. R. Integrated Nano-Domains of Disordered and Ordered Spinel Phases in LiNi0.5Mn1.5O4 for Li-Ion Batteries. *Chem. Mater.* **2014**, *26* (15), 4377–4386.

(15) Casas-Cabanas, M.; Kim, C.; Rodríguez-Carvajal, J.; Cabana, J. Atomic Defects during Ordering Transitions in LiNi0.5Mn1.5O4 and Their Relationship with Electrochemical Properties. *J. Mater. Chem. A* **2016**, *4* (21), 8255–8262.

(16) Kuppan, S.; Xu, Y.; Liu, Y.; Chen, G. Phase Transformation Mechanism in Lithium Manganese Nickel Oxide Revealed by Single-Crystal Hard X-Ray Microscopy. *Nat. Commun.* **2017**, *8*, 14309.

(17) Finegan, D. P.; Vamvakeros, A.; Tan, C.; Heenan, T. M. M.; Daemi, S. R.; Seitzman, N.; Di Michiel, M.; Jacques, S.; Beale, A. M.; Brett, D. J. L.; Shearing, P. R.; Smith, K. Spatial Quantification of Dynamic Inter and Intra Particle Crystallographic Heterogeneities within Lithium Ion Electrodes. *Nat. Commun.* **2020**, *11* (1), 631.

(18) Li, J.; Sharma, N.; Jiang, Z.; Yang, Y.; Monaco, F.; Xu, Z.; Hou, D.; Ratner, D.; Pianetta, P.; Cloetens, P.; Lin, F.; Zhao, K.; Liu, Y. Dynamics of Particle Network in Composite Battery Cathodes. *Science (80-.).* **2022**, *376* (6592), 517–521.

(19) Spence, S. L.; Hu, A.; Jiang, M.; Xu, Z.; Yang, Z.; Rahman, M. M.; Li, L.; Chu, Y. S.; Xiao, X.; Huang, X.; Lin, F. Mapping Lattice Distortions in LiNi 0.5 Mn 1.5 O 4 Cathode Materials. *ACS Energy Lett.* **2022**, 690–695.

(20) Sun, H.; Hu, A.; Spence, S.; Kuai, C.; Hou, D.; Mu, L.; Liu, J.; Li, L.; Sun, C.; Sainio, S.; Nordlund, D.; Luo, W.; Huang, Y.; Lin, F. Tailoring Disordered/Ordered Phases to Revisit the Degradation Mechanism of High-Voltage LiNi0.5Mn1.5O4 Spinel Cathode Materials. *Adv. Funct. Mater.* **2022**, 2112279.

(21) Spence, S. L.; Xu, Z.; Sainio, S.; Nordlund, D.; Lin, F. Tuning the Morphology and Electronic Properties of Single-Crystal LiNi 0.5 Mn 1.5 O 4−δ : Exploring the Influence of LiCl–KCl Molten Salt Flux Composition and Synthesis Temperature. *Inorg. Chem.* **2020**, *59*, 10591–10603.

(22) Zhou, J.; Hong, D.; Wang, J.; Hu, Y.; Xie, X.; Fang, H. Electronic Structure Variation of the Surface and Bulk of a LiNi 0.5Mn1.5O4 Cathode as a Function of State of Charge: X-Ray Absorption Spectroscopic Study. *Phys. Chem. Chem. Phys.* **2014**, *16* (27), 13838–13842.

(23) Suntivich, J.; Hong, W. T.; Lee, Y. L.; Rondinelli, J. M.; Yang, W.; Goodenough, J. B.; Dabrowski, B.; Freeland, J. W.; Shao-Horn, Y. Estimating Hybridization of Transition Metal and Oxygen States in Perovskites from o k -Edge X-Ray Absorption Spectroscopy. *J. Phys. Chem. C* **2014**, *118* (4), 1856–1863.

(24) Qiao, R.; Wray, L. A.; Kim, J. H.; Pieczonka, N. P. W.; Harris, S. J.; Yang, W. Direct Experimental Probe of the Ni(II)/Ni(III)/Ni(IV) Redox Evolution in LiNi0.5Mn1.5O4 Electrodes. *J. Phys. Chem. C* **2015**, *119* (49), 27228–27233.

(25) Huang, Y.; Dong, Y.; Li, S.; Lee, J.; Wang, C.; Zhu, Z.; Xue, W.; Li, Y.; Li, J. Lithium Manganese Spinel Cathodes for Lithium-Ion Batteries. *Adv. Energy Mater.* **2020**, 2000997.

(26) Tang, D.; Sun, Y.; Yang, Z.; Ben, L.; Gu, L.; Huang, X. Surface Structure Evolution of

LiMn2O4 Cathode Material upon Charge/Discharge. *Chem. Mater.* **2014**, *26* (11), 3535–3543.

(27) Hong, Y. S.; Huang, X.; Wei, C.; Wang, J.; Zhang, J. N.; Yan, H.; Chu, Y. S.; Pianetta, P.; Xiao, R.; Yu, X.; Liu, Y.; Li, H. Hierarchical Defect Engineering for LiCoO2 through Low-Solubility Trace Element Doping. *Chem* **2020**, *6* (10), 2759–2769.

(28) Saravanan, K.; Jarry, A.; Kostecki, R.; Chen, G. A Study of Roomerature LixMn1.5Ni0.5O4 Solid Solutions. *Sci. Rep.* **2015**, *5* (1), 8027.

Chapter 6. Conclusions and Perspectives

6.1. Conclusions

This dissertation concerns elucidating the properties of high-voltage, single-crystal, spinel oxide cathode material, $LiNi_{0.5}Mn_{1.5}O_4$ (LNMO), through lab-based and advanced synchrotron techniques. The parameters of the molten salt synthesis method and their effect on structural and electronic properties are explored in depth through a suite of characterization methods to reveal the significance and evolution of physical and chemical heterogeneities at multiple length scales. High-resolution nanodiffraction experiments were developed as diagnostic tools to examine structural defects and distortions in material. **Chapter 1** introduces the competing structures of LNMO material, which consist of cation ordered and cation disordered spinel phases. Mn^{3+} content is closely related to cation ordering and influences the electrochemical properties of the cathode in battery systems. The molten salt synthesis method is chosen as a highly tunable platform to control morphology and Mn^{3+} content of single-crystal LNMO for further studies.

Chapter 2 systemically explores the influence of tuning molten salt synthesis parameters including calcination time, transition metal to salt ratio, and the surface area of the sample slurry exposed to the atmosphere on particle size and shape uniformity at the materials level. We found that tuning the exposed surface area through changing crucible size, batch size, and covering condition has an influence on the resulting particle size distribution and performance, with limited oxygen flow increasing sample purity and specific capacity in half-cell batteries. This study also reveals the challenges in reproducibility for small-scale molten salt LNMO synthesis.

In **Chapter 3**, we employ high-spatial-resolution X-ray nanodiffraction to map lattice distortions and defects in octahedral and plate-like particles and reveal that strain is heterogeneously distributed in single crystals. A larger Mn^{3+} content present in the plate-like

sample synthesized at a higher temperature causing cation disordering contained a greater intensity of lattice distortions as well as a more heterogeneous spatial distribution. We further explore the changes in lattice distortion in the plate sample upon Li removal with chemical delithiation in **Chapter 4**. Severe particle fragmentation and increased lattice distortion heterogeneity were observed, which we attribute to both the cubic phase changes occurring in the material upon Li removal and structural and chemical degradation of the particle due to Mn dissolution. We conclude that our chemical delithiation method could not replicate the electrochemical cycling process as it caused severe structural damage and dissolution in individual particles. Finally, **Chapter 5** develops and analyzes *in situ* nanodiffraction measurements on octahedral LNMO particles, taken to better visualize the dynamic structural evolution occurring during Li removal under more practical battery operating conditions. We observe multiple nanodomains within the particle and non-linear changes in strain heterogeneity upon cycling suggesting nanodiffraction is a powerful method of characterizing defects and degradation mechanism in cathode materials.

In the following sections of **Chapter 6**, we provide perspectives for the future of LNMO synthesis, modification, applications, and characterization, based on insights gleaned from the work in and beyond this dissertation.

6.2. Perspectives for Future Works

6.2.1. Optimizing the Synthesis and Properties of Single-Crystal LNMO

The molten salt method is highly tunable allowing for precise tailoring of materials level and particle level properties. Taking advantage of this method, our results suggest that there is an optimal concentration of cation ordering and Mn^{3+} in as-synthesized LNMO to achieve high capacity and rate capability while repressing secondary impurity formation.[1,2] Furthermore,

microstructure control to precisely tailor facets can dictate the rate performance or phase stability of materials.[3–5] However, further fundamental studies are required to fully study and understand synergistic relationships of materials properties as well as particle growth mechanisms for finer morphological control and reproducibility. For example, further work in the molten salt synthesis method may explore growing the largest or smallest uniform particle sizes to correlate size to stability or performance. Turing the heating profile could potentially create a gradient of Mn oxidation states within particles for improved bulk performance with stable surfaces, which could be probed through electron energy loss spectroscopy (EELS) experiments.

A complete picture of the interplay between global and local cation ordering, oxygen vacancies, Mn oxidation state, impurity content, and structure has eluded research consensus and upholds spinel LNMO as a highly complex cathode material system. Additionally, in this work we have observed heterogeneity at multiple length scales further complicating efforts to define and correlate structure-property-performance relationships. Continued systematic research in tailoring and optimization of structure (i.e. transition metal ordering) and Mn oxidation state to minimize heterogeneity through advanced and well-controlled synthesis methods including molten salt, solid state, hydrothermal, etc. as well as characterization through multi-modal techniques are required to improve the performance and stability of LNMO cathode materials.

6.2.2. Modification Strategies to Mitigate Degradation

Mn dissolution and interfacial reactions at high voltages lead to capacity fading and are the major degradation mechanisms of spinel LNMO cathode materials. Surface coating with metals, carbon materials, oxides, phosphates, lithium compounds, or polymers can physically separate active material and organic electrolyte components to alleviate degradation from Mn dissolution.[6,7]

Doping with transition metals such as Fe, Ga, Zn, Al, Cr, Co, and Cu, or anions F, Cl, S, P, and Si can be done in bulk or at the active materials surface and can influence cation ordering, provide structural enhancements, and improve ionic and electronic conductivity to improve cycling performance.[7–9] Electrolyte additives such as fluoroethylene carbonate (FEC), lithium bis(oxalate)borate (LiBOB), and dimethyl methylphosphonate (DMMP) salts have been used to provide stability at high operating voltages.[10] Coupling experiment design with machine learning could be helpful to explore the full compositional space to develop new dopant combinations and high-voltage stable liquid electrolytes.[11] The development of solid polymer, ceramic, or polymer-ceramic composite electrolytes for all-solid-state batteries could further improve the mechanical stability and safety of cells operating at high voltages. **Figure 6-1** summarizes the challenges, synthesis methods, and modification strategies to mitigate degradation in LNMO. Ultimately, continued fundamental studies are needed to understand degradation mechanisms relating to Mn dissolution and surface instability in LNMO coupled with experimental testing and characterization to identify practical solutions that are green, cost effective, and safe for use in LiBs.

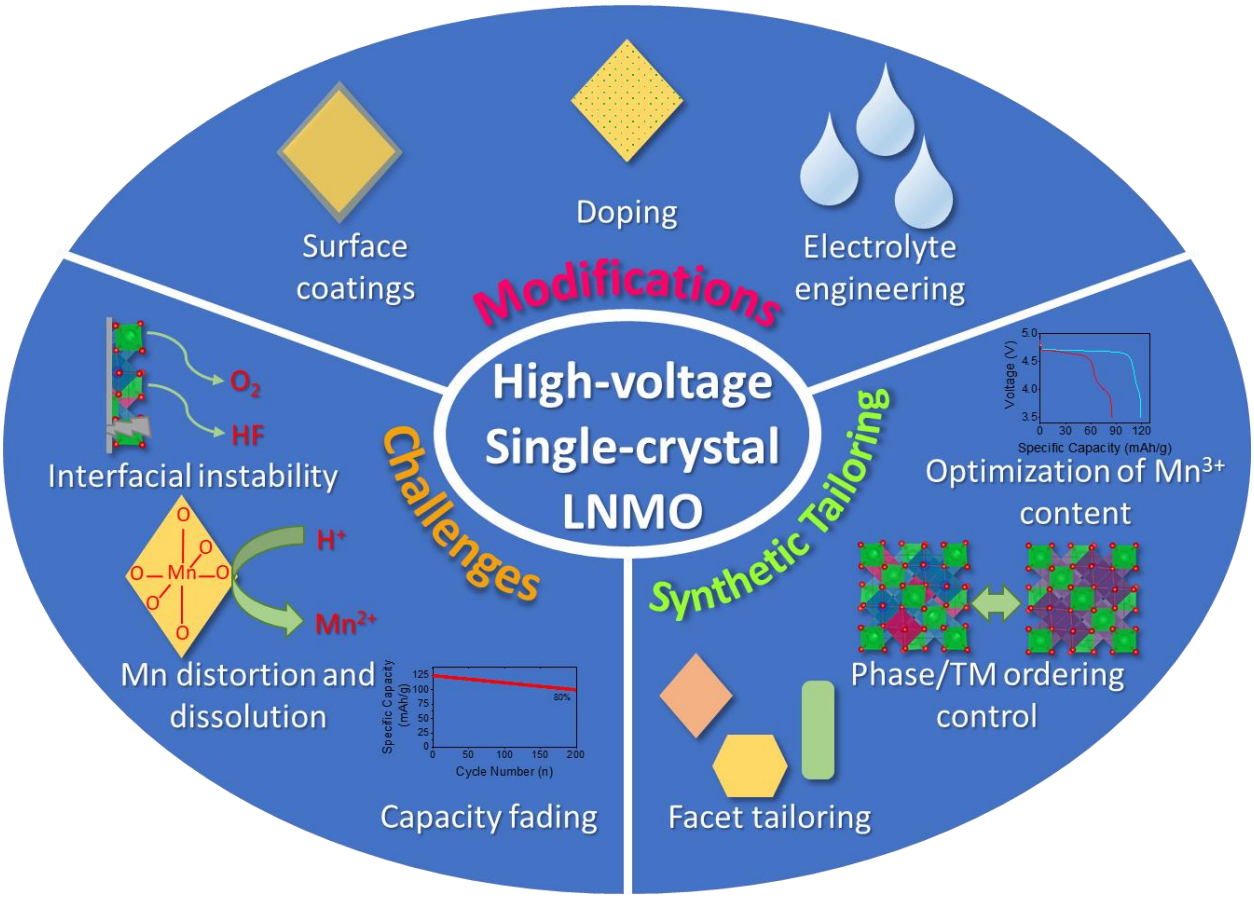

Figure 6-1. Schematic of major challenges, synthetic tailoring, and modification strategies for high-voltage, single-crystal LNMO materials.

6.2.3. Future Applications of High-Voltage LNMO

The ability of spinel transition metal oxides to intercalate and extract Li ions allows them to potentially be used as tunable supports for metal nanocatalysts.[12] Utilizing material typically used as battery cathodes for catalysis applications is an opportunity to potentially repurpose spent battery materials, which typically have lifetimes of only three to eight years in consumer products.[13] Through delithiation, the oxidation state of transition metals can be tuned, influencing TM-3d orbital occupancy and TM−O covalency and, ultimately, the catalytic activity of the material itself or a supported metal.[14] Li containing layered and spinel transition metal oxides are

active for the oxygen evolution reaction, an intensive 4-electron process, as a result of Li mobility.[12,15] The structural stability and tunable properties of spinel LNMO make it favorable for use as a support system for nanosized gold or platinum to understand and optimize support effects and to design novel heterogeneous catalysts.

While the practical capacity of LNMO may not presently be able to reach that of layered cathode materials, it is a favorable cathode to enable fast charging capabilities. Layered LCO, NMC, NCA, or Li-rich cathodes undergo surface phase reconstructions to undesirable spinel-like phases blocking Li diffusion channels and leading to capacity fading and impedance buildup.[16,17] LNMO spinel, on the other hand, is characterized by three-dimensional Li diffusion channels which allow for fast Li-ion transport and can improve rate performances.[8,11,18] Furthermore, the structural stability of this so-called "good spinel" material prevents disadvantageous surface reconstruction.[11] LNMO spinel structures can therefore be integrated as surface coatings or as duel structure cathodes to provide robust structural frameworks, reduce costs, and improve rate performance in high-performing layered cathode materials.[11,19] Integration of LNMO into solid-state batteries could also potentially bypass the challenge of Mn dissolution they face in liquid electrolytes and allow for high-voltage stable cycling.[11,20]

6.2.4. Challenges and Future Directions for X-ray Nanodiffraction Experiments

The use of synchrotron X-ray nanodiffraction is relatively new method for the study of battery materials. Our utilization of this method for properties investigations of high-voltage cathode materials and the development of chemical delithiation and *in situ* cycling studies have illustrated both the challenges and exciting possibilities of this technique. With a spatial resolution of 50 nm, our experiments require micron sized particles to accurately measure heterogeneity. In

Chapter 3, we measure particles with octahedral and plate morphologies. We first identify isolated single crystals of appropriate size via SEM before nanodiffraction; however, the particles were revealed to be not be perfect single crystals but contained severe defects and nano-sized grains which complicated analysis. We used the plate-like particle in **Chapter 4** to perform experiments after chemical delithiation as the flat surface allowed us to affix the particle to the sample mounting board, reducing the risk of the particle being washed away during the chemical soaking. Ideally, we would like to perform chemical delithiation on both the octahedral and plate particle, but risk the movement of particles with more complex morphologies. In the *in situ* studies in **Chapter 5**, a thin electrode with low materials loading was used to increase the chances of finding a single, isolated particle, however particle agglomeration still presented challenges to finding a candidate particle. Furthermore, we are not able to identify a particle by SEM in the *in situ* cell before nanodiffraction measurements and must identify a particle under the X-ray based on the diffraction signal. As previously discussed, the geometry of the *in situ* cell design also led to challenges in particle alignment during the cycling. It is also not possible to measure the current density of the individual particle or particles measured so the true SOC may not be accurate. We observed changing orientation of the particles during each of the measurements limiting our comparisons of particles after chemical delithiation/cycling. Measuring multiple particles would allow for more representative information, but the length of time of each measurement (~8 hours for a 5 µm x 5µm map) limits our experimental capabilities. In future studies we hope to couple *in situ* nanodiffraction and *in situ* XANES on LNMO during cycling to spatially and temporally correlate lattice distortion and Mn oxidation state; however, the sample would have to be moved back and forth between beamlines and the overhead time for sample setup and beam/sample alignment would take away significantly from measurement time. **Figure 6-2** summarizes some of the

experimental challenges faced throughout this work, strategies for improvements, and future experiment designs and capabilities. Overall, while highly complex and requiring careful experimental planning and design, nanodiffraction is an emerging experimental platform for the structural analysis of battery cathode materials including LNMO.

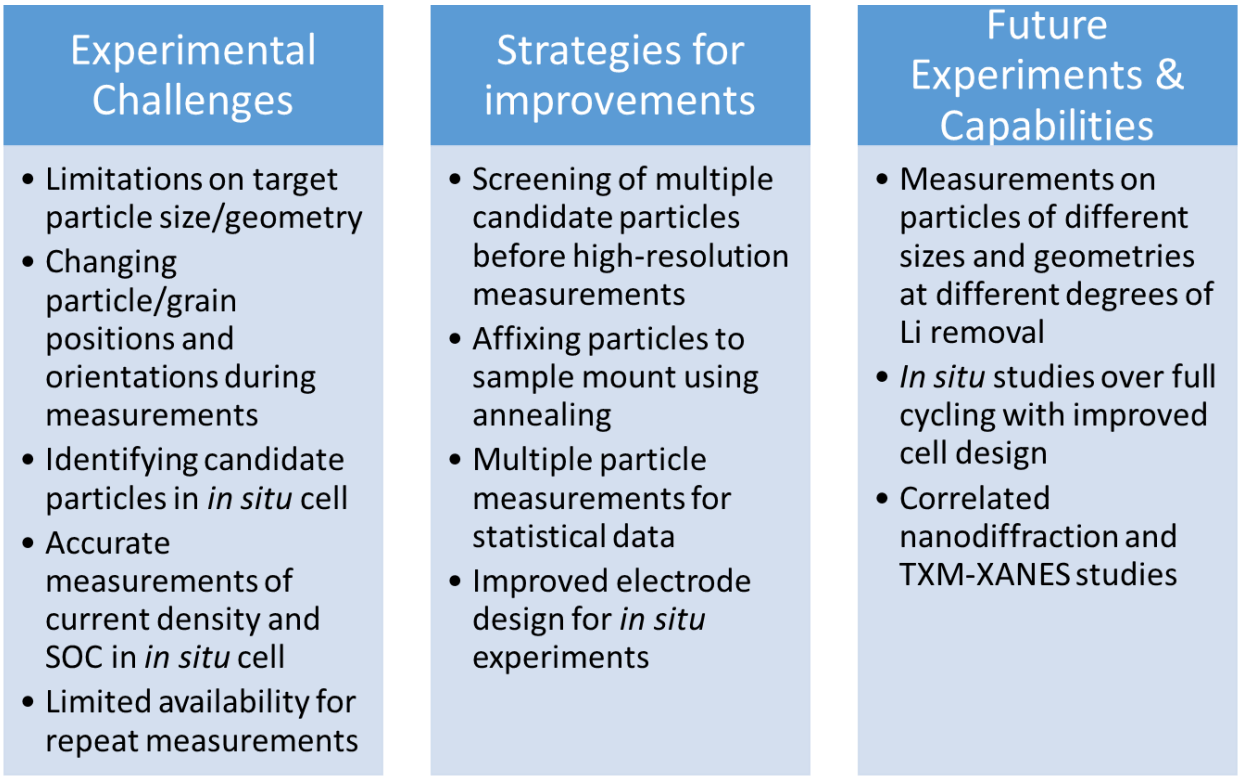

Figure 6-2. Summary of challenges encountered during nanodiffraction experiments, strategies for improvement, and future experimental designs and capabilities.

6.2.5. Advanced Characterization Techniques

Herein, we have discussed limitations to bulk averaged characterization techniques such as powder XRD or XAS that cannot detect intra-particle phase and chemical heterogeneities. High-resolution techniques that can provide information at the nano-scale such as nanodiffraction and

transmission X-ray microscopy require high-energy synchrotron X-ray sources, which have limited availability and often require specialized training to operate or perform data analysis. These methods are also not representative as only a few or single particles can be measured at a time, with each measurement potentially taking several hours to perform. Temporal resolution is limited when dynamic information is needed at practical timescales for battery operation. Techniques measuring tomography are restricted by sample size or geometry. Multimodal imaging and/or spectroscopic techniques at multiple length scales are therefore highly desired for the full characterization of battery materials. Techniques with improved experimental throughput or over a large sample size for statistical analysis but maintaining high spatial resolution would be ideal to further the understanding of battery materials systems. Measuring only a few samples may not be fully representative as the particle-to-particle variation may be severe or not all particles may be electrochemically active in the cell. As it stands, we must rely on coupling techniques with different length and/or time scales and resolutions to visualize the full structural and chemical picture of a sample. As technologies and data analysis methods advance improving resolution in high-throughput techniques or improving throughput in high-resolution techniques exciting new capabilities will progress our understanding of battery materials.

In conclusion, LNMO is a highly tunable platform and synthesis methods, such as molten salt, can be used to design materials with properties for specific applications including higher capacity, energy density, high rate performance, or long cycle life. Continued research efforts to identify structural and chemical heterogeneities, distortions, and their influence on performance are vital to elucidate further fundamental materials properties and to mitigate degradation. Accessible, high-resolution characterization techniques are required for the measurement of properties with high sample throughput. While single-crystal LNMO is a green alternative to Co-

containing cathodes, continued optimization and the development of high-voltage compatible battery components and materials are required before achieving commercialization.

6.3. References

(1) Spence, S. L.; Xu, Z.; Sainio, S.; Nordlund, D.; Lin, F. Tuning the Morphology and Electronic Properties of Single-Crystal LiNi 0.5 Mn 1.5 O 4−δ : Exploring the Influence of LiCl–KCl Molten Salt Flux Composition and Synthesis Temperature. *Inorg. Chem.* **2020**, *59*, 10591–10603.

(2) Sun, H.; Hu, A.; Spence, S.; Kuai, C.; Hou, D.; Mu, L.; Liu, J.; Li, L.; Sun, C.; Sainio, S.; Nordlund, D.; Luo, W.; Huang, Y.; Lin, F. Tailoring Disordered/Ordered Phases to Revisit the Degradation Mechanism of High-Voltage LiNi0.5Mn1.5O4 Spinel Cathode Materials. *Adv. Funct. Mater.* **2022**, 2112279.

(3) Cabana, J.; Zheng, H.; Shukla, A. K.; Kim, C.; Battaglia, V. S.; Kunduraci, M. Comparison of the Performance of LiNi1/2Mn3/2O4 with Different Microstructures. *J. Electrochem. Soc.* **2011**, *158* (9), A997.

(4) Xue, Y.; Wang, Z.; Zheng, L.; Yu, F.; Liu, B.; Zhang, Y.; Ke, K. Investigation on Preparation and Performance of Spinel LiNi0.5 Mn1.5 O4 with Different Microstructures for Lithium-Ion Batteries. *Sci. Rep.* **2015**, *5* (1), 13299.

(5) Yang, J.; Han, X.; Zhang, X.; Cheng, F.; Chen, J. Spinel LiNi0.5Mn1.5O4cathode for Rechargeable Lithiumion Batteries: Nano vs Micro, Ordered Phase (P4332) vs Disordered Phase (Fd3̄m). *Nano Res.* **2013**, *6* (9), 679–687.

(6) Yi, T. F.; Mei, J.; Zhu, Y. R. Key Strategies for Enhancing the Cycling Stability and Rate Capacity of LiNi0.5Mn1.5O4 as High-Voltage Cathode Materials for High Power Lithium-Ion Batteries. *J. Power Sources* **2016**, *316*, 85–105.

(7) Yu, X.; Yu, W. A.; Manthiram, A. Advances and Prospects of High-Voltage Spinel Cathodes for Lithium-Based Batteries. *Small Methods* **2021**, *5* (5), 1–30.

(8) Chemelewski, K. R.; Li, W.; Gutierrez, A.; Manthiram, A. High-Voltage Spinel Cathodes for Lithium-Ion Batteries: Controlling the Growth of Preferred Crystallographic Planes through Cation Doping. *J. Mater. Chem. A* **2013**, *1* (48), 15334–15341.

(9) Wang, Y.; Wang, E.; Zhang, X.; Yu, H. High-Voltage "Single-Crystal" Cathode Materials for Lithium-Ion Batteries. *Energy and Fuels* **2021**, *35* (3), 1918–1932.

(10) Manthiram, A.; Chemelewski, K.; Lee, E. S. A Perspective on the High-Voltage LiMn1.5Ni0.5O 4 Spinel Cathode for Lithium-Ion Batteries. *Energy Environ. Sci.* **2014**, *7* (4), 1339–1350.

(11) Huang, Y.; Dong, Y.; Li, S.; Lee, J.; Wang, C.; Zhu, Z.; Xue, W.; Li, Y.; Li, J. Lithium Manganese Spinel Cathodes for Lithium-Ion Batteries. *Adv. Energy Mater.* **2020**, 2000997.

(12) Lu, Z.; Wang, H.; Kong, D.; Yan, K.; Hsu, P.-C.; Zheng, G.; Yao, H.; Liang, Z.; Sun, X.; Cui, Y. Electrochemical Tuning of Layered Lithium Transition Metal Oxides for Improvement of Oxygen Evolution Reaction. *Nat. Commun.* **2014**, *5* (1), 4345.

(13) Zheng, X.; Zhu, Z.; Lin, X.; Zhang, Y.; He, Y.; Cao, H.; Sun, Z. A Mini-Review on Metal Recycling from Spent Lithium Ion Batteries. *Engineering* **2018**, *4* (3), 361–370.

(14) Okubo, M.; Yamada, A. Molecular Orbital Principles of Oxygen-Redox Battery Electrodes. *ACS Appl. Mater. Interfaces* **2017**, *9* (42), 36463–36472.

(15) Robinson, D. M.; Go, Y. B.; Greenblatt, M.; Dismukes, G. C. Water Oxidation by λ-MnO2: Catalysis by the Cubical Mn4O4Subcluster Obtained by Delithiation of Spinel LiMn2O4. *J. Am. Chem. Soc.* **2010**, *132* (33), 11467–11469.

(16) Lin, F.; Markus, I. M.; Nordlund, D.; Weng, T. C.; Asta, M. D.; Xin, H. L.; Doeff, M. M. Surface Reconstruction and Chemical Evolution of Stoichiometric Layered Cathode Materials for Lithium-Ion Batteries. *Nat. Commun.* **2014**, *5*, 3529.

(17) Xiao, P.; Shi, T.; Huang, W.; Ceder, G. Understanding Surface Densified Phases in Ni-Rich Layered Compounds. *ACS Energy Lett.* **2019**, *4* (4), 811–818.

(18) Zheng, J.; Xiao, J.; Yu, X.; Kovarik, L.; Gu, M.; Omenya, F.; Chen, X.; Yang, X. Q.; Liu, J.; Graff, G. L.; Whittingham, M. S.; Zhang, J. G. Enhanced Li + Ion Transport in LiNi 0.5Mn 1.5O 4 through Control of Site Disorder. *Phys. Chem. Chem. Phys.* **2012**, *14* (39), 13515–13521.

(19) Zhu, Z.; Yu, D.; Shi, Z.; Gao, R.; Xiao, X.; Waluyo, I.; Ge, M.; Dong, Y.; Xue, W.; Xu, G.; Lee, W. K.; Hunt, A.; Li, J. Gradient-Morph LiCoO2 Single Crystals with Stabilized Energy Density above 3400 W h L−1. *Energy Environ. Sci.* **2020**, *13* (6), 1865–1878.

(20) Zhao, J.; Zhang, J.; Hu, P.; Ma, J.; Wang, X.; Yue, L.; Xu, G.; Qin, B.; Liu, Z.; Zhou, X.; Cui, G. A Sustainable and Rigid-Flexible Coupling Cellulose-Supported Poly(Propylene Carbonate) Polymer Electrolyte towards 5 V High Voltage Lithium Batteries. *Electrochim. Acta* **2016**, *188*, 23–30.